

REPORT DOCUMENTATION PAGE			<i>Form Approved</i> OMB No. 0704-0188	
Public reporting burden for this collection of information is estimated to average 1 hour per response, including the time for reviewing instructions, searching existing data sources, gathering and maintaining the data needed, and completing and reviewing this collection of information. Send comments regarding this burden estimate or any other aspect of this collection of information, including suggestions for reducing this burden to Department of Defense, Washington Headquarters Services, Directorate for Information Operations and Reports (0704-0188), 1215 Jefferson Davis Highway, Suite 1204, Arlington, VA 22202-4302. Respondents should be aware that notwithstanding any other provision of law, no person shall be subject to any penalty for failing to comply with a collection of information if it does not display a currently valid OMB control number. PLEASE DO NOT RETURN YOUR FORM TO THE ABOVE ADDRESS.				
1. REPORT DATE (DD-MM-YYYY) 22-02-2010		2. REPORT TYPE Final		3. DATES COVERED (From - To) March, 2007 - November, 2009
4. TITLE AND SUBTITLE Hybrid LES/RANS Simulation of the Effects of Boundary Layer Control Devices Using Immersed Boundary Methods			5a. CONTRACT NUMBER	
			5b. GRANT NUMBER FA9550-07-1-0191	
			5c. PROGRAM ELEMENT NUMBER	
6. AUTHOR(S) Jack R. Edwards			5d. PROJECT NUMBER	
			5e. TASK NUMBER	
			5f. WORK UNIT NUMBER	
7. PERFORMING ORGANIZATION NAME(S) AND ADDRESS(ES) North Carolina State University, 8 Holliday Hall, Campus Box 7214, Raleigh, North Carolina 27525-7214			8. PERFORMING ORGANIZATION REPORT NUMBER	
9. SPONSORING / MONITORING AGENCY NAME(S) AND ADDRESS(ES) Air Force Office of Scientific Research Aerospace, Chemical, and Materials Sciences Directorate 875 N. Randolph St. Arlington, VA, 22203			10. SPONSOR/MONITOR'S ACRONYM(S) AFOSR/NA	
			11. SPONSOR/MONITOR'S REPORT NUMBER(S)	
12. DISTRIBUTION / AVAILABILITY STATEMENT Approved for public release; distribution unlimited.				
13. SUPPLEMENTARY NOTES				
14. ABSTRACT This work has developed an extension of an existing immersed-boundary (IB) method to compressible, turbulent flows and has investigated its use in simulating the effects of different types of flow control devices: micro vortex generators, bleed-hole arrays, aero-elastically-deforming 'mesoflaps', and boundary layer trips. The IB method has been used with Reynolds-averaged Navier-Stokes (Menter SST) and hybrid large-eddy simulation / Reynolds-averaged Navier-Stokes (LES/RANS) turbulence closures. The method has been applied to oblique shock / turbulent boundary layer interactions with and without micro vortex-generator flow control (Cambridge University experiments), bleed flow control (NASA Glenn experiments), and aeroelastically-deforming mesoflap flow control (University of Illinois experiments). The results show that the IB approach can simulate the general effects of the control devices to a high degree of precision without requiring excessively fine meshes near the control element. The LES/RANS method is capable of accurately predicting mean-flow and second-moment statistics and can be used to provide insights into the effects of the control device in modulating the turbulent flow response.				
15. SUBJECT TERMS hybrid large-eddy / Reynolds-averaged Navier-Stokes simulations, shock wave / turbulent boundary layer interaction, micro vortex generators, boundary-layer bleed				
16. SECURITY CLASSIFICATION OF:			17. LIMITATION OF ABSTRACT UL	18. NUMBER OF PAGES 75
a. REPORT unclassified	b. ABSTRACT unclassified	c. THIS PAGE unclassified		
			19b. TELEPHONE NUMBER (include area code) (919) 515-5264	

Hybrid LES/ RANS Simulation of the Effects of Boundary Layer Control Devices Using Immersed Boundary Methods

Final Technical Report

**Air Force Office of Scientific Research
FA9550-07-1-0191**

Submitted by

**Dr. Jack R. Edwards
Department of Mechanical and Aerospace Engineering
Campus Box 7910
North Carolina State University
Raleigh, NC 27695**

To

**Air Force Office of Scientific Research
Aerospace, Chemical, and Materials Sciences Directorate (NA)
(Attn. Dr. John Schmisser, program manager, Hypersonics and Turbulence)
875 N. Randolph St.
Arlington, VA 22203**

TABLE OF CONTENTS

<u>Section</u>	<u>Page Numbers</u>
Table of Contents	2
Project Abstract (Original Proposal)	4
1. Background and Objectives	5
2. Numerical Methods	7
3. Turbulence Models	8
3.1. Menter's SST Model	8
3.2. Hybrid LES/RANS Model	9
3.3. Recycling / Rescaling Method	11
4. Immersed Boundary Method	12
4.1. Cell Classification Procedure	13
4.2. Band-Cell Interpolations	14
4.3. Determination of Information at the Interpolation Point	16
5. Fluid / Structure Interactions	18
5.1. Structural Solver: Beam Bending Equations	18
5.2. Fluid-Structure Coupling	20
5.2.1. Determination of loads on flap surfaces from neighboring fluid cells	20
5.2.2. Interpolation of loads	21
5.2.3. Fluid-structure iteration	21
5.2.4. Fluid solver changes	22
6. Results	23
6.1. Overview	23
6.2. Micro VG Control of Shock / Boundary Layer Interactions	23
6.2.1. Experiment details	24
6.2.2. Computational domain and calculation details	25
6.2.3. Inflow boundary layer	27
6.2.4. Immersed-boundary assessment: Mach 2.5 flow over a single micro VG	27
6.2.5. Detailed data comparisons for Mach 2.5 flow over 6 mm and 3 mm micro VGs	30
6.2.6. Wind-tunnel shock / boundary layer interaction – flow structure	32
6.2.7. Wind-tunnel shock / boundary layer interaction	

– comparisons with experimental data	32
6.2.8. Wind-tunnel shock / boundary layer interaction with micro VG flow control –flow structure	33
6.2.9. Wind-tunnel shock / boundary layer interaction with micro VG flow control –comparisons with experimental data	35
6.2.10. Idealized shock / boundary layer interactions	36
6.2.11. Idealized shock / boundary layer interaction with micro VG flow control	38
6.3. Bleed Control of Shock / Boundary Layer Interactions	41
6.3.1. Experiment details	41
6.3.2. Computational domain and calculation details	41
6.3.3. Flat-plate boundary layer simulations with bleed	44
6.3.4. Oblique shock / turbulent boundary layer interaction without bleed	44
6.3.5. Oblique shock / turbulent boundary layer interaction with bleed	46
6.3.6. Reynolds stress evolution and turbulence structure	52
6.4. Mesoflap Control of Shock / Boundary Layer Interactions	54
6.4.1. Experiment details	54
6.4.2. Computational domain and calculation details	55
6.4.3. Oblique shock / boundary layer interaction without mesoflap array	57
6.4.4. Flow structure of oblique shock / boundary layer interaction with mesoflap array -2-D FSI modeling	60
6.4.5. Flow structure of oblique shock / boundary layer interaction with mesoflap array – 3-D FSI modeling	62
6.4.6. Oblique shock / boundary layer interaction with mesoflap array – data comparisons	66
6.5. Hyper-X Boundary Layer Trip Arrays	68
6.6. University of Michigan 3D Shock / Boundary Layer Interaction	68
7. Conclusions	69
8. Directions for Future Work	71
9. Publications Resulting from this Study	71
10. Personnel	72
11. Connections / Collaborations / Invited Talks	72
12. Bibliography	73

Project Abstract (Original Proposal)

The focus of this research program is to combine a recently developed capability for hybrid large-eddy / Reynolds-averaged Navier-Stokes (LES/RANS) simulations with a novel immersed-boundary method to predict the effects of different techniques for forcing boundary-layer transition and mitigating flow separation due to shock / boundary layer interactions. Hybrid LES/RANS methods can naturally account for time-dependent phenomena, such as unsteady shock motion, and have displayed an ability to predict the rapid recovery of a turbulent boundary layer following separation and re-attachment. Because the near-wall boundary-layer structure is modeled through RANS concepts, no restrictions in Reynolds number are required. The use of immersed-boundary techniques promises significant economy in the number of mesh points required to simulate complex objects such as boundary-layer trip arrays and perforated-plate bleed systems. Furthermore, they can be coupled with structural response models in a straightforward manner, thus enabling simulation of passive control methods based on aero-elastic flap deflections. The proposed research program is focused in three areas: (1.) development of immersed-boundary techniques for compressible, turbulent flows at high Reynolds number; (2.) development of strategies for coupling structural response models with immersed-boundary movement; (3.) simulation of well-documented experiments involving boundary-layer trip effects, active bleed control of shock / boundary layer interactions, and passive control of shock / boundary interactions using ‘meso flap’ arrays; and (4.) use of data from hybrid LES/RANS simulations to guide development of engineering-level models for the effects of boundary-layer control devices.

1. Background and Objectives

The control of shock-induced separation within a supersonic inlet is critical in achieving the desired total pressure recovery and uniformity of the flow entering the compressor. Off-design responses, such as inlet unstart, are often the result of the growth of large regions of separated flow, generated initially through shock interactions. Control of shock-induced separation within the inlet often involves the use of passive or active bleed systems and slots to skim off the boundary layer [1-5]. Control techniques based on aero-elastic deformation of thin flaps (UIUC's 'mesoflap' concept and others) have been proposed [6-8]. Micro vortex generators (micro VGs) are currently being considered as a means of energizing a boundary layer through the introduction of axial vorticity. [9,10] The proper implementation of such control systems requires an understanding of their effects at on and off-design conditions. Computational fluid dynamics can potentially play an important role in the design and implementation of boundary-layer control techniques, but the direct rendering of large numbers of such control devices within the framework of a complete engine simulation is currently infeasible. Such effects must be modeled at some level, and in the absence of detailed experimental data, there is little available to guide the modeling.

The design of active or passive bleed systems for high-speed inlets is an area in which experimentation and empirical correlations have played a dominant role.[3,4] Most efforts in simulation of boundary layer bleed for separation control have concentrated on single slot or hole effects [11-14]. With the exception of a few three-dimensional studies involving resolution of individual holes using overset-grid techniques [13,14], most studies have assumed two-dimensional flow, and all have utilized Reynolds-averaged Navier-Stokes (RANS) models or simpler strategies. Given that fact that shock / boundary layer interactions tend to be unsteady on a large scale, and that local pressure differences can lead to periodic blowing / suction even in "active" control devices [5], it appears that accounting for the time-dependent nature of the control approach and its interaction with the flow may be critical to achieving better predictions. The geometric complexity of bleed systems complicates the application of techniques such as large-eddy simulation (LES), as resolution of features such as individual holes would normally require a large number of clustered mesh cells. The number of mesh points used could become excessively large, and the accuracy of the LES approach could diminish due to the presence of irregular mesh cells.

Passive control of shock / boundary layer interactions (SBLIs) through the use of vortex generators embedded within the boundary layer [9,10] is being considered as an alternative to traditional bleed systems. In these concepts, micro vortex generators are embedded in regular arrays within the boundary layer upstream of a shock-impingement point. The devices modify the structure of the turbulent boundary layer, energizing to the point that it can better resist the shock-induced adverse pressure gradient. The effects of flow-aligned, regular arrays of such devices may be simulated by gridding a few objects in detail and by imposing periodic boundary conditions. However, this approach neglects the effects of possible three-dimensionality, which may result from sidewall shock / boundary layer interactions. The accurate prediction of the performance of micro VGs may also require a time-dependent method of analysis, due to the need to capture the dynamics of the generated vortical structures and their effects on the shock / boundary layer interaction.

The purpose of this study is to develop a different framework for conducting detailed time-dependent simulations of the effects of control devices, such as bleed through perforated plates, aerolastically-deformable ‘mesoflaps’, and micro vortex generators, on shock wave / boundary layer interactions. The approach will combine hybrid large-eddy / Reynolds-averaged (LES/RANS) techniques for flowfield modeling [15,16] with a novel immersed-boundary (IB) concept [17] for geometric rendering of control devices. The use of LES/RANS techniques in this scope implies that the effect of the control techniques on the development of larger turbulent eddies should be captured directly for improved accuracy. The LES/RANS concepts developed at NCSU involve the use of flow-dependent blending functions to shift the closure from a RANS description near solid surfaces to a LES description in the outer portion of the boundary layer. Coherent structure growth is sustained through the application of recycling / re-scaling strategies [15]. As the near-wall behavior is modeled using RANS, the total number of mesh points needed is significantly less than for a wall-resolved LES at the same Reynolds number.

The use of immersed-boundary (IB) techniques [18-20] in this scope promises significant economy in terms of the overall number of grid points required, as fine details of the flow near (or within) control devices are modeled, rather than directly simulated. The hope is that the geometric influences of the control technique on the surrounding flow are captured properly. Our prior work [17] for incompressible flows has shown that this can be the case in general, even at high Reynolds number. Another advantage of an IB method, as opposed to direct rendering, is that feature deformation under time-dependent aero-elastic loads can be captured simply and directly without recourse to grid re-generation or adaptation. A further advantage is that changes in the design or placement or number of control devices can be accomplished in a trivial manner, by simply re-generating the underlying CAD surface descriptions of the objects. The IB procedures are not dependent on whether the turbulence closure is RANS or hybrid LES/RANS and can be incorporated into production level RANS codes as a means of directly simulating the large-scale effects of particular control methods.

The remainder of this report outlines the numerical methods used in Section 2 and the turbulence closure methods employed in Section 3. A complete description of an IB method valid for compressible, turbulent flows is provided in Section 4, and the extension of the methodology to aero-elastic deformation of surfaces as described by beam-bending theory is discussed in Section 5. The results of the investigation are presented in Section 6. Three major classes of control devices for shock / boundary layer interactions are considered: micro VGs (Section 6.2), bleed arrays (Section 6.3), and mesoflaps (Section 6.4). In addition, results from other studies that employ the developed IB method to simulate laminar flows over boundary layer trip devices (Section 6.5) and shock-generator effects in a 3-D shock / boundary layer interaction (Section 6.6) are described in brief. Conclusions of the study are presented in Section 7, and directions for future work are discussed in Section 8.

2. Numerical Methods

Simulations were performed using NCSU’s REACTMB code. In REACTMB, the governing equations are discretized in a finite-volume manner. Inviscid fluxes are discretized using Edwards’ LDFSS scheme [21], while viscous and diffusive fluxes are discretized using second-order central differences. The LDFSS scheme is extended to second or higher-order spatial accuracy using the piecewise parabolic method (PPM) [22], as described later. A dual-time stepping implicit method is used to advance the equations in time. At each time step, a

Crank-Nicholson discretization of the equations is solved to a prescribed tolerance using a sub-iteration procedure. The matrix system resulting from the linearization of the equation system is approximately solved using a planar relaxation procedure at each sub-iteration. To enhance computational efficiency, matrix elements are held fixed over the duration of the sub-iterations.

The PPM reduces to a fourth-order central differencing scheme for sufficiently smooth data, enhancing its ability to capture small-scale features. A cell-by-cell limiting procedure reduces the order of accuracy in the vicinity of local extrema in the solution. A general interface flux formula may be written as $\vec{F}_{i+1/2}(\vec{V}_{L,i+1/2}, \vec{V}_{R,i+1/2})$, with left-and-right state interpolations $\vec{V}_{L,i+1/2}$ and $\vec{V}_{R,i+1/2}$ determined by the step-by-step procedure described below.

Step 1: initially set left-and-right state values to fourth-order averaging operators. If unmodified, these provide a fourth-order central difference approximation to the flux difference $\vec{F}_{i+1/2} - \vec{F}_{i-1/2}$:

$$\vec{V}_{L,i+1/2} = \vec{V}_{R,i+1/2} = \frac{7}{2}(\vec{V}_i + \vec{V}_{i+1}) - \frac{1}{12}(\vec{V}_{i+2} + \vec{V}_{i-1}) \quad (1)$$

Step 2: conduct cell-by-cell limiting to enforce monotonicity:

$$\begin{aligned} &\text{if } \text{sgn}[(\vec{V}_{L,i+1/2} - \vec{V}_i)(\vec{V}_i - \vec{V}_{R,i-1/2})] = -1, \text{ then} \\ &\quad \vec{V}_{L,i+1/2} = \vec{V}_{R,i-1/2} = \vec{V}_i \\ &\text{else} \\ &\quad C = \vec{V}_{L,i+1/2} - \vec{V}_{R,i-1/2} \\ &\quad D = 6.0[\vec{V}_i - \frac{1}{2}(\vec{V}_{L,i+1/2} + \vec{V}_{R,i-1/2})] \\ &\quad \text{if } (DC > CC) \text{ then} \\ &\quad \quad \vec{V}_{R,i-1/2} = 3\vec{V}_i - 2\vec{V}_{L,i+1/2} \\ &\quad \text{elseif } (-CC > DC) \text{ then} \\ &\quad \quad \vec{V}_{L,i+1/2} = 3\vec{V}_i - 2\vec{V}_{R,i-1/2} \\ &\quad \text{end if} \\ &\text{end if} \end{aligned} \quad (2)$$

The first ‘if’ block resets the interpolation function to a constant if \vec{V}_i is a local maximum or minimum. The second ‘if’ block resets either the left-state value at interface $i + 1/2$ or the right-state value at interface $i - 1/2$ so that the interpolation parabola that connects the interface states with the state at the cell center is monotonically increasing or decreasing. It is also possible to enforce physical constraints (such as positive temperatures, densities, and mass fractions) at the cell interfaces by a similar cell-by-cell resetting algorithm. The PPM requires a seven point stencil in each coordinate direction, and the reconstruction procedures are applied to the primitive-variable vector $\vec{V} = [p, u, v, w, T, k, \omega]^T$.

3. Turbulence Closure

3.1. Menter's SST Model

The RANS turbulence model used in this investigation is Menter's hybrid $k - \omega / k - \varepsilon$ shear-stress transport (SST) model.[23] The transport equations for the turbulence kinetic energy, k , and the specific dissipation rate, ω for Menter's model are given by

$$\frac{\partial(\rho k)}{\partial t} + \frac{\partial(\rho k u_j)}{\partial x_j} = \mu_t S^2 - \beta^* \rho \omega k + \frac{\partial}{\partial x_j} \left[(\mu + \sigma_k \mu_t) \frac{\partial k}{\partial x_j} \right] \quad (3)$$

$$\frac{\partial(\rho \omega)}{\partial t} + \frac{\partial(\rho \omega u_j)}{\partial x_j} = \gamma \rho S^2 - \beta \rho \omega^2 + \frac{\partial}{\partial x_j} \left[(\mu + \sigma_\omega \mu_t) \frac{\partial \omega}{\partial x_j} \right] + 2(1 - F_1) \rho \sigma_\omega \frac{1}{\omega} \frac{\partial k}{\partial x_j} \frac{\partial \omega}{\partial x_j} \quad (4)$$

where S is taken to be the magnitude of the vorticity vector and ϕ represents any constant in Menter's model ($\sigma_k, \sigma_\omega, \dots$), averaged according to the blending function F_1

$$\phi = F_1 \phi_1 + (1 - F_1) \phi_2 \quad (5)$$

The ϕ_1 constants are from the $k - \omega$ model:

$$\begin{aligned} \sigma_{k1} &= 0.85, \quad \sigma_{\omega1} = 0.5, \quad \beta_1 = 0.075 \\ \beta^* &= 0.09, \quad \kappa = 0.41, \quad \gamma_1 = \frac{\beta_1}{\beta^*} - \frac{\sigma_{\omega1} \kappa^2}{\sqrt{\beta^*}} \end{aligned} \quad (6)$$

and the ϕ_2 constants are from the standard $k - \varepsilon$ model:

$$\begin{aligned} \sigma_{k2} &= 1.0, \quad \sigma_{\omega2} = 0.856, \quad \beta_2 = 0.0828 \\ \beta^* &= 0.09, \quad \kappa = 0.41, \quad \gamma_2 = \frac{\beta_2}{\beta^*} - \frac{\sigma_{\omega2} \kappa^2}{\sqrt{\beta^*}} \end{aligned} \quad (7)$$

The blending function F_1 is defined as

$$F_1 = \tanh(\arg_1^4), \quad \arg_1 = \max\left(\frac{\sqrt{k}}{0.09 \omega d}, \frac{500 \nu}{d^2 \omega}\right) \quad (8)$$

where d is the distance to the nearest wall. The eddy viscosity is defined as:

$$\nu_t = \frac{a_1 k}{\max(a_1 \omega, A_{sst} \Omega F_2)} \quad (9)$$

where $a_1 = 0.31$, Ω is the magnitude of the vorticity vector, and F_2 is another blending function given by

$$F_2 = \tanh(\arg_2^2), \quad \arg_2 = \max\left(2 \frac{\sqrt{k}}{0.09 \omega d}, \frac{500 \nu}{d^2 \omega}\right) \quad (10)$$

This 'shear stress transport' (SST) modification alters the turbulence frequency as used in the eddy viscosity definition in the vicinity of high strain rates. The general effect is to lower the eddy viscosity and thus to promote the growth of regions of separated flow. For the relatively weak interactions considered in this study, the use of the SST modification typically results in better RANS predictions. The Menter BSL model is used as the RANS component of the hybrid

LES/RANS model, as previous studies [15] have found that this approach provides generally better results than the use of the SST model.

3.2. Hybrid LES/RANS Model

The LES/RANS model used in this work is designed to transition from RANS near solid surfaces to LES as the boundary layer shifts from its logarithmic form to its wake-like form. The eddy viscosity as used in the turbulence transport equations and the main flow equations is defined as a weighted sum of a RANS description and a mixed-scale model [24]:

$$\mu_t = \rho \nu_t = \rho \left(\Gamma \frac{k}{\omega} + (1 - \Gamma) \nu_{t,SGS} \right), \quad (11)$$

with

$$\nu_{t,SGS} = C_M S^{1/2} (q^2)^{1/4} \Delta^{3/2}, \quad C_M = 0.06 \quad (12)$$

An estimate of the subgrid kinetic energy is obtained by test-filtering the resolved-scale velocity data:

$$q^2 = \frac{1}{2} (\tilde{u}_k - \hat{\tilde{u}}_k)^2 \quad (13)$$

The blending function Γ is designed to shift the closure from a RANS description near solid surfaces to an LES description in the outer parts of the boundary layer and in regions of flow separation. The blending function is based on the ratio of the wall distance d to a modeled form of the Taylor micro-scale:

$$\Gamma = \frac{1}{2} \left(1 - \tanh \left[5 \left(\frac{\kappa}{\sqrt{C_\mu}} \eta^2 - 1 \right) - \phi \right] \right), \quad \eta = \frac{d}{\alpha_1 \lambda} \quad (14)$$

with the Taylor micro-scale defined as

$$\lambda = \sqrt{\nu / C_\mu \omega} \quad (15)$$

The primary advantage of this form is that the location of the RANS/LES juncture (defined as $\Gamma=0.5$) can be correlated as a function of the wall coordinate $d^+ = u_\tau d / \nu$. Substituting the log-law expression for the turbulence frequency $\omega = u_\tau / (\sqrt{\beta_*} \kappa d)$ into Eq. (15) and placing the result in Eq. (14), it can be shown that the $\Gamma=0.5$ position should occur at $d^+ = \alpha_1^2$ if $\phi = 0.0$. The constant α_1 then can be used control the position of the juncture, assuming that the log-law scaling is maintained. The value of “5” in Eq. (14) controls the sharpness of the transition, and the constant ϕ can be used to shift the mid-point of the blending function. In this work, ϕ is set to $\tanh^{-1}(0.98)$, so that the balancing position (where $\frac{\kappa}{\sqrt{C_\mu}} \eta^2 = 1$) corresponds to $\Gamma=0.99$ instead of $\Gamma=0.5$.

To determine the constant α_1 for a particular inflow boundary layer, the following procedure is used. First, a prediction of the equilibrium boundary layer is obtained, given free-stream properties, a specified wall condition (adiabatic or isothermal) and a value for the

boundary layer thickness, from Coles' Law of the Wall / Wake along with the Van Driest transformation:

$$\frac{u_{vd}}{u_\tau} = \frac{1}{\kappa} \ln(d_w^+) + C + 2 \frac{\Pi}{\kappa} \sin^2\left(\frac{\pi}{2} \frac{d}{\delta}\right), \quad d_w^+ = \frac{u_\tau d}{\nu_w} \quad (16)$$

with

$$u_{vd} = \frac{u_\infty}{A} \left\{ \sin^{-1} \left[\frac{2A^2 u / u_\infty - B}{\sqrt{B^2 + 4A^2}} \right] + \sin^{-1} \left[\frac{B}{\sqrt{B^2 + 4A^2}} \right] \right\}, \quad (17)$$

$$A = \sqrt{\frac{(\gamma-1)}{2} \text{Pr}_t M_\infty^2 \frac{T_\infty}{T_w}}, \quad B = \left[1 + \text{Pr}_t^{1/2} \frac{(\gamma-1)}{2} M_\infty^2 \right] \frac{T_\infty}{T_w} - 1$$

An initial estimate for the outer extent of the log layer is defined by finding the value of d_w^+ such

that $\left(\frac{1}{\kappa} \ln(d_w^+) + C \right) / \left(\frac{u_{vd}}{u_\tau} \right) = 0.98$. The value of $d^+ = u_\tau d / \nu$ that corresponds to this value of

d_w^+ is then found through the use of Walz's formula for the static temperature distribution within the boundary layer [25]:

$$\frac{T}{T_\infty} = \frac{T_w}{T_\infty} + \frac{(T_{aw} - T_w)}{T_\infty} \frac{u}{u_\infty} - r \frac{(\gamma-1)}{2} M_\infty^2 \left(\frac{u}{u_\infty} \right)^2 \quad (18)$$

Since the kinematic viscosity ν is a function of temperature, the target value for d^+ will differ significantly from d_w^+ for high Mach number flows. The selection of the constant is done in a pre-processing step, based on an inputted distribution of the boundary layer thickness versus streamwise distance obtained from a RANS solver. Table 1 shows streamwise distributions in the model constant for the cases described later. A reasonable estimate of the value of model constant can be obtained by considering only the first term in the fit, as the streamwise interval is generally small (~ 10 boundary layer thicknesses)

Table 1: Model constant versus streamwise distance

case	Model constant α_1
Babinsky, et al. [10]	$\alpha_1(x) = 27.35 + 39.02x - 19.21x^2$
Willis, et al. [26]	$\alpha_1(x) = 53.90 + 11.04x$
Gefroh, et al. [6]	$\alpha_1(x) = 38.46 + 49.78x$

A key to the blending function response is the relative insensitivity of the turbulence frequency to changes in the turbulence kinetic energy and the eddy viscosity. This means that the average location of the blending function (in terms of its distance from the wall) will not vary significantly. The dependence of the turbulence frequency on the vorticity S means that the instantaneous position of the interface will vary in response to resolved-eddy dynamics. The calibration procedure described above is specific to a particular inflow boundary layer and is not guaranteed to adjust properly as the flow transitions from one equilibrium state to another. An improved method that does not require a problem-specific calibration has been developed and is undergoing evaluation [27] but has only been used for the case presented in Section 6.6.

3.3. Recycling-Re-scaling Method

A recycling / rescaling technique, applied to the fluctuating fields, is used to initiate and sustain turbulent structures. In this procedure, fluctuations in the fluid properties at a ‘recycle plane’ are extracted by subtracting the instantaneous profile from a time- and span-averaged profile. The fluctuation fields are then rescaled according to boundary layer similarity laws and superimposed onto a RANS mean inflow profile. The general procedure is described in [15]. One modification used in this work to prevent excessive turbulence energy accumulation in the outer part of the boundary layer is to multiply the recycled fluctuations by a Klebanoff-type intermittency function [28]:

$$\begin{aligned} q_{\text{inflow}} &= q_{\text{RANS}} + F_{\text{kleb}} q'_{\text{recyc}}; \quad q = \text{density, velocity, temperature} \\ q_{\text{inflow}} &= (1 - F_{\text{kleb}}) q_{\text{RANS}} + F_{\text{kleb}} q'_{\text{recyc}}; \quad q = \text{turbulence variables} \\ F_{\text{kleb}} &= (1 + (d/C_{\text{kleb}} \delta)^6)^{-1} \end{aligned} \quad (19)$$

with $C_{\text{kleb}} = 1.10$. This procedure also ensures that the RANS free-stream inflow properties are not altered outside the boundary layer. We also require that recycled temperature fluctuations be no greater (in magnitude) than allowed by Morkovin’s hypothesis of negligible total-temperature fluctuations. From Morkovin’s hypothesis,

$$\begin{aligned} C_p T'_{\text{mork}} &= -[F_{\text{kleb}} (u_{\text{RANS}} u'_{\text{recyc}} + v_{\text{RANS}} v'_{\text{recyc}} + w_{\text{RANS}} w'_{\text{recyc}}) + \\ &\quad \frac{1}{2} F_{\text{kleb}}^2 (u'^2_{\text{recyc}} + v'^2_{\text{recyc}} + w'^2_{\text{recyc}})] \end{aligned} \quad (20)$$

and the recycled temperature fluctuation is limited as follows:

$$T'_{\text{recyc}}|_{\text{lim}} = F_{\text{kleb}} T'_{\text{recyc}} \min(1.0, \left| \frac{T'_{\text{mork}}}{F_{\text{kleb}} T'_{\text{recyc}}} \right|), \quad F_{\text{kleb}} T'_{\text{recyc}} \neq 0 \quad (21)$$

The density fluctuation is determined as follows. First, a provisional value of the pressure fluctuation is determined from the recycled density fluctuation:

$$p'_{\text{prov}} = R[\rho_{\text{RANS}} T'_{\text{recyc}}|_{\text{lim}} + F_{\text{kleb}} \rho'_{\text{recyc}} (T_{\text{RANS}} + T'_{\text{recyc}}|_{\text{lim}})] \quad (22)$$

The pressure fluctuation is then limited to be a specified multiple of the pressure (2% in this case):

$$p'_{\text{prov}}|_{\text{lim}} = \text{sgn}(p'_{\text{prov}}) \min(|p'_{\text{prov}}|, 0.02 p_{\text{RANS}}) \quad (23)$$

and a corrected value of the density fluctuation is determined from the limited pressure fluctuation:

$$\rho'_{\text{recyc}} = (p'_{\text{prov}}|_{\text{lim}} - \rho_{\text{RANS}} R T'_{\text{recyc}}|_{\text{lim}}) / (T_{\text{RANS}} + T'_{\text{recyc}}|_{\text{lim}}) \quad (24)$$

A further modification is motivated by the fact that quasi-periodic inflow-generation methods tend to ‘fix’ the positions of longitudinal vortical structures within the boundary layer over long times. This problem is exacerbated by the RANS component of the closure, which attenuates smaller-scale near-wall structures that might otherwise act to break up the quasi-periodic behavior. One way to avoid this is by shifting the plane containing the fluctuation fields in the spanwise (Z) direction by some fraction of the incoming boundary layer thickness δ . This shift is determined by a profile of shifting distance versus time that is produced by sampling Gaussian distributions corresponding to an average near-wall streak length (3-5 δ) and the

shifting-distance itself. To produce this profile, the average near-wall streak length (usually 3-5 boundary layer thicknesses) is converted to an increment in time by dividing the value by the convective velocity (taken as 80% of freestream velocity). Standard deviations for the streak-length and spanwise- shifting Gaussian distributions are taken as 1.0δ and as 0.5δ , respectively. The procedure results in a random sequence of shifts at discrete time intervals. This discrete distribution is converted to a continuous one by linearly interpolating between each discrete point. A typical distribution of shifting distance (normalized by δ) versus normalized time is shown in Figure 1. Ref. [29] shows that this procedure does act to homogenize the time-averaged flow in the spanwise direction while not significantly affecting turbulent statistics. The ‘Z-shifting’ technique was only used for the simulations of the Willis, et al. [26] and Gefroh, et al. [6] experiments.

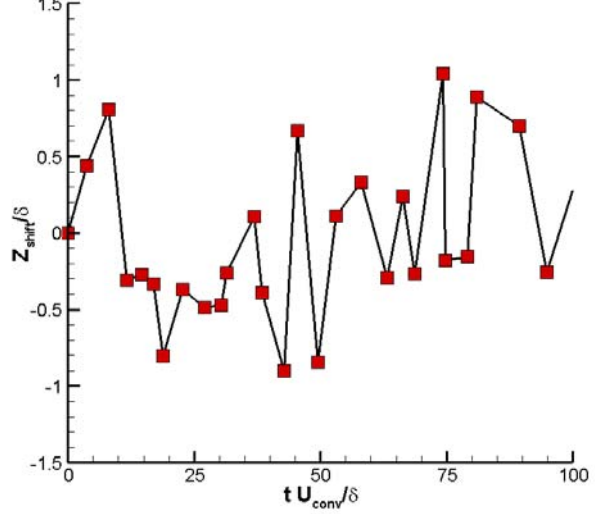


Figure 1: Spanwise shifting distance versus time

4. Immersed Boundary Method

In the present work, the IB method developed in Choi et al. [17] is extended to handle compressible, turbulent flows. The immersed surface is generated as a cloud of points which can be structured or unstructured. The entire flow domain is then classified into three categories of cells. Cells sufficiently removed from the immersed boundary are termed as ‘field’ cells, cells very near but not inside the immersed object are ‘band’ cells, and cells inside the immersed body are ‘interior’ cells. To perform this classification, a distance function to the nearest surface point for all cells (within a ‘bounding box’ of the IB) is computed using an approximate nearest neighbor-search algorithm. Concepts from computational geometry are then used to impose an unambiguous sign to the distance function (thus deciding ‘inside’ or ‘outside’ for closed surfaces). A ‘direct forcing’ approach is used to enforce the boundary conditions at the interior and band cells. This results in the residual form of the equation system shown below which is then solved implicitly, coupled with exterior cells, by use of sub-iteration techniques.

$$R_i^{n+1,l} = (1 - G(\Phi^{n+1}))R_{i,NS}^{n+1,l} + G(\Phi^{n+1}) \left[\frac{V_i^{n+1,l} - V_{B,i}^{n+1,l}}{\Delta t} \right] = 0 \quad (25)$$

This equation represents the blending of the Navier-Stokes residual with a source term that relaxes the primitive variable vector $V = [p, u, v, w, T, k, \omega]^T$ to its band-cell values. The quantity $G(\Phi)$ is a sharp Heaviside function (set to 1 for ‘band’ and ‘interior’ cells and zero otherwise), Φ is the signed distance function, and l is a sub-iteration index. Field cells are defined as those with $G = 0$ and $\Phi > 0$, while band cells are those with $G = 1$ and $\Phi < 0$, and interior cells are

those with $G = 1$ and $\Phi < 0$. The Navier-Stokes equations are solved in the field cells, fluid properties are generally held fixed in the interior cells, and analytic forms for the fluid properties (discussed later) are prescribed in the band cells.

4.1. Cell Classification Procedure

The first step in the IB method is to define an immersed body as a collection of surface points. This can be done using a CAD format or through other means, but the key is that for each separate component (separate in the sense that different components may move at different rates), a list of surface points and outward-pointing unit normals is created. The next step is to calculate the signed distance from each field point \vec{x}_k to the nearest surface point on each surface $\vec{x}_{s,l(k)}$. This is accomplished first through the use of approximate nearest-neighbor searching techniques [30], which return the unsigned distance. In practice, this is done only for the number of field points that are within a “bounding box” surrounding the particular surface, as it is these points that are likely to be influenced immediately by the body. Distances outside the “bounding box” are assigned to be a very large positive number. For the cases presented in this report, the signed distance function is obtained by multiplying the unsigned distance with the sign of the dot product of the distance vector with the outward normal:

$$\Phi_s(\vec{x}_k, t) = \text{sgn}((\vec{x}_k - \vec{x}_{s,l(k)}) \cdot \vec{n}_{s,l(k)}) \times |\vec{x}_k - \vec{x}_{s,l(k)}| \quad (26)$$

Other approaches [17] can be used for more complicated CAD-based objects.

To define a global signed distance function at any given mesh point $(\Phi(\vec{x}_k, t))$, a simple priority rule is exercised. First, the global distance function is initialized to a large number. Then, the global signed distance function at a particular point is taken as the minimum of the individual signed distance functions at that point:

$$\Phi(\vec{x}_k, t) = \min_s (\Phi_s(\vec{x}_k, t)) \quad (27)$$

The collections of points that comprise the surfaces are allowed to move according to prescribed rate laws. Once new surface positions are obtained, the preceding and following steps for developing the signed-distance and Heaviside functions have to be repeated.

The Heaviside function $G(\Phi(\vec{x}, t))$ is defined to be one for points just outside the immersed body and within the immersed body and is zero otherwise. The calculation of the Heaviside function is initiated by first initializing $G(\Phi(\vec{x}_k, t)) = 0$ for all points \vec{x}_k . Then, given a point \vec{x}_k , if $\Phi(\vec{x}_k, t) > 0$ and if any $\Phi(\vec{x}_l, t) < 0$, where \vec{x}_l is a nearest-neighbor of \vec{x}_k , then $G(\Phi(\vec{x}_k, t))$ is set to 1. If $\Phi(\vec{x}_k, t) < 0$, then $G(\Phi(\vec{x}_k, t))$ is also set to 1. The set of “nearest-neighbors”, for a structured grid, is generally defined as the 26 cells that are immediately adjacent to a particular mesh cell (i,j,k), though smaller subsets can be used. As mentioned before, this process subdivides all of the mesh cells into

- a.) field points (those with $\Phi(\vec{x}_k, t) > 0$ and $G(\Phi(\vec{x}_k, t)) = 0$)
 - b.) band points (those with $\Phi(\vec{x}_k, t) > 0$ and $G(\Phi(\vec{x}_k, t)) = 1$), and
 - c.) interior points (those with $\Phi(\vec{x}_k, t) < 0$ and $G(\Phi(\vec{x}_k, t)) = 1$)
- (28)

4.2. Band Cell Interpolations

To extend the method of [17] to compressible flows, the following first-order accurate closures are considered for the fluid properties in the band cells, where the subscript ‘I’ indicates properties obtained at an interpolation point located along the normal line extending outward from the nearest surface point corresponding to the band cell in question (discussed later), and the subscript ‘B’ indicates the band-cell.

$$p_B = p(d_I)$$

$$u_{B,i} - u_{S,i} = u_{T,i}(d_I) \left(\frac{d_B}{d_I} \right)^k + u_{N,i}(d_I) c(\rho, d_I, d_B), \quad (29)$$

$$u_{N,i}(d_I) = (u_j(d_I) - u_{S,j}) \mathbf{n}_j \cdot \mathbf{n}_i, \quad u_{T,i}(d_I) = (u_i(d_I) - u_{S,i}) - u_{N,i}(d_I)$$

In these expressions, \mathbf{n}_i is the normal vector at the closest point on the body surface, d is a distance from the nearest surface point, $u_{S,j}$ is the velocity at the nearest surface point, and k is a power-law. The choice of k allows the model to replicate a turbulent velocity profile ($k=1/7$ or $1/9$) or a laminar profile ($k=1$). To obtain the temperature distribution near the surface, Walz’s relation for the temperature distribution within a compressible boundary layer is used [25]:

$$\frac{T_B}{T(d_I)} = \frac{T_w}{T(d_I)} + \left(1 - \frac{T_w}{T(d_I)} + \frac{r(\gamma-1)}{2\gamma RT(d_I)} [u_{T,i}(d_I)]^2 \right) \left(\frac{d_B}{d_I} \right)^k - \frac{r(\gamma-1)}{2\gamma RT(d_I)} [u_{T,i}(d_I)]^2 \left(\frac{d_B}{d_I} \right)^{2k} \quad (30)$$

$$\text{or } \frac{T_B}{T(d_I)} = 1 + \frac{r(\gamma-1)}{2\gamma RT(d_I)} [u_{T,i}(d_I)]^2 \left(1 - \left(\frac{d_B}{d_I} \right)^{2k} \right) \quad (\text{adiabatic wall})$$

In this, r is the recovery factor and $[u_{T,i}(d_I)]^2$ is the kinetic energy associated with the tangential velocity component at the interpolation point.

The function $c(\rho, d_I, d_B)$ that scales the normal velocity component in Eq. (29) is determined by enforcing a discrete form of the continuity equation at each band cell. In the immersed boundary method of Choi et al. [17], we adopt a locally-parallel flow assumption so that all flow properties in the region near the immersed surface are functions of the coordinate normal to the surface n . Decomposing the velocity into tangential components u_{T_1} and u_{T_2} (in directions T_1 and T_2) and normal component u_n (in direction n), we write the steady continuity equation as:

$$\nabla_T \cdot (\rho \vec{u}_T) + \frac{\partial(\rho u_N)}{\partial n} = 0, \quad \text{with } \nabla_T \cdot (\rho \vec{u}_T) = \frac{\partial(\rho u_{T_1})}{\partial T_1} + \frac{\partial(\rho u_{T_2})}{\partial T_2} \quad (31)$$

Applying the parallel-flow assumption and introducing the functional forms $f(n)$ and $g(n)$ to describe the distributions in tangential velocity and density from the interpolation-point location d_I to the wall (ie. $\vec{u}_T(n) = \vec{u}_T(d_I) f(n)$, $\rho(n) = \rho(d_I) g(n)$), we have

$$\nabla_T \cdot (\rho(d_I) \vec{u}_T(d_I)) f(n) g(n) + \frac{\partial(\rho u_N)}{\partial n} = 0 \quad (32)$$

Now consider the two control volumes Ω_1 and Ω_2 shown in Figure 2. Discretizing Eq. (32) over each of the control volumes gives the following system:

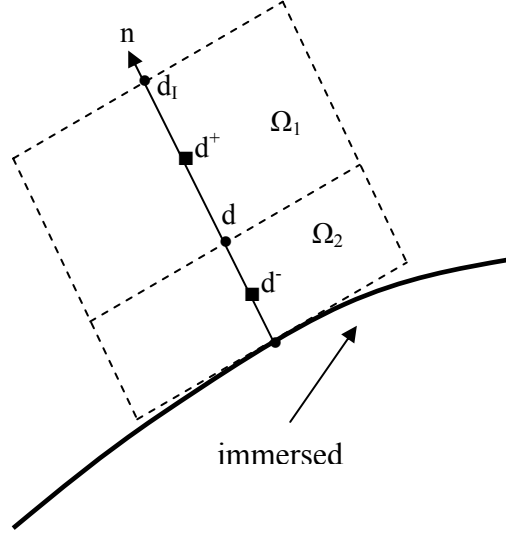


Figure 2: Schematic of control volumes used to define normal velocity component

$$\begin{aligned} \nabla_T \cdot (\rho(d_I) \vec{u}_T(d_I)) f(\tilde{d}^+) g(\tilde{d}^+) + \frac{\rho(d_I) u_N(d_I) - \rho(d_B) u_N(d_B)}{d_I - d_B} &= 0, \quad \Omega = \Omega_1 \\ \nabla_T \cdot (\rho(d_I) \vec{u}_T(d_I)) f(\tilde{d}^-) g(\tilde{d}^-) + \frac{\rho(d_B) u_N(d_B)}{d_B} &= 0, \quad \Omega = \Omega_2 \end{aligned} \quad (33)$$

with

$$\begin{aligned} \tilde{d}^+ &= \frac{1}{2} (d_I + d_B), \\ \tilde{d}^- &= \frac{1}{2} d_B \end{aligned} \quad (34)$$

Upon eliminating the common factor $\nabla_T \cdot (\rho(d_I) \vec{u}_T(d_I))$, Eq. (33) can be solved to obtain an expression for the normal velocity component at the band cell, $u_N(d_B)$:

$$\frac{u_N(d_B)}{u_N(d_I)} = \frac{\rho(d_I)}{\rho(d_B)} \left(\frac{\frac{d_B}{d_I} f(\tilde{d}^-) g(\tilde{d}^-)}{\frac{d_B}{d_I} f(\tilde{d}^-) g(\tilde{d}^-) + f(\tilde{d}^+) g(\tilde{d}^+) (1 - \frac{d_B}{d_I})} \right) \quad (35)$$

The closure is completed by substituting power-law and Walz / Crocco-type relations for $f(n)$ and $g(n)$:

$$f(n) = \left(\frac{n}{d_I} \right)^k, \quad g(n) = \frac{T_I}{T(n)} \text{ (from Eqs. (29) and (30)),} \quad (36)$$

by assuming that the pressure gradient normal to the surface is zero, and by evaluating the expression at the band-cell distance d_B . The result, for an adiabatic wall, is given as

$$\begin{aligned}
c(\rho, d_I, d_B) &= \frac{1}{\tilde{\rho}} \frac{\frac{d_B}{d_I} d^- \tilde{\rho}^-}{\left(\frac{d_B}{d_I} d^- \tilde{\rho}^- + \left(1 - \frac{d_B}{d_I}\right) \tilde{\rho}^+ \right)}, \\
d^- &= \left(\frac{d_B}{2d_I} \right)^k, \quad d^+ = \left(\frac{1}{2} \left(1 + \frac{d_B}{d_I}\right) \right)^k, \\
\frac{1}{\tilde{\rho}} &= 1 + \frac{r(\gamma-1)}{2\gamma RT(d_I)} [u_{T,i}(d_I)]^2 \left(1 - \left(\frac{d_B}{d_I}\right)^{2k}\right), \\
\frac{1}{\tilde{\rho}^-} &= 1 + \frac{r(\gamma-1)}{2\gamma RT(d_I)} [u_{T,i}(d_I)]^2 (1 - (d^-)^2), \\
\frac{1}{\tilde{\rho}^+} &= 1 + \frac{r(\gamma-1)}{2\gamma RT(d_I)} [u_{T,i}(d_I)]^2 (1 - (d^+)^2),
\end{aligned} \tag{37}$$

The turbulence variables in the band cells are defined as

$$\begin{aligned}
k_B &= u_\tau^2 / \sqrt{C_\mu}, \quad \omega_B = u_\tau / (\sqrt{C_\mu} \kappa d_B): \quad d^+ > 10.934 \\
k_B &= k(d_I) \left(\frac{d_B}{d_I} \right)^2, \quad \omega_B = 60\nu_w / (0.075 d_B^2): \quad d^+ < 10.934 \quad \text{or } k = 1 \\
d^+ &= u_\tau d_b / \nu_w, \quad u_\tau = |u_{T,i}(d_I)| / (\ln(d^+) / \kappa + 5.1) \quad (\text{iterative solution})
\end{aligned} \tag{38}$$

To arrive at this form, we assume equivalence between the result provided by the power-law profile and the law of the wall within the band cells. Some of the cases presented later use another variant of this procedure that replaces the pressure extrapolation (the first line in Eq. (29)) with the finite-volume solution of the continuity equation within the band cells. In the formulation of the continuity equation, the mass flux is set to zero at a cell interface if the distance function Φ changes sign across the interface. The continuity equation in the band cells evolves according to this constraint and to the specified velocity and temperature fields described above. This procedure ensures exact mass conservation but can sometimes lead to pressure oscillations within the band cells.

4.3. Determination of Information at the Interpolation Point

The preceding developments hinge on the determination of flow properties $\hat{q}(d_I)$ at a certain distance d_I away from the surface. Given a point within the band \vec{x}_k and a list of nearest neighbors to that point \vec{x}_l , a merit function w_l is defined as follows: (see Figure 3)

$$w_l = \frac{1}{\sqrt{(|\vec{x}_l - \vec{x}_k|)^2 - ((\vec{x}_l - \vec{x}_k) \cdot \hat{n}))^2} + \varepsilon} \quad \text{if } (\vec{x}_l - \vec{x}_k) \cdot \hat{n} > 0, \text{ and } w_l = 0 \text{ otherwise} \tag{39}$$

In this, $(\bar{x}_l - \bar{x}_k) \cdot \hat{n}$ is the projection of the distance from \bar{x}_k to \bar{x}_l in the direction of the outward normal, and $|\bar{x}_l - \bar{x}_k|$ is the magnitude of the distance vector itself. If point \bar{x}_l is located directly along the outward normal line corresponding to band point \bar{x}_k , and if $(\bar{x}_l - \bar{x}_k) \cdot \hat{n}$ is positive,

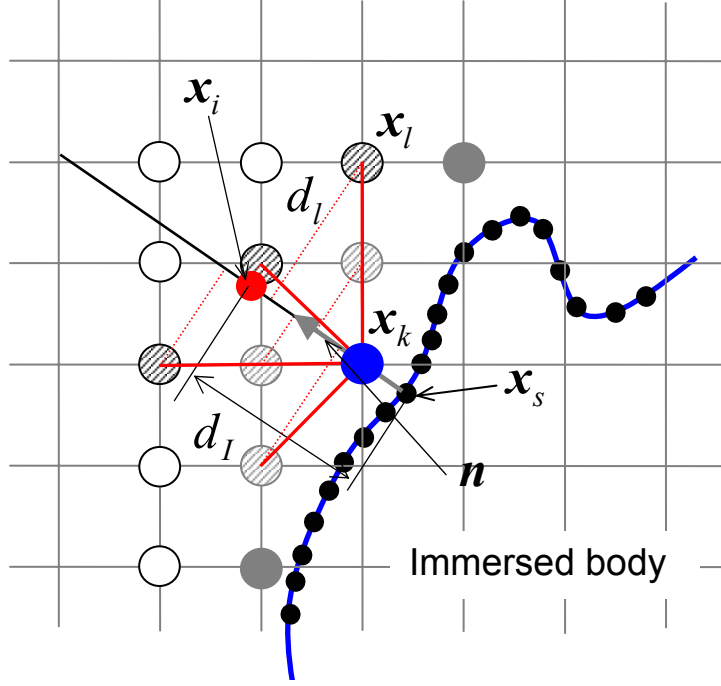


Figure 3: Schematic determination of the distance d_l between the interpolation point x_i and surface node point for a given band point x_k using the projected distance d_l from neighbor points x_l to outward normal line based on surface normal vector n at the immersed surface node x_s . Large closed circle represent the band point to be interpolated with the information at neighbor point. Hatched black and gray circles represent the field points and band points associated with the present determination, respectively.

meaning that point \bar{x}_l is further away from the surface than point \bar{x}_k , then the merit function returns a very large value ($\sim 1/\varepsilon$, where ε is 10^{-12})

The actual calculation of w_l is performed in three stages. First, only field points (those with $\Phi(\bar{x}_l, t) > 0$ and $G(\Phi(\bar{x}_l, t)) = 0$) are considered as members of the list of nearest neighbors. Then, w_l is calculated according to Eq. (39), and the sum of the weights $\sum_m w_m$ is calculated. If this sum is non-zero, then the actual weight function for each nearest-neighbor is determined as

$$\omega_l = \frac{w_l}{\sum_m w_m} \quad (40)$$

Otherwise, the process is repeated, now considering both field points and other band points as members of the list of nearest neighbors. If this application also results in no viable interpolation points being found, then the band point \bar{x}_k is effectively set to an interior point.

The location at which interpolated properties are defined, d_I , is calculated for a particular field point as

$$d_I = \sum_l \omega_l (\bar{x}_l - \bar{x}_k) \cdot \hat{n} \quad (41)$$

Note that this distance is in the direction of the normal coordinate. With this, the fluid properties $\hat{q}(d_I)$ are found by applying the weighting functions

$$\hat{q}(d_I) = \sum_m \hat{q}_m \omega_m \quad (42)$$

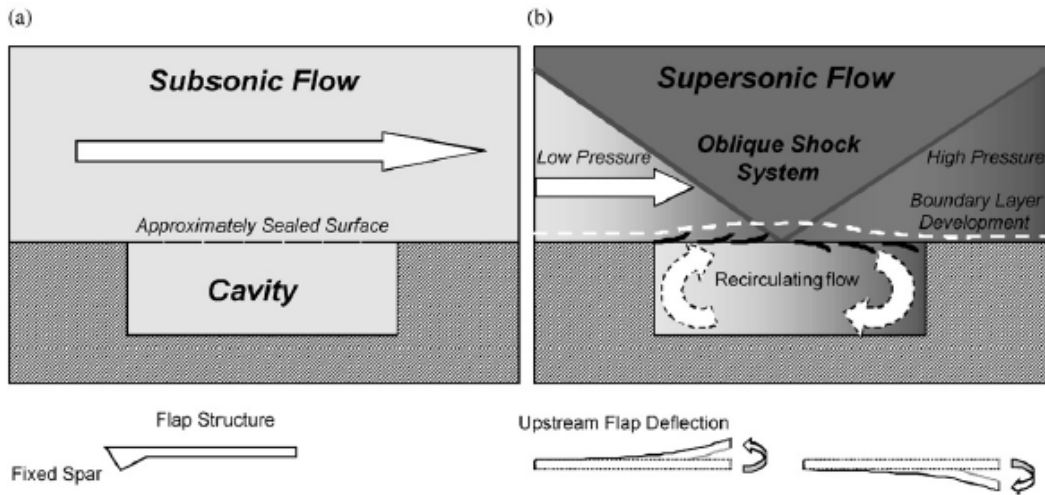


Figure 4. Aeroelastic mesoflaps over a cavity for (a) subsonic flow and (b) supersonic flow with impinging oblique shock. [6]

5. Fluid-Structure Interactions

One of the control devices simulated in the present study is an array of mesoflaps.[6-8] To simulate the flow control induced by an array of mesoflaps, a fluid structure interaction problem must be solved, as the mesoflaps deform dynamically due to the fluctuating surface loads. Figure 4 shows a schematic of a mesoflap system and its mode of operation. In this work, a loosely coupled approach is adopted for the fluid-structure interaction problem with separate solvers used for the fluid and structural domains.

5.1. Structural Solver: Beam Bending Equations

Each mesoflap is treated as an Euler-Bernoulli beam which is cantilevered at its upstream end and deflects due to the transverse (fluid) pressure loads acting on its surfaces. The mesoflaps are rendered as immersed objects in the computational domain, and their motion is

coupled with the flow solver using procedures outlined in the previous section. Figure 5 shows a schematic of a mesoflap and its beam model. The beam rendered as 1-D mesh (for each flap) has 101 equally spaced points and the mesh point distribution exactly matches that of the IB points on each mesoflap in the streamwise (x) direction. Two different governing equations are used for the structural problem, based on whether the interaction takes into account the inertia of the mesoflap system or neglects it. In general, the static deflection of the elastic line for the Euler-Bernoulli beam for a steady load is given by

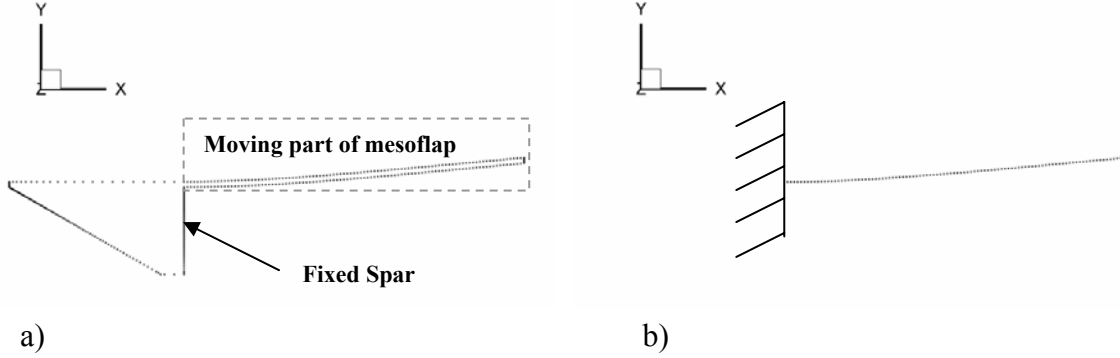


Figure 5: a) 2-D view of a mesoflap rendered as an IB, b) structural model of a mesoflap as a cantilevered beam

$$\frac{\partial^2}{\partial x^2} \left[EI(x) \frac{\partial^2 v(x)}{\partial x^2} \right] = f(x), \quad 0 < x < L \quad (43)$$

where v is the deflection, E is the modulus of elasticity, I is the area moment of inertia of the flap cross-section about the neutral axis, f is the applied transverse force/unit length and L is the beam or flap length. For a prismatic beam, the neutral axis is an imaginary line passing through the centroid of the cross-section about which the first moment of area (of the cross-section) is zero. The beam cross-section, which is same as the flap cross-section, is uniform and rectangular for which I is given by $\frac{1}{12}bt^3$, where b is the flap width and t is the flap thickness. As quantities are calculated on a unit width (of flap) basis in this work, f is derived on a per unit area basis, and I is given by $\frac{1}{12}t^3$. Since the beam-model used here accounts for deformation due to transverse loads only, shear forces on the mesoflap surfaces are not considered. The load f is thus the pressure acting on the flap surface. In the case when the dynamics of the beam is considered and time-varying loads are accounted for, the governing equation is that of a vibrating beam ,

$$-\frac{\partial^2}{\partial x^2} \left[EI(x) \frac{\partial^2 v(x,t)}{\partial x^2} \right] + f(x,t) = m(x) \frac{\partial^2 v(x,t)}{\partial t^2}, \quad 0 < x < L \quad (44)$$

where $m(x)$ is the mass per unit length of the beam. Central differences are used for the discretization of the fourth order equation [31] resulting in a semi-discretized system,

$$EI[K']\{v\} + \rho A[I]\{\ddot{v}\} = f \quad (45)$$

where $[K']$ is the discrete fourth order differential operator for the entire beam, ρ is the density of the beam and A is the area of the beam per unit depth which is effectively equal to the height of the beam (t) in this case. The discretization of the temporal derivative for this problem is done using Newmark's average acceleration method [32]

$$\begin{aligned}\dot{v}^{n+1} &= \dot{v}^n + \Delta t \left((1-\gamma)\ddot{v}^n + \gamma\ddot{v}^{n+1} \right) \\ v^{n+1} &= v^n + \Delta t \dot{v}^n + \frac{1}{2}(1-2\beta)\Delta t^2 \ddot{v}^n + \beta\Delta t^2 \ddot{v}^{n+1}\end{aligned}\tag{46}$$

In the above equation, the superscript n denotes the time step, and β and γ are the Newmark parameters. For the average acceleration method, which is fully implicit, unconditionally stable and is second order accurate, $\beta = \frac{1}{4}$ and $\gamma = \frac{1}{2}$. The use of Eq. (45) in Eq. (46) results, after some rearrangement, in the following equation,

$$\begin{aligned}[K_{eff}]\{v^{n+1}\} &= f + \rho A [I] \left(\frac{1}{\beta\Delta t^2}\{v^n\} + \frac{1}{\beta\Delta t}\{\dot{v}^n\} + \left(\frac{1}{2\beta}-1\right)\{\ddot{v}^n\} \right) \\ [K_{eff}] &= \frac{1}{\beta\Delta t^2} \rho A [I] + [K]\end{aligned}\tag{47}$$

where $[K] = EI[K']$ is a coefficient matrix which is similar to the stiffness matrix as computed in finite element computations. For the case of a quasi-steady problem, which does not involve any time dependant terms, the resulting matrix equation to solve is given by,

$$EI[K]\{v^{n+1}\} = f\tag{48}$$

This results in a coefficient matrix $[K]$ which is not diagonally dominant for the quasi-steady case and a direct solver using Gaussian elimination with partial pivoting is used to solve for the displacements. For the dynamic problem, the coefficient matrix is dependent on the time step based on which the matrix may or may not be diagonally dominant.

5.2. Fluid-Structure Coupling

5.2.1. Determination of loads on flap surfaces from neighboring fluid cells

One of the primary steps involved in the coupling of the fluid and structural solvers is the determination of loads on the surface of the structure. As the mesoflaps are modeled as Euler-Bernoulli beams in this study, only the transverse loads acting on the top and bottom surfaces of the mesoflaps need to be determined. The procedure adopted in determining the load is as follows. The mesoflaps and supporting structures (Figure 5) are rendered as immersed objects in the fluid domain which implies that there will be *band* points in the fluid domain that have their nearest surface points on a flap surface. So for each band point in the domain, it is checked if the nearest IB surface point is a mesoflap upper or lower surface. If this is true, then the data stored at the *interpolation* point (for the given band point) is projected to the surface point on the mesoflap. In the case that a surface point (on the mesoflap) is closest to more than one *band* point, then the pressure value from the interpolation point which is closer to the surface point is considered. This procedure results in a sparsely populated pressure data set for each of the

mesoflap surfaces, which is then reconstructed using a bi-linear interpolation to obtain complete surface-load data. This is elaborated upon in the next section.

5.2.2. Interpolation of loads

A bi-linear interpolation approach – linear interpolation with sweeps in the streamwise and spanwise direction -- is adopted for the reconstruction of the load on the mesoflap surfaces. This is done after a partially populated load is obtained on the mesoflap surface as outlined in the previous section. Figure 6 shows a schematic of the interpolation scheme used to reconstruct the load on the mesoflap surfaces. Figure 6 shows an array of IB points rendering the mesoflap surface, with ‘i’ denoting the streamwise direction and ‘j’ the spanwise direction. Load values are computed by first doing a sweep in the ‘i’ direction and then in the ‘j’ direction. In the ‘i’ direction, an interpolation based on curved surface distances is used to compute the interpolated load with data available from the nearest (populated) right and left neighbors. This will populate the load values at all the points on those rows (fixed ‘j’ value) where there is some initial data but will not affect the ones without any initial load. Thus, following the ‘i’ sweep, a sweep in the ‘j’ direction is performed in which a linear interpolation is done using straight-line distances. This sweep ensures that all the IB points on the flap top and bottom surfaces are populated with

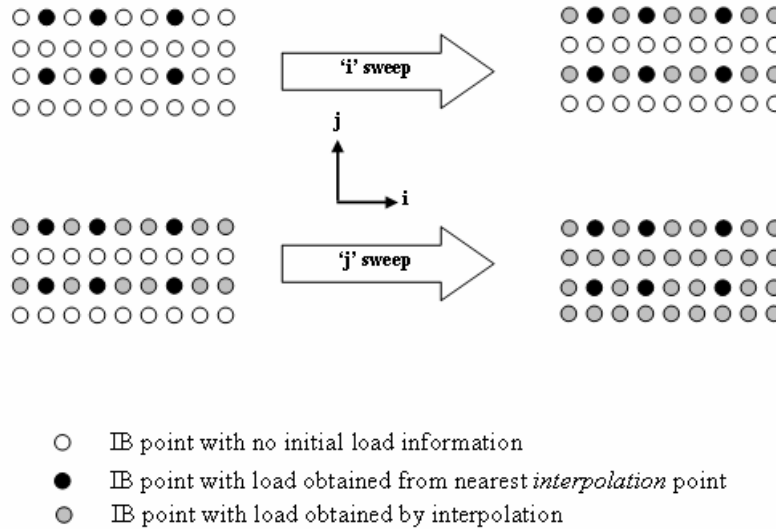


Figure 6: Schematic representation of interpolation scheme used in the reconstruction of surface loads on mesoflap upper and lower surfaces

load values. The choice of using curvi-linear distances in the streamwise (‘i’) direction and linear distances in the spanwise (‘j’) direction is made as the flap has a curved shape in the ‘i’ direction but is flat in the ‘j’ direction. To obtain load values at the points which have only one populated neighbor (specifically the points at the edge), a first order extrapolation is used.

5.2.3. Fluid-structure iteration

Once the interpolation of loads is done, a fully populated array of loads is obtained for the upper and lower surfaces for each mesoflap. A span-averaged 1-D load distribution is then obtained for each mesoflap which is transferred to the beam solver. The beam solver updates the

deflection and velocity of the beam based on the new loads by solving Eq. (43) (quasi-steady) or Eq. (44) (dynamic), which is then used to obtain a new configuration for the mesoflap. This structural iteration can be summarized as follows:

- Determination of loads at (some) discrete IB points on the flap surfaces using band point and interpolation point data.
- Interpolation of loads to obtain a complete data set for the IB points rendering the mesoflap upper and lower surfaces.
- Calculation of a span-averaged 1-D load distribution for the discretized beam.
- Invocation of the beam solver: computation of new position and velocities of mesoflap
- Reclassification of fluid domain into field, band and interior cells.

The frequency at which a structural iteration, is done depends on whether a quasi-steady or fully dynamic fluid-structure interaction problem is being solved. For the quasi-steady 2-D simulation this is done after every 2500 iterations of the fluid solver which is considered sufficient to obtain a reasonably converged intermediate fluid solution. The process of updating the configuration of the mesoflaps (after every 2500 fluid-solver cycles) is continued until a convergence criterion is met for the computed displacements. This is evaluated in the following way:

- At every structural iteration, the maximum change in displacement of each mesoflap (compared to the previous configuration) is computed.
- It is then checked whether this value is less than a specified tolerance, which is chosen as 10% of the flap thickness [32]. If this is true for all the mesoflaps then the fluid-structure interaction is assumed to be converged
- A final fluid solution is obtained for the converged configuration of the mesoflap system.

For the fully dynamic approach, a structural iteration is done at each time step (every fluid iteration).

5.2.4. Fluid-solver changes

A couple of changes are adopted for the fluid solver to facilitate the smooth running of the fluid-structure interaction problem when the dynamics of the structure is considered. These are listed below

- A reduced order of time integration (Euler implicit) is used for the fluid cells in the vicinity of the immersed surfaces.
- For the baseline IB method as applied to non-moving geometries, the solution in the interior cells is fixed somewhat arbitrarily and not as function of the solution of neighboring cells. This approach was making the solution unstable for the moving IB surfaces investigated herein. A possible reason for this is as follows. As the continuity equation is integrated for the *band* cells in this method, this requires the knowledge of flow properties stored at these *band* cells at the previous time step (for updating and residual construction). For the case in which a cell changes from being an *interior* cell to a *band* cell, the values being used for the residual construction may not be consistent. To address this issue, the reconstruction of the solution in the *interior* cells which are neighbored by a *band* cell has been modified. If any interior cell has as its neighbor a *band* cell, then its properties are evaluated by interpolating the values of its neighboring

band cells using an inverse distance weighting approach. This is similar in concept to the treatment used for simulation of moving bodies by Balaras [33].

6. Results

6.1. Overview

Three main sets of experiments are simulated in this work. The first set of experiments was conducted at Cambridge University [10] and involved supersonic flow over single micro VGs as well as impinging oblique shock interactions with and without micro VG effects. The second set of experiments was conducted at NASA Glenn Research Center [26,34] and involved flat plate boundary layer flows with bleed effects and impinging oblique shock interactions with and without bleed. The third set of experiments was performed at the University of Illinois [6-8] and involved impinging oblique-shock interactions with and without meso-flap flow control. Results from simulations of each of these experiments are described in detail in the following sections. A collaboration with NASA Langley led to the use of the immersed-boundary flow solver to investigate linear stability of laminar flows influenced by boundary layer trip elements. This work will be discussed in brief, as will results from a workshop study that applied the IB method to simulate the effects of a shock generator.

Free-stream conditions and inflow boundary layer properties for the three main sets of experiments are summarized in Table 2.

Table 2: Inflow boundary layer properties

Parameter	Babinsky, et al.	Willis, et al.	Gefroh, et al.
M_∞	2.5	2.46	2.41
p_o (Pa)	3.056e6	1.724e6	5.026e6
T_o (K)	290.0	293	300
Re/m	30.0e6	17.5e6	50.4e6
δ_o (cm)	0.6	2.63	0.4

6.2. Micro VG Control of Shock / Boundary Layer Interactions

The first set of calculations described in this work correspond to experiments that examine the effects of micro vortex generators (micro VGs) in controlling shock / boundary layer interactions. Here, the individual vortex generators (up to 3) are rendered as immersed objects. The following sections are excerpted from papers P-1 and P-5 in the publication list (Section 9).

6.2.1. Experiment details

Experiments involving the effects of micro VGs on shock interaction control have been performed at Cambridge University by Dr. Holger Babinsky and his students. The experiments were performed at a nominal Mach number of 2.5, a stagnation temperature of 290 K, and a Reynolds number / meter of 30×10^6 . The test section in the wind tunnel is 90 mm high and 110 mm wide. Data collected in these experiments includes pitot pressure surveys, wall static

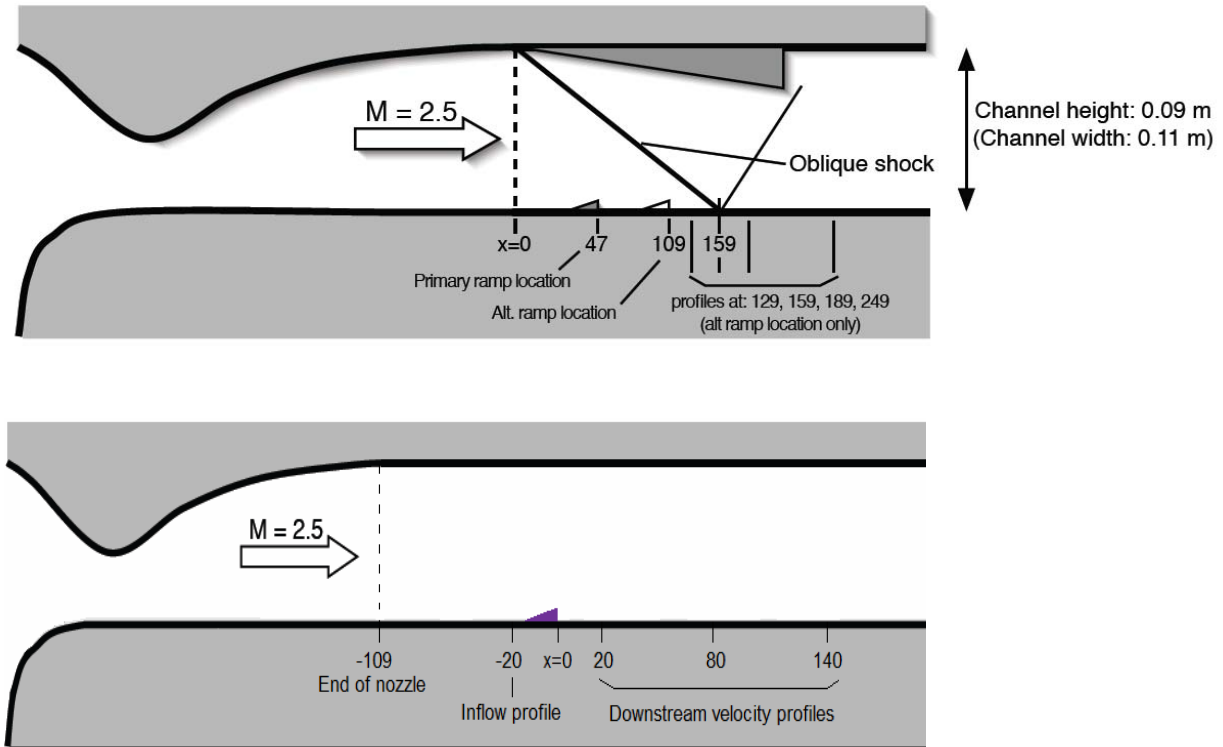


Figure 7: Schematic of Cambridge University wind tunnel showing the locations of the data stations, VG positions, and shock generator (provided by H. Babinsky)

pressure distributions, and axial velocity profiles obtained at various streamwise and spanwise stations using laser Doppler anemometry (LDA). Of the cases considered in the Cambridge database, this paper focuses on three experiments:

1. Mach 2.5 flow over single wedge-shaped micro VGs of heights $h = 3$ mm and $h = 6$ mm (LDA velocity data, Schlieren imaging, surface oil-flow)
2. An oblique shock / turbulent boundary layer interaction at Mach 2.5 induced by a 7-degree wedge placed on the upper wall of the wind tunnel (LDA velocity data, surface pressure measurements, Schlieren imaging, surface oil-flow)
3. The same oblique shock / turbulent boundary layer interaction with the addition of an array of three micro VGs with heights $h = 3$ mm upstream of the shock impingement point (LDA velocity data, surface pressure measurements, Schlieren imaging, surface oil-flow)

Figure 7 shows the general arrangement of the VG arrays within the Cambridge wind tunnel. For the experiments considered herein, the trailing edge of each micro VG was located 108.5 mm downstream of the start of the test section. The leading edge of the shock generator was also placed at the start of the test section, resulting in a lower-wall shock-impingement position of 159 mm, assuming inviscid flow. Velocity profiles were collected at streamwise stations of $X = 20$ mm, $X = 80$ mm, and $X = 140$ mm, with the X coordinate measured from the trailing edge of the micro VG. Additional profiles were collected at $X = -20$ mm (in the absence of the VG) to determine the inflow boundary layer characteristics, and at $X = 50$ mm for the shock-impingement cases. The nominal boundary layer thickness at the inflow plane ($X = -20$ mm) is around 6.5 mm. At each of the streamwise stations, LDA data was recorded at three or four spanwise stations (with $Z = 0$ mm being the tunnel centerline) as indicated in Table 3. The dimensions and alignment of the wedge-shaped micro VGs in the experiments are based on [9] and [10].

Table 3. Spanwise location of data stations for different micro VG sizes with / without shock interaction

Experiment	Spanwise data locations (Z , mm)
Mach 2.5 flow over 6 mm micro VG	0.0, 4.5, 9.0, 18.0
Mach 2.5 flow over 3mm micro VG	0.0, 2.3, 4.5, 9.0
Mach 2.5 shock / boundary layer interaction (3 x 3 mm micro VG array)	0.0, 4.5, 9.0

6.2.2. Computational domain and calculation details

Two computational domains have been used for the simulations described in this work. The first domain, used for the single micro-VG calculations and for the ‘idealized’ SBLI simulations described later, ranges from $\bar{X} = -108.5$ mm to $\bar{X} = 262.75$ mm in the streamwise direction (with the \bar{X} coordinate measured with respect to the start of the wind-tunnel test section), from $Y = 0$ mm to $Y = 90$ mm in the normal direction, and from $Z = -22.5$ mm to $Z = 22.5$ mm in the spanwise direction. The mesh spacing in the \bar{X} and Z directions is 0.5 mm, and a minimum spacing of 0.005 mm is enforced at the lower wall. The total mesh size is $747 \times 200 \times 90 = 13.45$ million interior mesh cells. Slip wall conditions are prescribed on the upper boundary ($Y = 90$ mm), extrapolation conditions are prescribed at the outer boundary ($\bar{X} = 262.75$ mm), periodic boundary conditions are applied at $Z = \pm 22.5$ mm, and no-slip, adiabatic-wall boundary conditions are applied at $Y = 0$ mm. For the SBLI simulations, the shock-generator leading edge is placed at $\bar{X} = -13$ mm, leading to a lower-wall impingement position of $\bar{X} = 146$ mm. This value is consistent with Schlieren imaging data (H. Babinsky, personal communication) and with full-wind tunnel simulations (discussed later) and accounts for the effects of the upper-surface boundary layer in modifying the shock inception point.

The second computational domain renders the Cambridge blow-down wind tunnel in two parts. The first part encompasses one half of the entire wind tunnel, including the nozzle and test section. Coordinates of the nozzle were provided by Dr. Babinsky and were spline-fitted for use in the mesh-generation exercise. The mesh is clustered to the upper wall, the lower wall ($Y = 0$ mm), and to one side wall ($Z = 55$ mm) (centerline symmetry being assumed) with a minimum spacing of 0.005 mm. Uniform mesh spacing at a value of 0.5 mm is used from $Z = 0$ to $Z = \sim 50$ mm, and a power-law mesh-clustering function is then used to connect this spacing to the

wall spacing of 0.005 mm. The mesh spacing in the \bar{X} direction is 1.0 mm, and the total number of interior mesh cells is $840 \times 225 \times 130 = 24.57$ million cells. A steady RANS calculation was performed on this mesh to obtain accurate inflow conditions for refined simulations of the flow in the test section. The test-section computational domain extends from $\bar{X} = -121.75$ mm to $\bar{X} = 252.75$ mm and has a spacing of 0.5 mm in the streamwise direction. The 7-degree shock generator is placed on the upper wall in this configuration (with the leading edge at the start of the test section as in the experiment). The numbers of mesh points and the stretching patterns in the Y and Z directions are identical to that used in the full wind-tunnel grid, and the total number of interior mesh cells is $750 \times 225 \times 130 = 21.94$ million cells. The wedge-shaped micro VGs are rendered separately as immersed boundaries using a simple structured surface mesh for each VG. The present implementation of the distance-function calculation requires a relatively fine surface mesh for accurate results. For the VG array (three 3 mm VGs), a total of 2234907 surface points is used, while for the 6 mm VG array, a total of 2964240 points is used.

Convergence of the RANS calculations was ascertained using three measures: relative decrease in residual norm, constancy of surface quantities, and constancy of the global mass flow rate. All RANS cases reached a steady-state solution. For the cases performed on the idealized domain, a flat-plate simulation at the test-section conditions was performed to determine the place at which the predicted boundary layer properties most closely matched the experimental values at $X = -20$ mm. The inflow plane used in the calculations was then extracted from the flat plate solution at a location 88.5 mm upstream of the matching position. The LES/RANS calculations were initiated by super-imposing scaled boundary-layer fluctuations from an earlier calculation onto part of a converged RANS solution. After several flow-through times to eliminate initial transients, time-averaged statistics for the LES/RANS calculations were collected over a minimum of 0.007s (10.7 flow-through times based on a domain length of 371.25 mm and a free-stream velocity of 570 m/s).

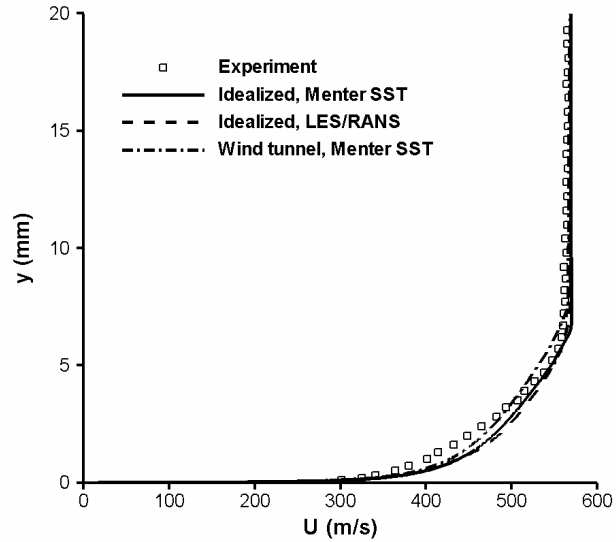
The different cases considered in this part of the study are summarized in Table 4.

Table 4: Summary of cases: SBLI with micro VGs

Case	Domain	Grid size	Turbulence Model(s)	IB details
1. Mach 2.5 flow over 6 mm micro VG	Periodic	13.45 M	RANS (Menter BSL), LES/RANS	$k=1,1/7,1/9$ (compressible) $k=1/7$ (compressible, mass conservative)
2. Mach 2.5 flow over 3 mm micro VG	Periodic	13.45 M	RANS (Menter BSL), LES/RANS	$k=1/7$ (compressible, mass conservative)
3. Mach 2.5 SBLI	Wind Tunnel	21.94 M	RANS (Menter SST)	None
4. Mach 2.5 SBLI with micro VG array	Wind Tunnel	21.94 M	RANS (Menter SST)	$k=1/7$ (compressible, mass conservative)
5. Mach 2.5 SBLI	Periodic	13.45 M	RANS (Menter SST), LES/RANS	None
6. Mach 2.5 SBLI with micro VG array	Periodic	13.45 M	RANS (Menter SST), LES/RANS	$k=1/7$ (compressible, mass conservative)

6.2.3. Inflow boundary layer

Inflow velocity profiles were measured at $X = -20$ mm in the absence of the micro VG array. Figure 8 compares inflow velocity profiles obtained on the idealized domain (RANS and LES/RANS), the wind tunnel domain (RANS), and in the experiment. Compared with the experiment, the computed profiles show consistently larger values of velocity in the inner part of the boundary layer, which implies lower values of the displacement and momentum thicknesses. The velocity profile obtained from the wind-tunnel calculation is somewhat thicker than the profiles obtained on the idealized domain. The LES/RANS and RANS predictions are very similar, with the LES/RANS profile showing slightly higher values of velocity in the near-wall region.



**Figure 8: Inflow boundary layer profiles
($X = -20$ mm)**

6.2.4. Immersed-boundary model assessment: Mach 2.5 flow over single micro VG

To assess the immersed boundary technique, results obtained using variations of the IB method are compared with a solution obtained on a body fitted grid and with experimental data for Mach 2.5 flow over a 6 mm micro VG. The body-fitted grid was generated using the commercial software GRIDGEN and contains 13.2 million cells, clustered to each solid surface with a minimum spacing of 0.005 mm. The \bar{X} extent of the body-fitted mesh ranges from -108.5 mm to 224.5 mm. Contour plots of Mach number at $X = 2$ mm and $X = 90$ mm and centerline plots of axial velocity at $X = 20$ mm and $X = 80$ mm are used in the assessment. The scale for the contour plots ranges from 0 to 2.85, with 0 being the darkest contours.

Mach number contours just downstream of the micro VG trailing edge at $X = 2$ mm (Figure 9) clearly show the initial growth of the primary vortex cores. The spanwise extent of the low momentum region is more pronounced for the $k=1$ interpolation and is least for the solution obtained on the body-fitted mesh. The vortices lift off less in the IB solutions and spread more laterally compared to the body-fitted mesh solution. Also, the higher-momentum flow reaches closer to the wall for the body-fitted mesh solution. This implies a stronger interaction between the vortex cores and the external flow. The presence of a secondary pair of vortices formed in the near-wall region downstream of the micro VG trailing edge is indicated by darker contours near the surface. The exact shape of the wake as predicted on the body-fitted grid is not very well matched by any of the RANS IB solutions, but a trend toward improved results with lower values of k is evident. LES/RANS results using $k=1/7$ and the mass-conservative IB are the closest to the body-fitted mesh RANS solutions.

At $X = 90$ mm (Figure 10), the vortex pairs generated behind the micro VG spread out and lift from the surface, and the lower-momentum core region becomes less pronounced, as

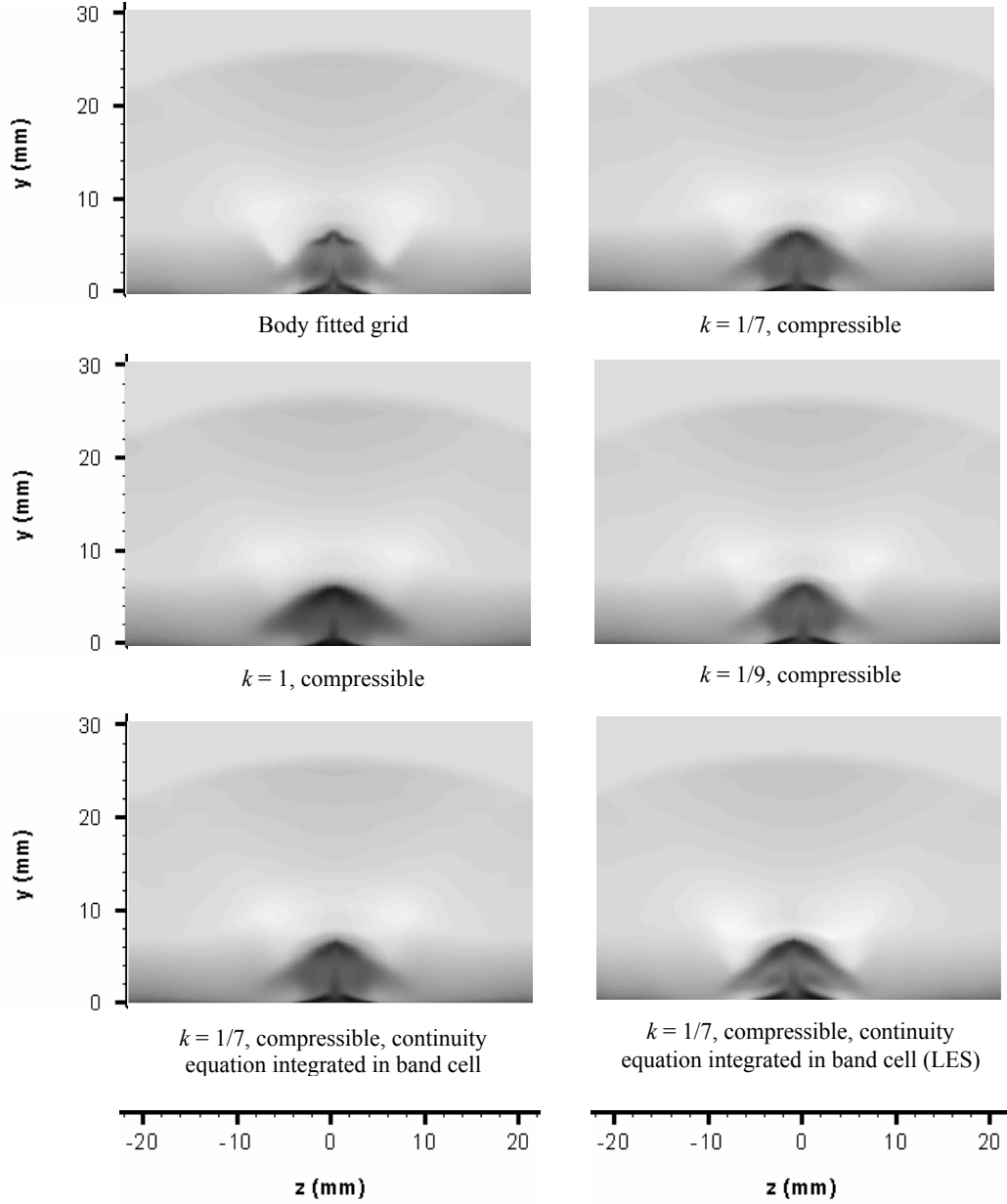


Figure 9: Mach contours at $X = 2$ mm for 6 mm VG placed in supersonic boundary layer

suggested by the lighter contours. The body-fitted solution again shows a narrower and taller low-momentum region, but the differences between this solution and the IB solutions are less apparent than at $X = 2$ mm. The low-momentum region is larger for the $k=1$ interpolation than for the others, implying that this ‘laminar’ choice might not provide enough flow attachment to the micro VG surface. The LES/RANS solution shows generally higher velocities in the wake and close to the lower wall, which is indicative of a stronger vortex providing more entrainment of high-momentum fluid.

Centerline velocity profiles in Figure 11 show that the body-fitted grid solution seems to match the experimental data best for both the stations shown. The IB predictions approach the

body-fitted solution for lower values of k , and interestingly, the mass-conservative IB method is not as quite as accurate as the others. From the comparisons at the $Z = 20$ mm station, it appears that the effects of the primary vortex in energizing the near-wall boundary layer are somewhat under-predicted by all of the IB methods. The shape of the wake deficit is not predicted well by any of the RANS methods at $X = 20$ mm but improves somewhat at $X = 80$ mm. These results

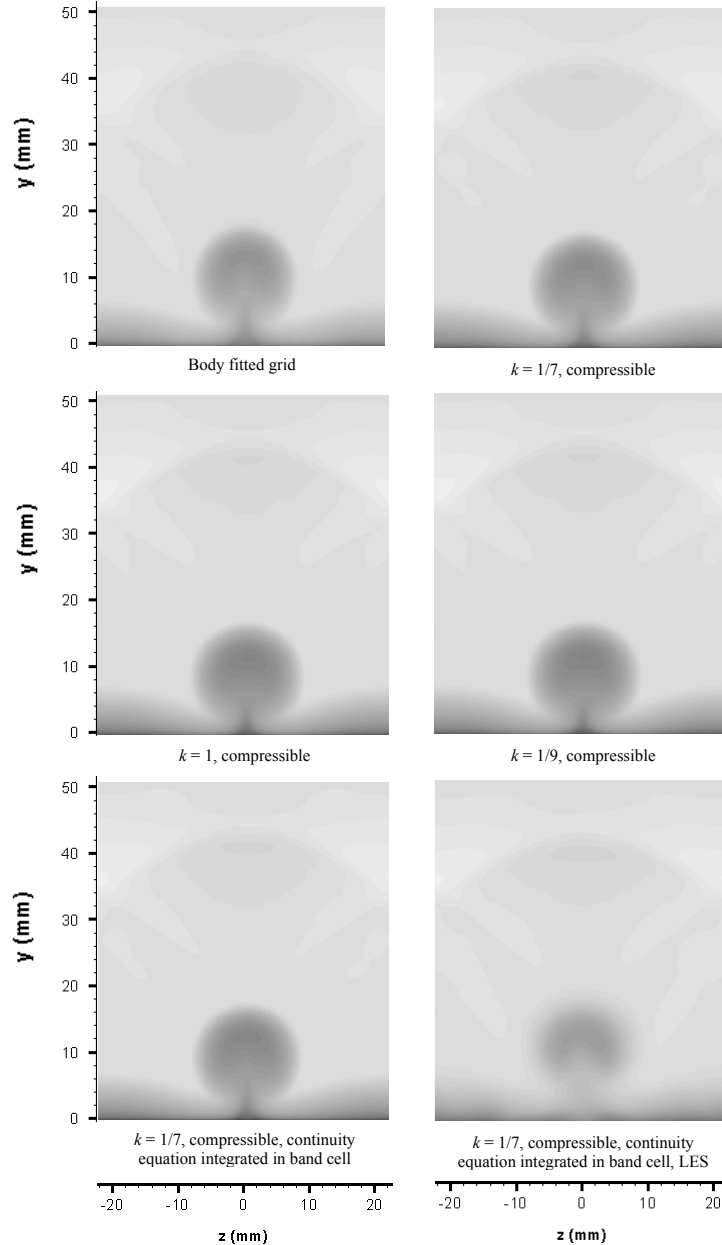


Figure 10: Mach contours at $x = 90$ mm for 6 mm VG in supersonic boundary layer

indicate that the IB rendering of the micro VG provides more of a momentum ‘sink’ than does the body-fitted rendering. Considering that no effort is made to resolve the flow near the surfaces of the micro VG when the IB techniques are used, the level of agreement shown is still encouraging enough for further evaluation.

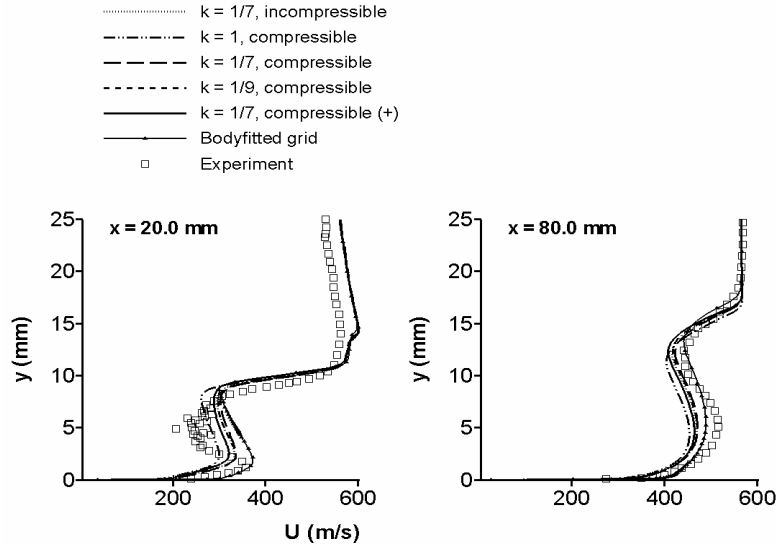


Figure 11: Comparison of centerline axial velocity profiles for different formulations of the IB method (Menter's $k-\omega$), a body fitted grid (Menter's $k-\omega$) and experimental data.

6.2.5. Detailed data comparisons for Mach 2.5 flow over 6mm and 3mm micro VGs

Figure 12 compares velocity profiles obtained using the RANS and LES/RANS models ($k=1/7$, mass-conservative IB) with LDA data collected at several X and Z positions behind the 6mm micro VG. (see Table 1) The energizing effects of the primary vortices are better captured by the LES/RANS model than by the RANS model. This is reflected in the fuller velocity profiles near the wall and close to the VG ($Z = 0$ mm and $Z = 4.5$ mm), which agree quite well with the experimental data. However there is a considerable disagreement in the level of the wake deficit found at the $Z = 4.5$ mm station at $X = 20$ mm and $X = 80$ mm. In the experiment, the wake deficit is almost absent at this Z station, either implying less lateral spreading of the vortices or a device misalignment that shifts the time-mean position of the vortex pair. It should be noted that all measurements were taken on one side of the centerline. In an attempt to determine whether uncertainties in the placement of the laser might play a role, the LES/RANS velocity profiles were also averaged in the Z direction over the experimental positional uncertainty of 2.5 mm (H. Babinsky, personal communication). These profiles show a slight improvement with respect to the experimental data. The good agreement shown at the most downstream station ($X = 140$ mm) for the LES/RANS model lends support to the possibility of a slight misalignment of the micro VG with respect to the incoming flow. The level of agreement found at the more outboard stations ($Z = 9$ mm and $Z = 18$ mm) is generally good, though near-wall discrepancies similar to those observed for the inflow velocity profile persist. The LES/RANS predictions are in better agreement with experimental data at most stations.

Figure 13 presents a similar set of comparisons for Mach 2.5 flow over a 3 mm micro VG. Centerline velocity profiles from the RANS and LES/RANS models do not agree particularly well with the data, in that the latter shows a much smaller wake deficit. The spanwise extent of the vortex pair is predicted to be larger than indicated in the experiment, as the measured wake deficit seems not to exist at any station other than the centerline. Agreement

with experimental data further away from the vortex pair is satisfactory for both models and again, the LES/RANS model provides more accurate predictions at most locations.

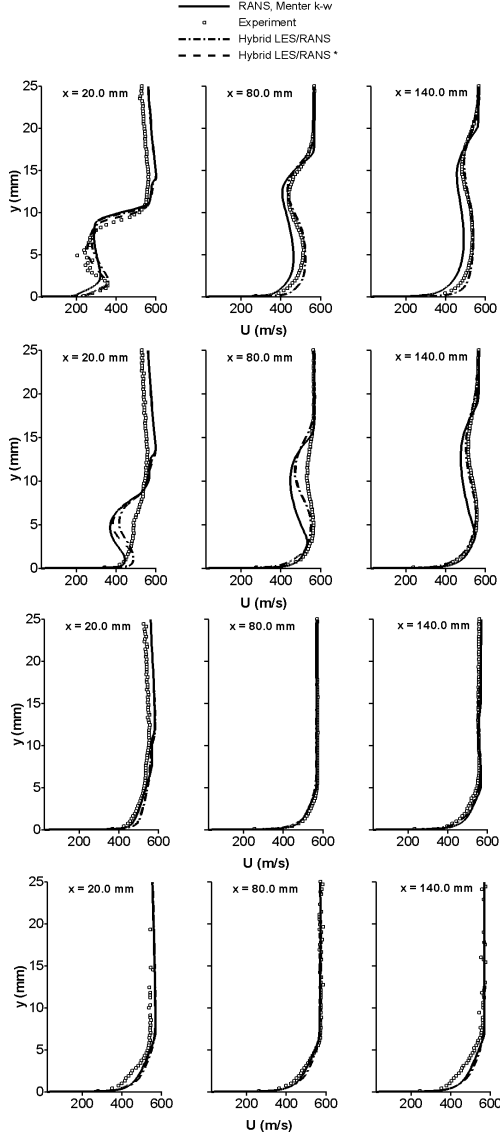


Figure 12: Comparison of axial velocity profiles for flow over 6 mm VG in idealized domain (* = data averaged over a span wise filter of 2.5 mm, centered at the Z location)

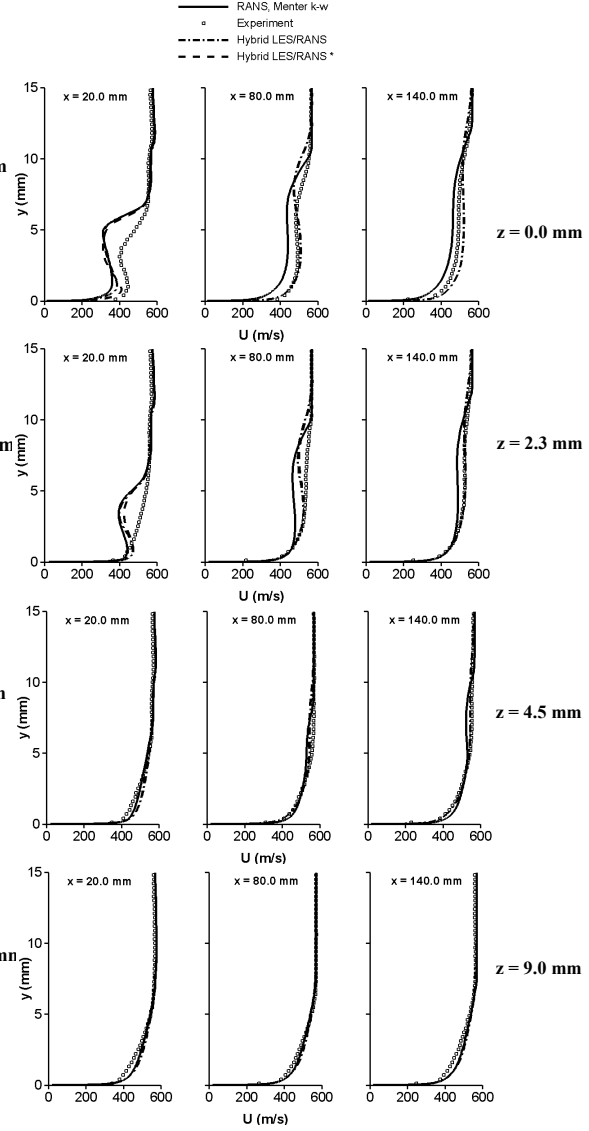


Figure 13: Comparison of axial velocity profiles for flow over 3 mm VG in idealized domain (* = data averaged over a span wise filter of 2.5 mm, centered at the Z location)

6.2.6. Wind-tunnel shock / boundary layer interaction – flow structure

Figures 14 and 15 present near-surface axial velocity contours and streamtraces for the wind-tunnel shock / boundary layer interaction without micro-VG flow control. The vertical white lines in the velocity contour plots indicate the theoretical position of the shock impingement ($X = 159$ mm), while the zero-velocity contour is indicated by a thinner white line.

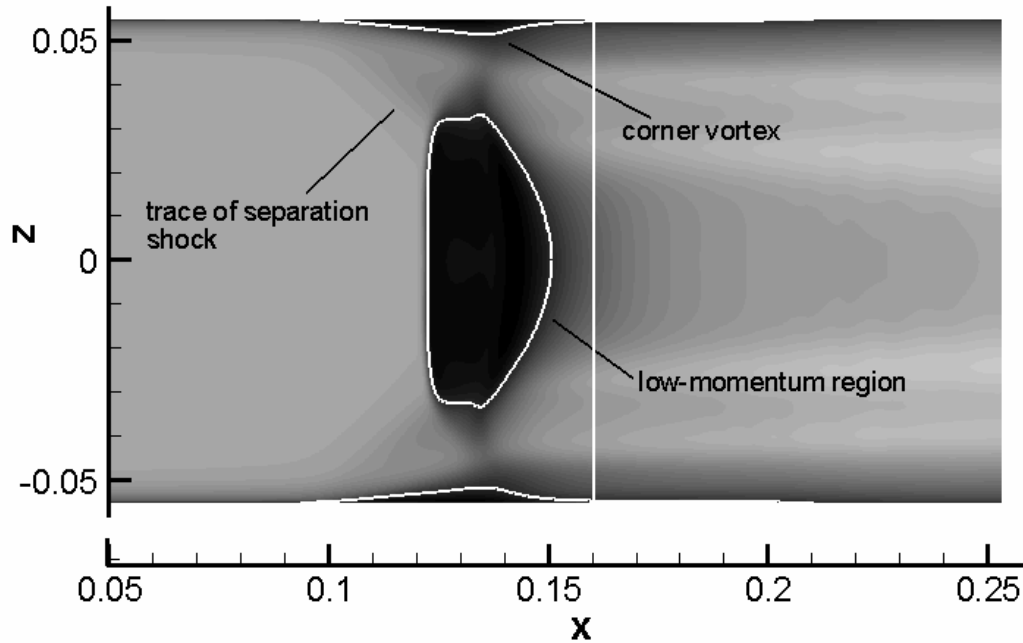


Figure 14: Near surface velocity contours at $Y = 0.0025$ mm (range: -5 m/s (dark) to 35 m/s) for SBLI in wind tunnel (contours reflected about centerline for clarity)

The interaction of the oblique shock with the sidewall boundary layer results in a crossflow separation similar to that observed in sharp fin interactions. The downward motion of the crossflow is arrested by the flat plate, leading to the formation of vortical structures located in the sidewall / flat plate junctures (indicated in dark contours near the upper and lower walls). The displacement effects of these structures induce the formation of a pair of separation shocks and a general movement of the flat-plate boundary layer fluid toward the centerline. Part of the near-wall fluid lifts away from the surface at two foci of separation, located at the points of intersection of the separation shocks with the impinging oblique shock. (Figure 15) This fluid then spirals through the main separation region before exiting near the centerline. The growth of the separation region toward the sidewall is prevented by the crossflow induced by the corner vortices, leading to a non-uniform region of low-momentum fluid that expands more near the centerline. (Figure 14)

6.2.7. Wind-tunnel shock / boundary layer interaction –comparisons with experimental data

Figure 15 compares centerline surface pressure distributions for the SBLIs with and without micro VG control with experimental data. The separation shock strength and the level

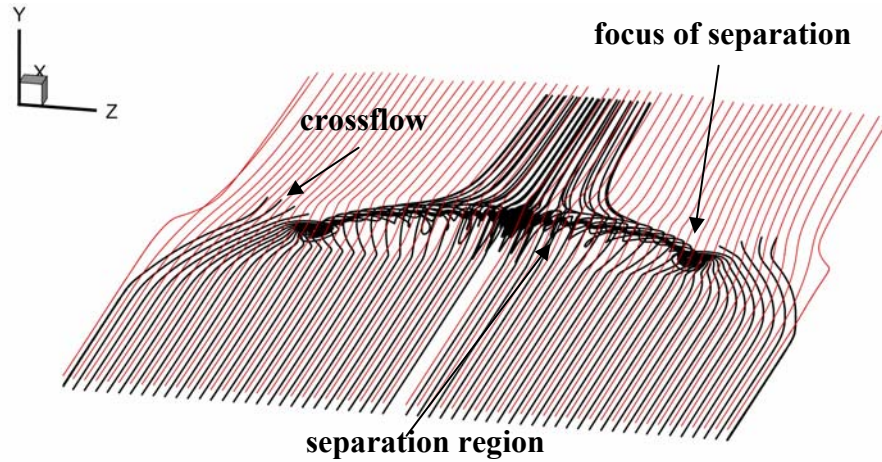


Figure 15: Near-surface streamtraces for SBLI in wind tunnel

of upstream influence of the interaction are predicted well by the Menter SST model for the case without the micro VG array. The predicted pressure distribution shows the start of a plateau behind the initial pressure rise. This feature is commonly observed in stronger SBLIs but is not seen in the experimental distribution. Velocity profiles at different streamwise stations along the centerline are shown in Figure 17. The first station ($X = 20$ mm) is within the region of upstream influence, and the predicted velocity profile shows a small region of reversed flow that is not captured by the LDA data. The comparison at $X = 50$ mm indicates that the calculation does not quite capture the shape of the wake-like velocity profile near the re-attachment position. The recovery of the centerline velocity ($X = 80$ mm and $X = 140$ mm) is predicted very well, except for some deviations in the free-stream velocity similar to those noted earlier.

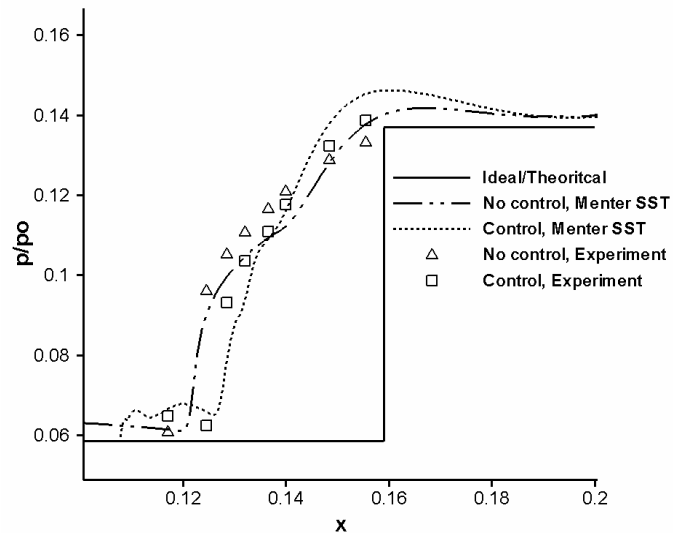


Figure 16: Centerline surface pressure distributions for wind-tunnel cases

6.2.8. Wind-tunnel shock / boundary layer interaction with micro-VG flow control – flow structure

The effects of the micro VG array on the near-surface flow structure are illustrated in Figure 18 (surface velocity contours) and in Figure 19 (near-wall streamtraces). Darker regions

in Figure 18 represent slower-moving fluid, while lighter regions represent faster-moving fluid.

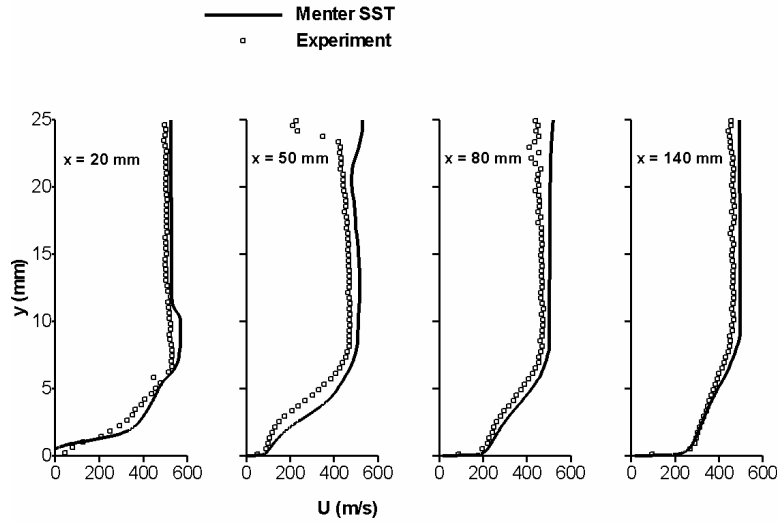


Figure 17: Centerline axial velocity profiles for wind-tunnel case without micro VG array

The major effect of the micro VG array is to induce the formation of longitudinal vortical structures (one pair per micro VG). These structures force higher momentum fluid toward the surface, energizing the inner part of the boundary layer. The traces of the vortical structures are indicated as light bands in Figure 18. The region directly behind the trailing edge of each micro

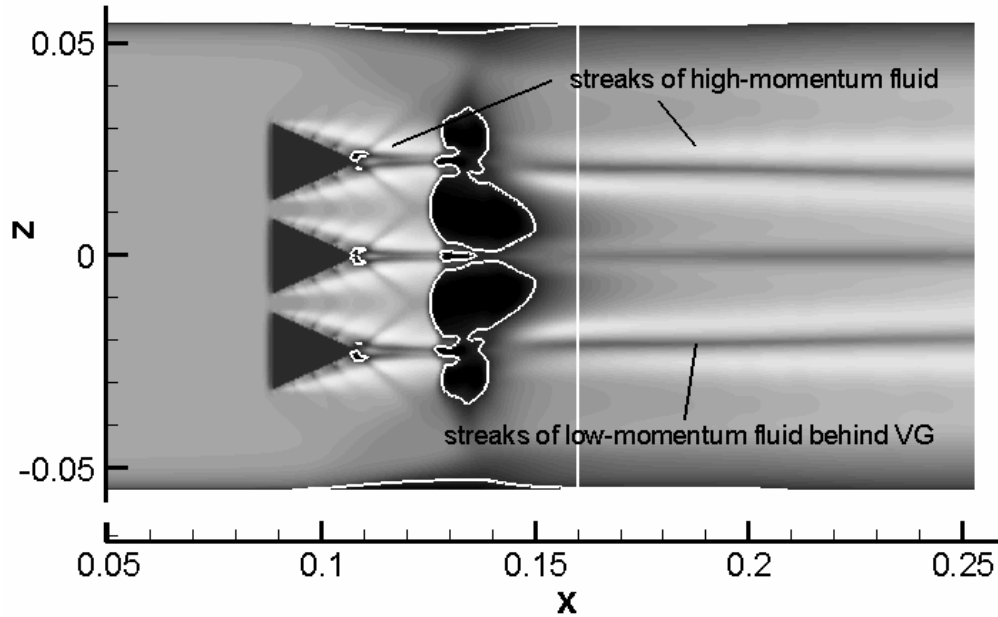


Figure 18: Near-surface velocity contours at $Y = 0.0025$ mm (range: -5 m/s (dark) to 35 m/s) for SBLI with micro VG array in wind tunnel (contours reflected about the centerline for clarity)

VG is influenced by another pair of counter-rotating vortices that act to move fluid away from the surface, resulting in low-momentum streaks that also persist downstream of the interaction

region. Comparing Figures 18 and 14, it is clear that the vortices induced by the micro VG array deform the large separation region but do not significantly reduce its size. The level of upstream influence is reduced in regions where the counter-rotating vortices energize the near-wall boundary layer but increases in the regions between the micro VGs. The strengths of the vortices generated by the centerline micro VG appear to be reduced relative to the others, as a consequence of their interaction with the large separation region. The amount of reversed flow again approximately coincides with the outer boundary of the dark region, except for the portions directly influenced by the counter-rotating vortex pairs.

The black streamtraces in Figure 19 show that part of the near-wall fluid originating between the outer VGs and the (corresponding) sidewalls is entrained into the vortex pairs generated from these devices. Another portion moves toward the centerline and lifts from the surface at two foci of separation, where it is entrained into the vortices generated by the centerline microVG. Some of the near-wall fluid originating between the micro VGs is also

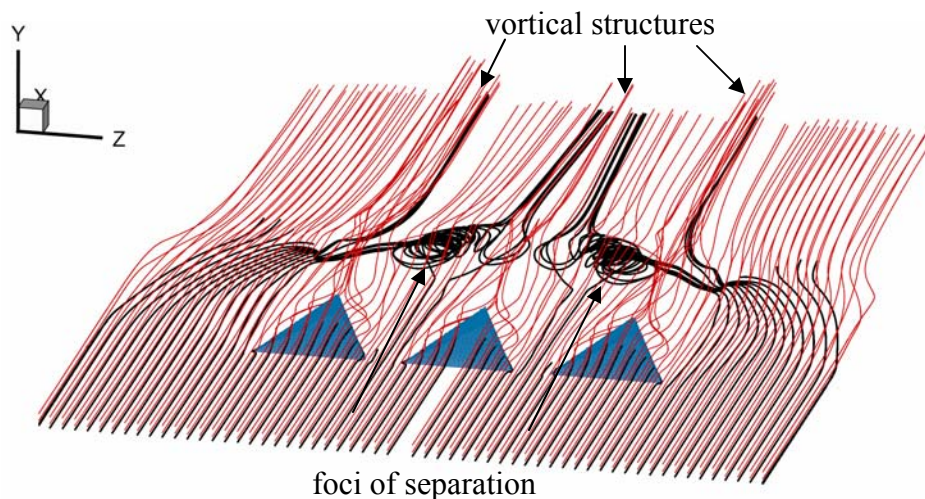


Figure 19: Near-surface streamtraces for SBLI with micro VG array in wind tunnel

entrained into the low-momentum region and departs from the surface at these foci. Fluid originating further away from the surface (red streamtraces) moves over and around the micro VGs but does not enter the low-momentum region. Some of this fluid eventually migrates into the vortical structures.

6.2.9. Wind-tunnel shock / boundary layer interaction with micro-VG flow control – comparisons with experimental data

Pressure distributions shown in Figure 16 indicate that the effect of the micro VG array, at least at the centerline, is to reduce slightly the upstream extent of the separation region and to sharpen the pressure rise. An overshoot in pressure is observed near the re-attachment location for both the calculated and measured distributions but is more pronounced in the former.

Axial velocity predictions at several streamwise and spanwise stations are shown in Figure 20. At the $X = 20$ mm and $X = 50$ mm stations along the centerline ($Z = 0$), the calculated velocity profiles show a pronounced low-momentum region that is associated with the

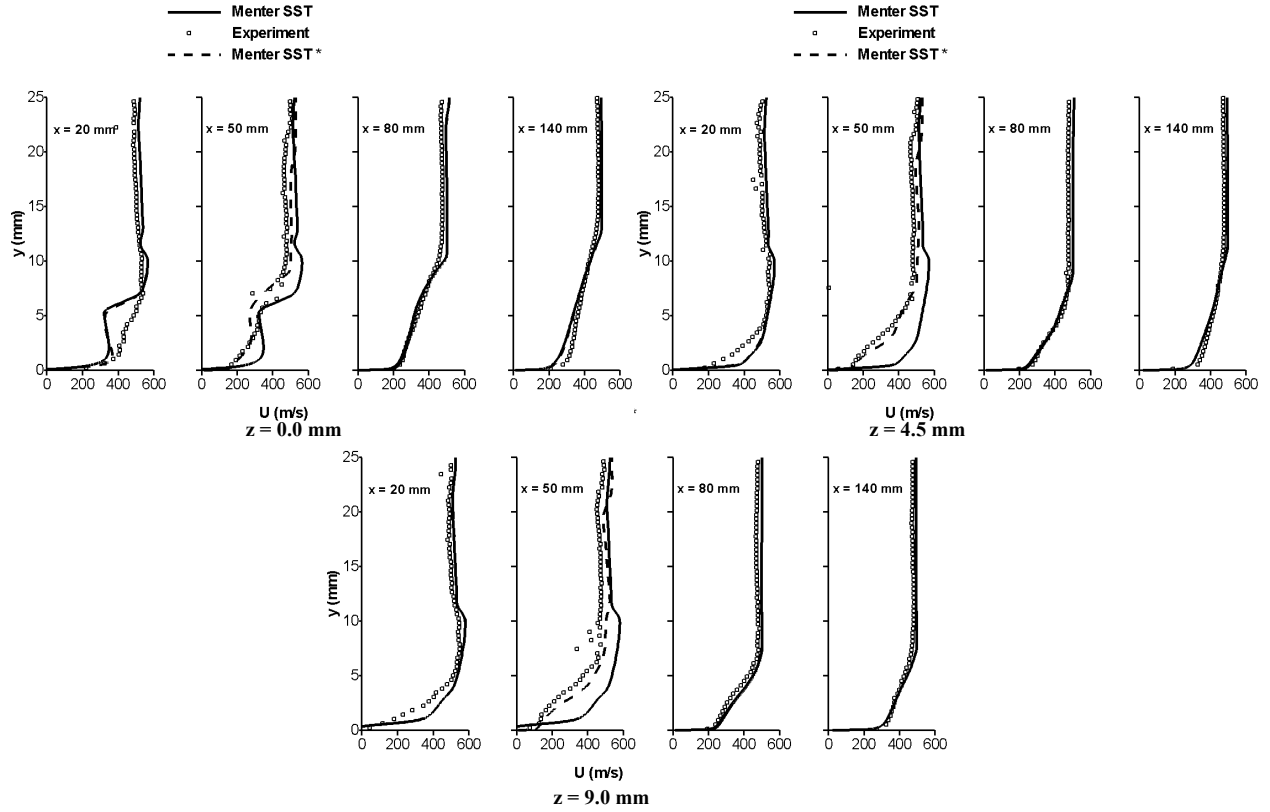


Figure 20: Axial velocity profiles for wind-tunnel case with micro VG array (* indicates data averaged over a spanwise filter of 2.5 mm, centered at the Z location)

vortex pairs. This feature is not prominent in the experimental profiles, similar to the single micro-VG results. The centerline profiles further downstream are in better agreement with the experimental data. The $Z = 4.5$ mm, $X = 50$ mm position is near the location where the centerline vortex divides the main separation region into a smaller one located near the centerline and a larger one located further away. The topology of the flow in this region changes abruptly, and improved predictions are obtained by averaging the computed velocity profiles over the experimental positional uncertainty of 2.5 mm. The same is true for the data station at $Z = 9.0$ mm, $X = 50$ mm. Agreement with the experimental data at $X = 80$ mm and $X = 140$ mm can be considered as excellent.

6.2.10. Idealized shock / boundary layer interaction

It is clear from the preceding discussion that three-dimensional effects significantly influence the flow features in the Cambridge wind tunnel experiments, and the evaluation of the expected benefits of the micro VG array is made more complicated as a result. To assess the behavior of the micro VG concept in an idealized setting and to compare the predictions obtained from the RANS and LES/RANS models, we consider an oblique shock interaction with and without micro VG control using the periodic domain discussed earlier. Here, the viscous side and top walls of the wind tunnel are neglected, and the incoming boundary layer is developed as a flat-plate solution at the test-section conditions. Periodic boundary conditions are imposed in

the spanwise (Z) direction. The shock generator position is adjusted so that the oblique shock impinges at $X \approx 146$ mm as discussed earlier. The resolution of the interaction region in the

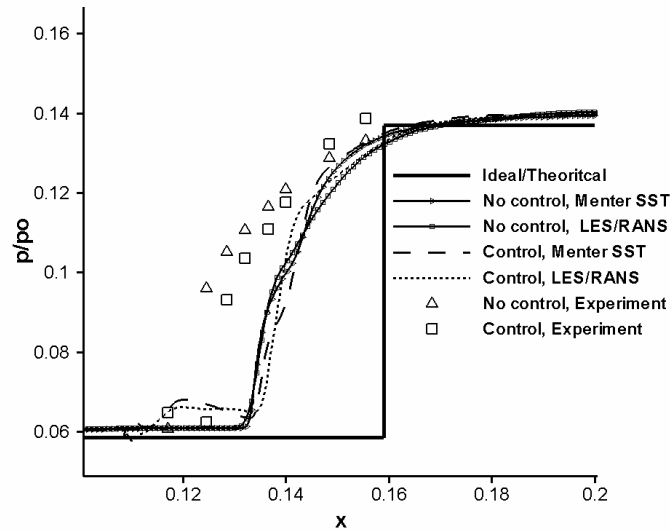


Figure 21: Centerline surface pressure distributions for idealized cases

streamwise and spanwise directions is the same as in the wind-tunnel calculations. Both RANS and hybrid LES/RANS calculations are performed for this configuration.

In the absence of the sidewalls and the VG array, the oblique shock interaction is nominally two-dimensional. Centerline pressure distributions shown in Figure 21 imply that the upstream extent of the low-momentum region is much less in the idealized interaction than in the experiment. As such, one cannot expect quantitative agreement with the experimental velocity profiles in the interaction region, and no such comparisons are presented. Details of the idealized interaction are shown in the near-surface velocity contours of Figures 22 and 23. To

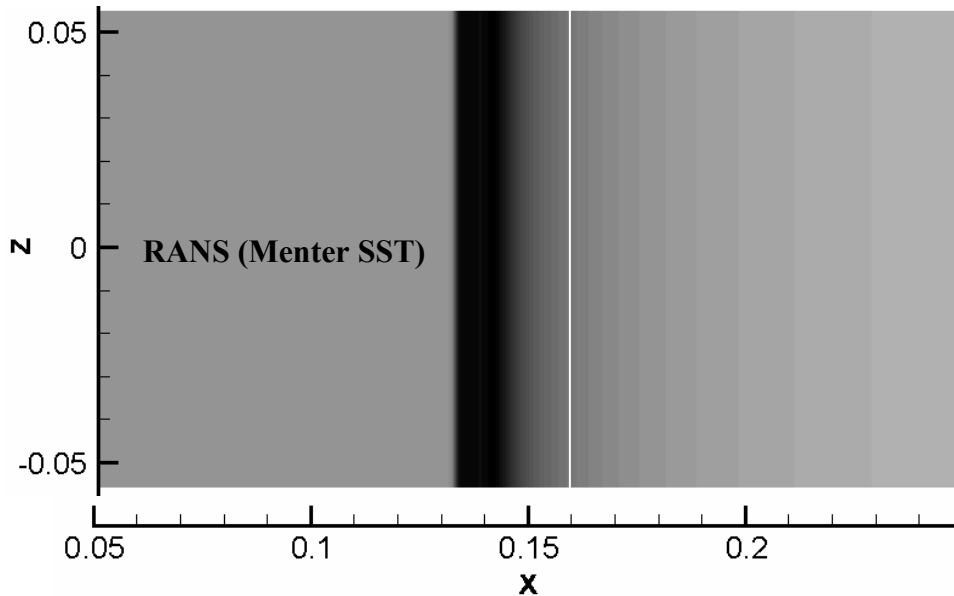


Figure 22: Surface velocity contours (range: -5 m/s (dark) to 35 m/s) for idealized SBLI (Menter SST RANS model)

facilitate a direct visual comparison with the wind-tunnel interaction, the Z scale is expanded to approximate the actual width of the wind tunnel, and both the velocity contour levels and the X scale are the same as in Figure 14. The extent of the low-momentum region is captured similarly by both modeling approaches, but the LES/RANS model predicts a smaller region of reversed flow with smaller velocity components (in magnitude). The near-surface boundary layer recovers more rapidly in the LES/RANS calculation, reaching span-averaged values of ~ 27 m/s as compared with ~ 20 m/s for the RANS solution at the exit plane.

One obvious feature is that traces of organized three-dimensionality are indicated in the time-averaged LES/RANS contours.(Figure 23) These result from the combination of several factors, the most noteworthy of which is the tendency of the recycling / rescaling method to ‘fix’ the spanwise positions of longitudinal vortices (in the time average) that are generated within the upstream boundary layer. Due to the action of shearing stresses, these structures become more elongated near the wall, and because of the absence of realistic turbulence in the logarithmic

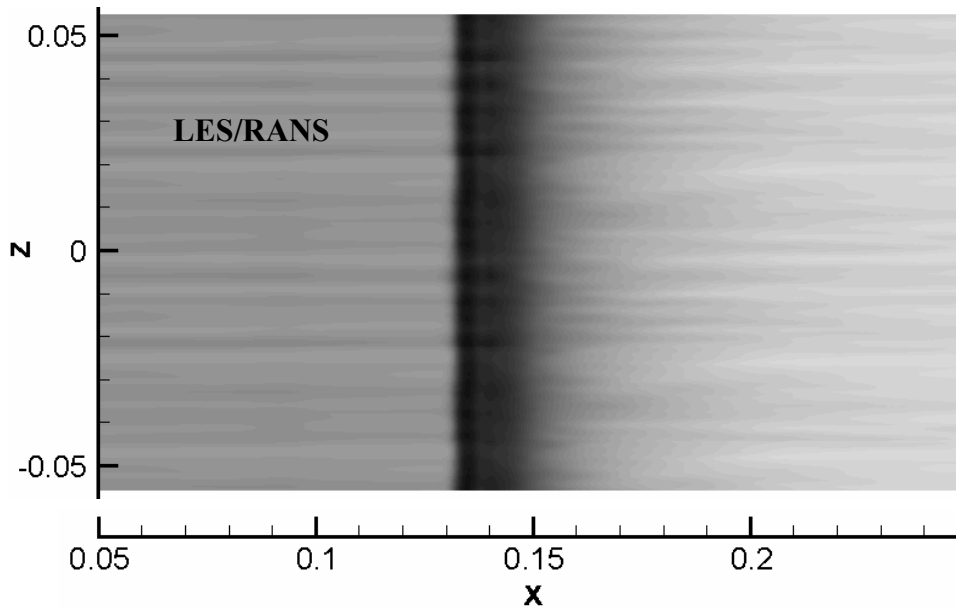


Figure 23: Surface velocity contours (range: -5 m/s (dark) to 35 m/s) for idealized SBLI (LES/RANS model)

region and below, the ‘footprints’ of the outer-layer structures are imposed upon the near-surface velocity field. The persistence of the structures for this particular calculation is also influenced by the relatively coarse mesh (ranging from about 9 cells per boundary layer thickness in the wall-transverse (X and Z) directions at the inflow to 15 cells per boundary layer thickness near the exit).

Because of the dominant effect of the sidewall separation in the wind tunnel, it is difficult to draw any direct comparisons between the idealized and wind-tunnel cases. It can be noted, however, that the area occupied by low-momentum fluid is similar in size for the two cases (Figures 22 and 14), indicating that the effect of the crossflow in the wind tunnel is to restrict the growth of the separation region in the spanwise direction while enhancing its growth in the streamwise direction.

6.2.11. Idealized shock / boundary layer interaction with micro-VG flow control

Center plane Mach number contours corresponding to the idealized oblique shock / boundary layer interaction with 3 mm micro VG control are shown in Figure 24 for the RANS (steady-state contours) and LES/RANS (instantaneous contours) models. The generation of an additional oblique shock wave by the micro VG is of note, as is the effect of the incident oblique shock in turning the vortex pair generated by the micro VG more toward the surface. The

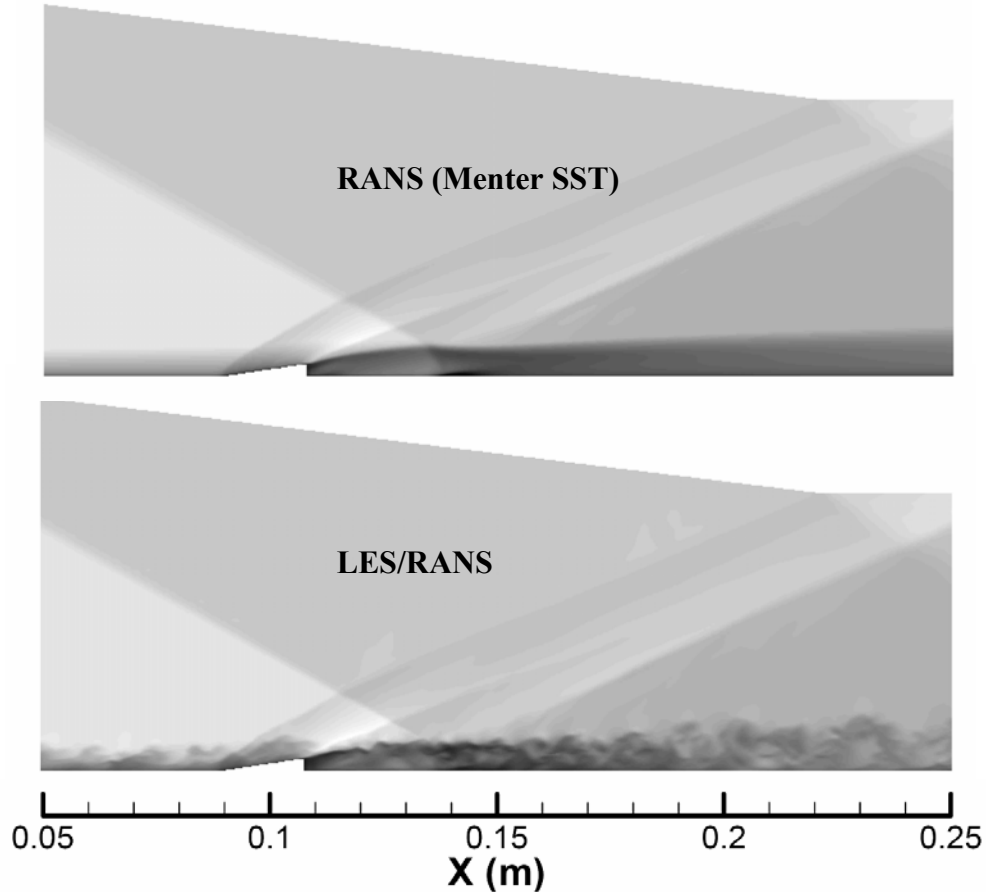


Figure 24: Centerplane Mach number contours (idealized interaction with micro VG array)

instantaneous snapshot indicates a more energetic eddy structure downstream of the shock impingement position. This may result from turbulence amplification through baroclinic torque, bulk compression, shock motion, and other mechanisms.

Surface velocity contours are shown in Figures 25 and 26 for the RANS and LES/RANS models, respectively. The vortices predicted by the LES/RANS model transfer more high-momentum fluid to the surface in the region directly behind the micro VGs, this being indicated by lighter contours. As a consequence, the overall separation extent is reduced for the LES/RANS calculation, relative to the RANS calculation. This is particularly evident for the low-momentum region directly behind the micro VG apex. Comparing Figures 25 and 26 with Figures 22 and 23, it is seen that the dominant effect of the micro VG array is to break up the nominally two-dimensional separation region into smaller pockets. The micro VG array appears more effective in actually eliminating regions of low-momentum fluid in this idealized interaction than in the wind-tunnel case. The vortices generated by the micro VG array appear to broaden downstream of the interaction for the LES/RANS model. This could be a consequence

of the turbulence amplification mechanisms noted earlier, and the effect is to homogenize the surface fluid in the spanwise direction. The average surface velocity at the exit plane is about

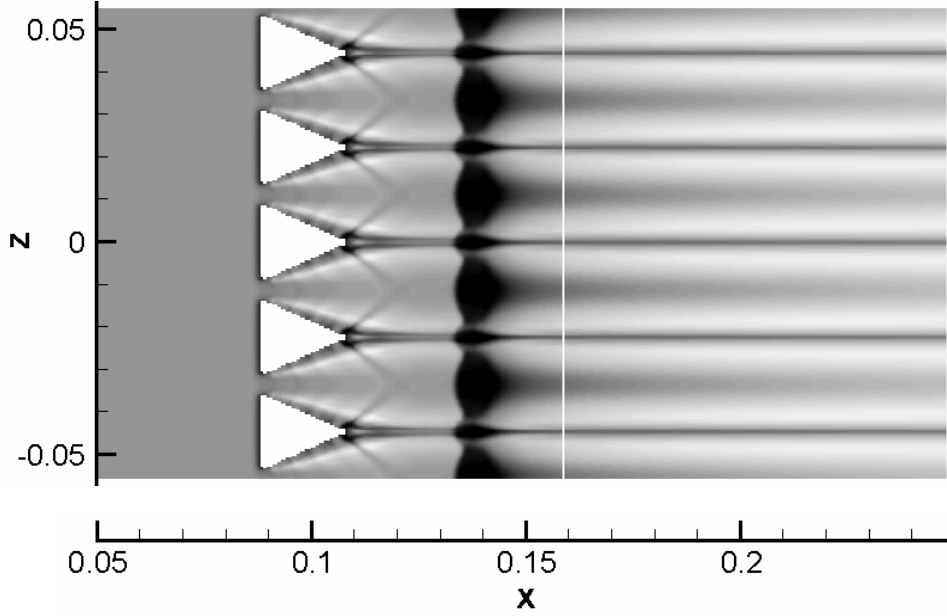


Figure 25: Surface velocity contours (range: -5 m/s (dark) to 35 m/s) for idealized SBLI with micro VG control (Menter SST RANS model)

30 m/s for the LES/RANS model and about 28 m/s for the RANS model, but the spanwise distribution of velocity for the LES/RANS model is much more uniform. The region of low-

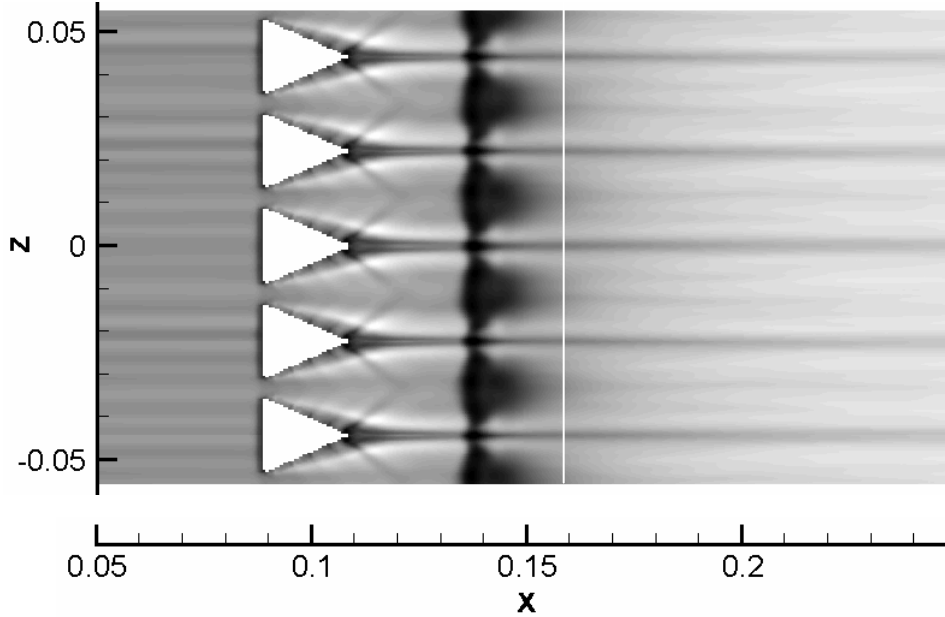


Figure 26: Surface velocity contours (range: -5 m/s (dark) to 35 m/s) for idealized SBLI with micro VG control (LES/RANS model)

momentum fluid directly behind the micro VG apex is smaller in the LES/RANS calculation, and the minimum velocity in this region is higher (~ 25 m/s versus ~ 12 m/s). The fact that the vortices generated by the micro VGs continue to energize the boundary layer well downstream of

the main interaction is noteworthy, as it indicates the potential of controlling weaker shock / boundary layer interactions generated as a part of a shock train, even if the main separation region is not totally eliminated.

6.3. Bleed Control of Shock / Boundary Layer Interactions

The second set of calculations presented in this work utilizes the LES/RANS/IB methodology to simulate the effects of bleed-hole arrays in controlling shock-induced flow separation. Here, an entire array of bleed holes (up to 68), along with portions of the supporting flat plate, are rendered as immersed objects. The following sections are excerpted from papers P-2 and P-6 in the publication list (see Section 9).

6.3.1. Experiment details

Experiments involving the effects of boundary layer bleed on shock interaction control were performed at NASA Glenn Research Center by Willis, et al. [26]. The experiments were performed at a nominal Mach number of 2.46, a stagnation temperature of 292 K, and a stagnation pressure of 172.4 kPa. In the configuration, an eight-degree wedge was placed so that the generated oblique shock impinged in the middle of a 9.52 cm bleed region embedded within the wind-tunnel lower surface. This region consisted of a regular array of one hundred circular holes with diameter $D = 0.635$ cm and length $L = 0.635$ cm, oriented 90 degrees with respect to the plate surface. The bleed flow exited into a plenum chamber, and the rate of mass flow out of the system was controlled by a regulator and driven by a vacuum generated by a 450 psi air ejector system. Both the plenum pressure and overall bleed mass flow were recorded in the experiments. Data collected in these experiments included Pitot pressure surveys at different streamwise locations, wall static pressure distributions, and Pitot pressure surveys taken in the bleed-region exit plane, all as a function of the bleed mass flow rate. In the experiments, the bleed mass flow rate is expressed as a discharge coefficient Q , representing the ratio of the actual bleed rate to the ideal value obtained under choked-flow conditions. Data was obtained for three values of Q – 0.00, 0.0342, and 0.0685 – as well as for a baseline case where the bleed plate was replaced by a solid surface. This case differs from the $Q = 0.00$ case, as the latter allows bleed into, and injection out of the plenum. Except for the zero bleed case ($Q = 0.0$), all other cases are considered in this study.

In addition to the Willis, et al. shock / boundary layer experiment [26], calculations were also performed for an experiment involving Mach 2.45 boundary-layer flow over a bleed plate [34]. This experiment focused on quantifying the discharge coefficient as a function of hole size, hole angle, plenum pressure, and free-stream conditions. The hole shape is the same as in [26] but the spacing of the holes within the array is different.

6.3.2. Computational domain and calculation details

The computational domain for the Willis, et al. [26] flat-plate boundary-layer simulations extends from $X = -5.08$ cm to $X = 17.78$ cm in the streamwise direction, from $Y = 0$ cm to $Y = 7.62$ cm in the wall-normal direction, and from $Z = -1.905$ cm to $Z = 1.905$ cm in the spanwise direction. The bleed plenum for this case ranges from $X = -1.905$ cm to $X = 9.525$ cm and from $Y = -7.62$ cm to $Y = -0.635$ cm, and the bleed-hole region extends from $X = 0$ cm to $X = 7.62$ cm and from $Y = -0.635$ cm to $Y = 0$ cm. To provide better resolution near the bleed ports, the

meshes covering the bleed region are refined by a factor of two in the Z direction. A patched-mesh boundary condition [35] is used to facilitate the coarse-to-fine and fine-to-coarse information transfers in this region. The X-Z resolution is sufficient to cover each circular bleed hole with a 10×10 square mesh. The total number of cells is 3.24 M, with 2.268 M located above the flat plate, 0.432 M within the bleed-hole region, and 0.540 M in the plenum. The bleed plate itself is generated as a combination of surfaces: two flat plates with cut-out holes for the top and bottom portions and 18 hollow cylinders ($L = 0.635$ cm, $D = 0.635$ cm) for the hole walls. A relatively fine IB surface mesh, containing 1.32 M points, was used to ensure an accurate distance-function evaluation. Figure 27 shows the immersed-surface rendition of one circular cylinder (hole wall) and the surrounding mesh.

The computational domain for the Willis, et al. [26] shock / boundary-layer interaction simulations extends from $X = -31.81$ cm to $X = 25.0$ cm in the streamwise direction, from $Y = 0.0$ cm to $Y = 21.5$ cm in the wall-normal direction at the inflow plane, and from $Z = -5.08$ cm to $Z = 5.08$ cm in the spanwise direction. The upper boundary is aligned with the position of the 8-degree shock generator. The nominal mesh spacing in the X and Z directions is 0.13 cm, decreasing to half of this value in the portions of the mesh covering the bleed region. The meshes covering the bleed region range from $X = -2.23$ cm to $X = 13.01$ cm and from $Y = -2.5$ cm to $Y = 0.0$ cm. The plenum chamber extends from $X = -14.5$ cm to $X = 26$ cm at the upper end (end of bleed region, $Y = -2.5$ cm) and from $X = -3.82$ cm to $X = 15.82$ cm at the exit ($Y = -24.64$ cm). The cross-section of the plenum is rectangular till about $Y = -9.88$ cm and then tapered to the dimensions at the exit using cubic fits. The bleed ports for this case are the same size as in the flat-plate study and the X-Z resolution is sufficient to cover each port with 10×10 square cells. The total number of mesh cells is 21.504 M, with 12.544 M located above the flat plate, 1.792 M located in the portion of the domain covering the bleed holes, another 1.792 M in the region between the bleed holes and the plenum and 5.376 M located in the plenum. The bleed-plate surface mesh contains 4.367 M points and is comprised of two flat sections with cut-out holes and 68 individual hollow cylinders.

No-slip, adiabatic-wall boundary conditions are imposed on all solid surfaces (excepting shock-generator and plenum walls where a slip wall condition is imposed) for both cases. A linear power-law is used to define the near-surface velocity interpolation for the flat-plate portions of the immersed bleed-plate object, as the mesh spacing near the wall is sufficient to resolve the viscous sublayer. The power-law for the portions representing the hole walls was varied as part of the flat-plate boundary-layer study, but in general, a fractional power law ($1/7$ or

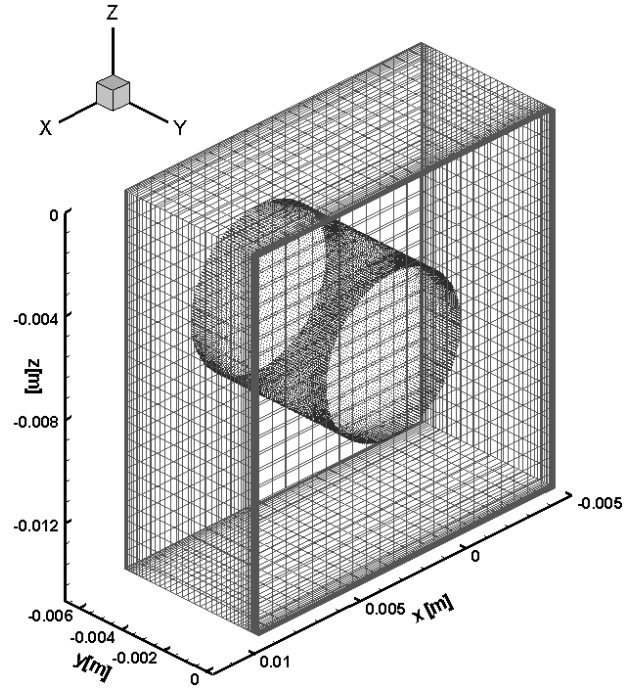


Figure 27: Mesh around the IB rendition of a circular bleed hole

1/9) is employed, as the mesh resolution near the hole surfaces does not extend into the viscous sublayer. A subsonic outflow condition which imposes the experimental mass flow rate (using a relaxation technique) is used at the plenum exit. Pressure and temperature are extrapolated and density is calculated based on equation of state. The normal velocity is then fixed based on the value of mass flux imposed and the density. The tangential velocity components are also zeroed out. Periodic boundary conditions are imposed in the spanwise directions. It should be noted that the experiments of Willis, et al. [26] used aerodynamic fences to isolate the interaction region from the corner flows developing in the wind tunnel. The spanwise extent of the computational domain does not extend to the positions of the fences (± 7.94 cm), and as such, the calculations represent an idealized shock / boundary-layer interaction free from effects of mean three-dimensionality. For the flat-plate boundary-layer simulations, flow properties are extrapolated from the interior on the upper boundary and the downstream boundary. For the shock / boundary-layer interactions, slip-wall conditions are applied along the upper boundary, and properties are extrapolated from the interior at the downstream boundary.

In all cases, a flat-plate simulation at the test-section conditions was performed to determine the place at which the predicted boundary layer properties most closely matched the experimental data. Flow properties at the inflow plane of the computational domain were then extracted from the flat plate solution at a location consistent with the position of the inflow plane relative to the measurement location. Convergence of the RANS calculations was ascertained using three measures: relative decrease in residual norm, constancy of surface quantities, and

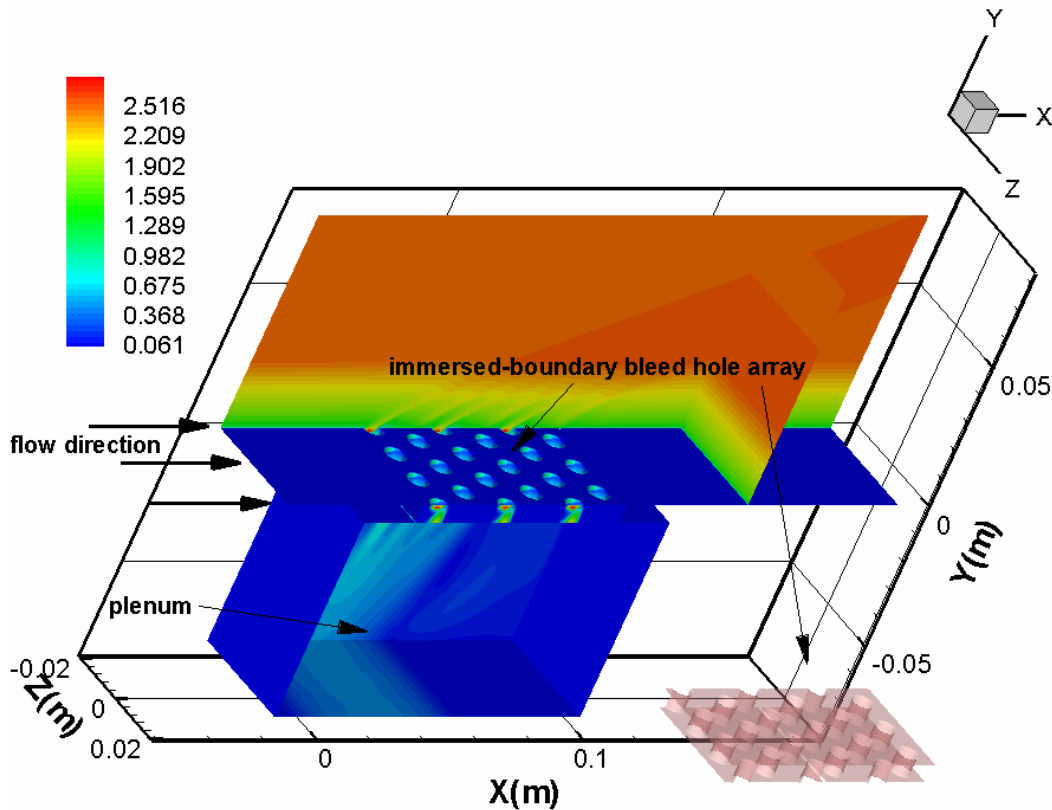


Figure 28: 3-D view of flow over a perforated plate with active suction (Mach number contours shown)

constancy of the global mass flow rate and bleed mass flow rates. The bleed mass flow rates were evaluated at the bleed-hole entrance and exit planes as well as the plenum exit plane. The LES/RANS calculations were initiated by super-imposing scaled boundary-layer fluctuations from an earlier calculation onto part of a converged RANS solution. After several flow-through times to eliminate initial transients, time-averaged statistics for the LES/RANS calculations were collected over a minimum of seven flow-through times, based on the domain length and free-stream velocity.

6.3.3. Flat-plate boundary layer simulations with bleed

Simulations of Mach 2.5 flow over a perforated plate were performed to ascertain the ability of the methodology to predict the discharge coefficient as a function of plenum pressure. The Menter BSL RANS model was used for these calculations. Mach number contours in Figure 28 show the characteristic pattern of flow entrainment into the bleed holes. The immersed-boundary object that represents the bleed plate is also shown in Figure 28. A large pocket of separated flow is formed at the upstream edge of each hole. The near-wall fluid accelerates to supersonic velocities within the bleed port and is forced to change direction, moving down into the plenum. The separation region forms an effective converging / diverging nozzle that first slows the supersonic flow down, then expands it to higher supersonic velocities before entering the plenum. Figure 29 plots the

discharge coefficient (actual mass flow rate divided by ideal (isentropic) mass flow rate at sonic conditions) versus the ratio of the plenum pressure to the upstream stagnation pressure. The predictions are seen to be in reasonable agreement with the experimental data. The predicted mass flow rate is a strong function of the power used to define the band-cell velocity field near the hole surfaces. Using a value of $k = 1$ (consistent with a linear near-wall velocity field and laminar flow) leads to too much flow separation within the bleed holes and to a reduction in the discharge coefficient. Values more consistent with a turbulent profile ($k = 1/7$ or $k=1/9$) promote more flow attachment and provide discharge coefficients more in accord with the experimental data. The predicted discharge coefficients at lower plenum pressures are somewhat smaller than indicated in the experiment. The effect of reducing the X-Z mesh resolution over each hole from 10×10 cells / hole to 5×5 cells / hole is also shown for the lowest plenum pressure. A reduction in predicted mass flow rate of about 17%, relative to the baseline 10×10 resolution, is observed.

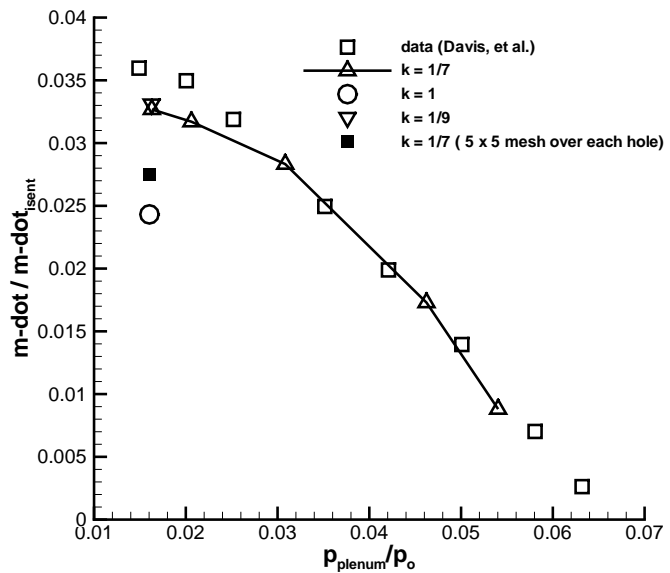


Figure 29: Flow coefficient versus plenum pressure

6.3.4. Oblique-shock / turbulent boundary layer interaction without bleed

A snapshot of temperature contours along the X-Y centerplane is shown in Figure 30 for the baseline shock / boundary layer interaction without bleed. The results indicate a general thinning of the boundary layer downstream of the shock reflection as well as local ‘hot spots’

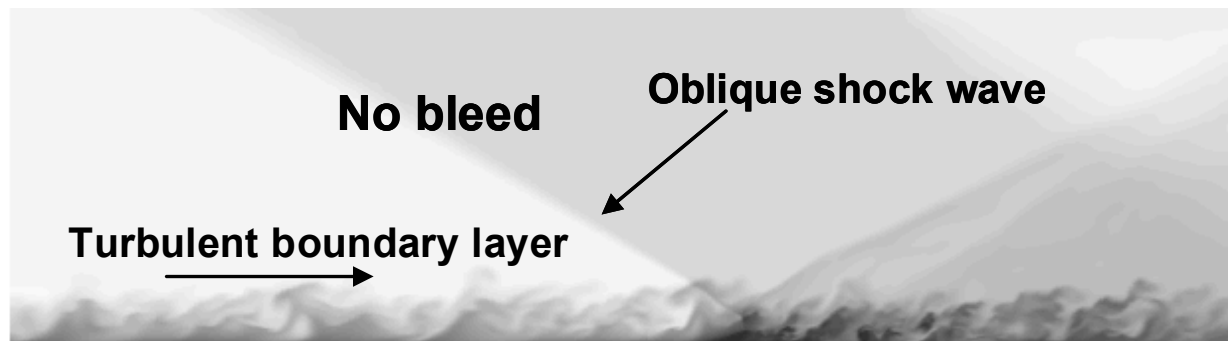


Figure 30: Snapshot of centerplane temperature contours for oblique shock interaction without bleed

(darker contours) caused by turbulent separation and re-attachment as well as by shock interaction. The shock wave is strong enough to induce mild separation of the turbulent boundary layer, as indicated in Figure 31, a plot of centerline wall pressure. The better agreement with experimental data is provided by the Menter SST RANS model, which correctly predicts the degree of upstream influence shown in the experiment. The LES/RANS model and Menter BSL RANS model (not shown) tend to under-predict the size of the separation region.

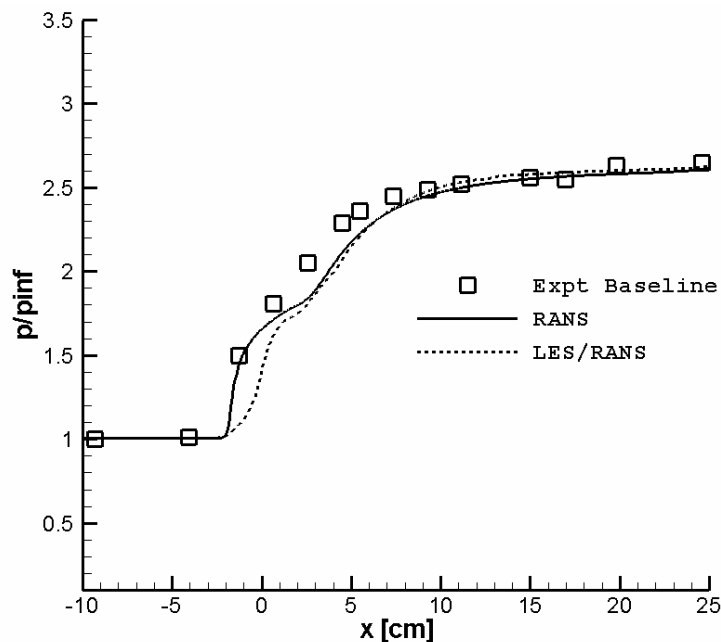


Figure 31: Wall pressure distributions: shock / boundary layer interaction without bleed

Centerline Pitot-pressure distributions throughout the interaction region are shown in Figure 32 for the LES/RANS and Menter SST models. The first trace of the incident oblique shock is captured at station 4, with the sharp pressure change at ~ 4 cm from the wall. Stations 5-8 ($x = 3.8, 29.2, 54.5, 80.0$ mm) form the core of the interaction of the oblique shock with the boundary layer. This is expected as these stations are within the bleed plate and the inviscid oblique shock impinges ideally at the center of the bleed region. The experimental data shows the onset of separation in profile 5. Good agreement is generally observed, with some discrepancies in the wake-like profile noted in the LES/RANS predictions at the $X = 3.8$ mm and $X = 29.2$ mm stations. These are related to the under-prediction of axial separation noted earlier. In the recovery region, the LES/RANS and RANS predictions generally bracket the experimental data, with the former slightly over-predicting the rate of recovery of the boundary layer.

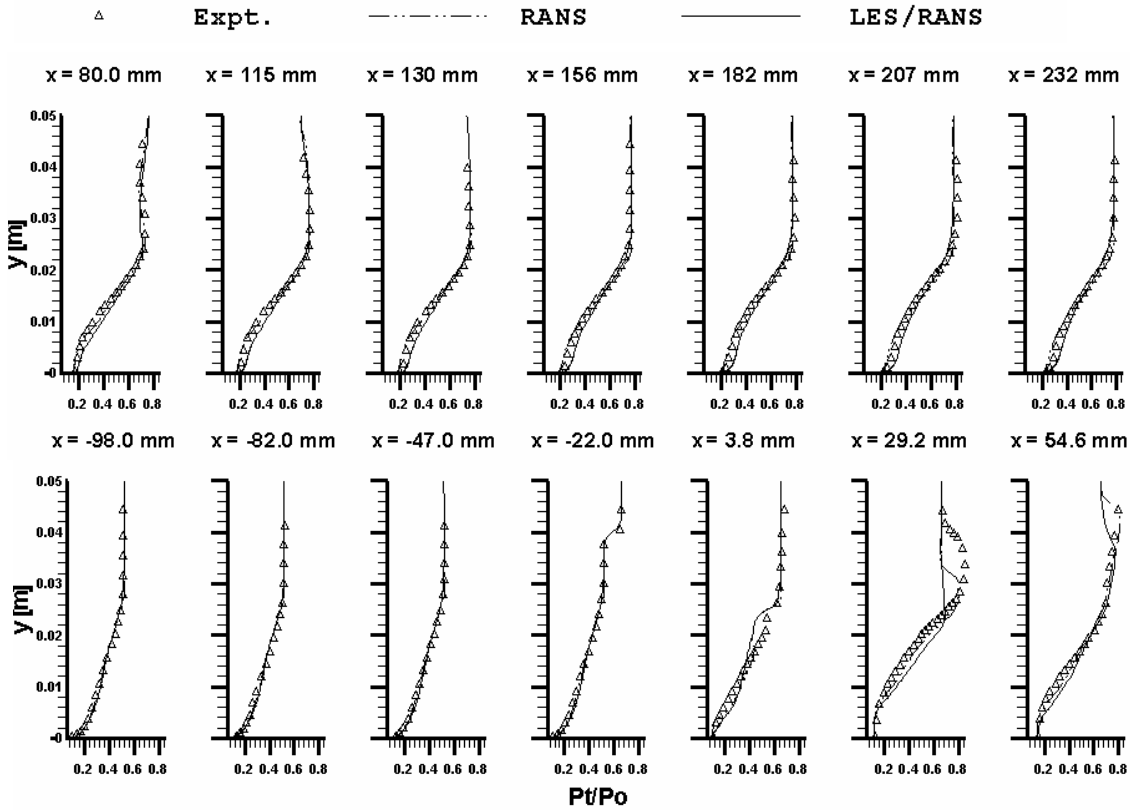


Figure 32: Pitot pressure distributions: shock / boundary layer interaction without bleed

6.3.5. Oblique-shock / turbulent boundary layer interaction with bleed

The cases detailed in this section involve suction through a 68-hole perforated plate, shown in Figure 33 as the zero iso-surface of the signed distance function. Two different bleed rates, referred to henceforth as ‘full bleed’ (maximum bleed) and ‘half bleed’, which is basically half of the maximum bleed, were simulated. Both RANS and LES/RANS simulations were performed for the full bleed case while only the LES/RANS model was used for the half bleed

simulation. Both the simulations were initialized with plenum pressures which correspond to those in the experiment for the respective bleed rates (5534 Pa for full bleed and 17413 Pa for half bleed). In the half-bleed case, the bleed mass flow rates are much more unsteady due to periodic blowing and suction through the holes located upstream of the shock impingement position.

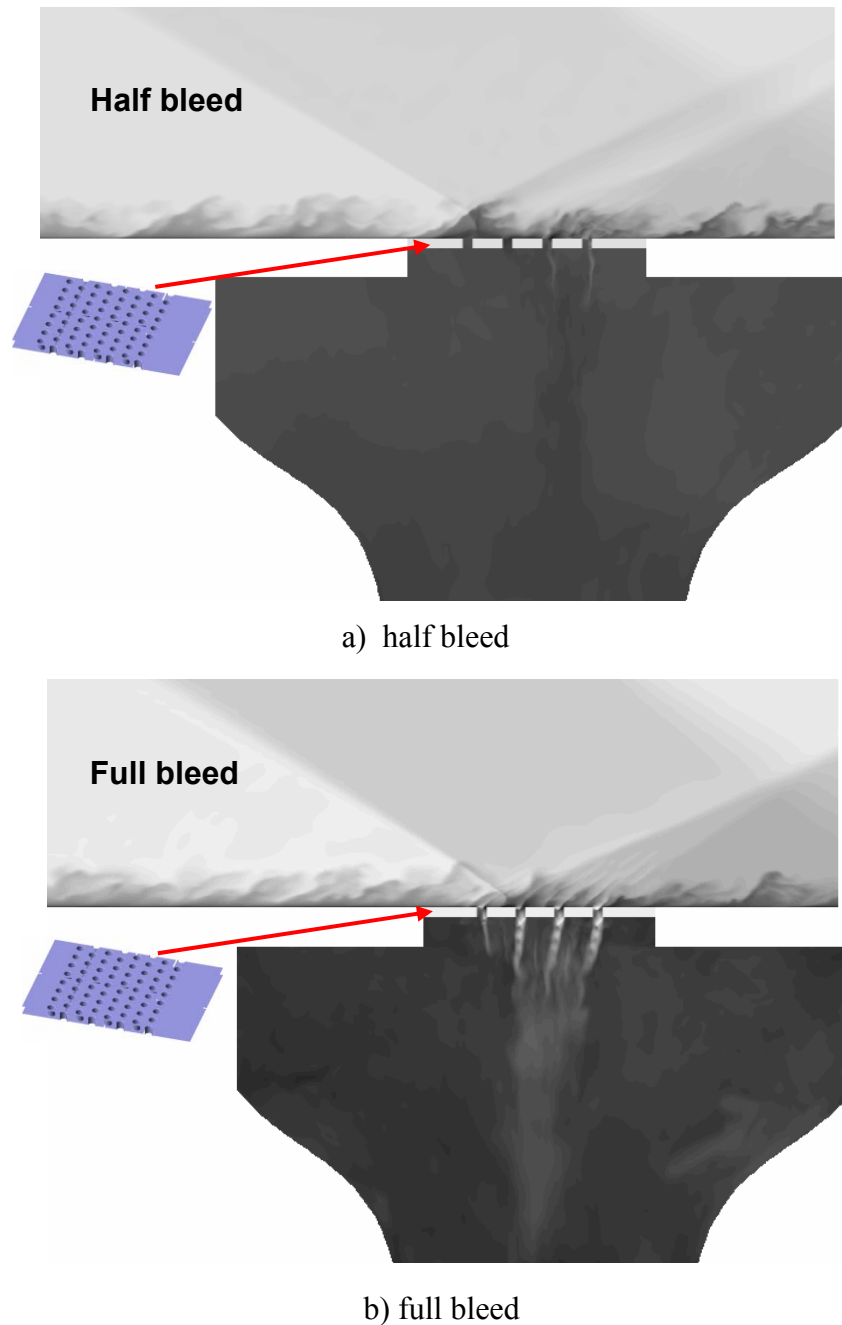
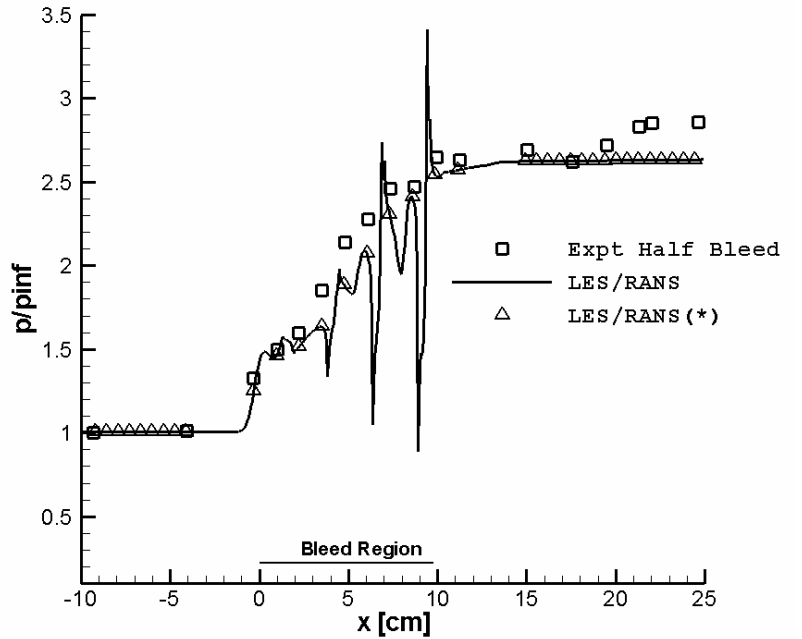
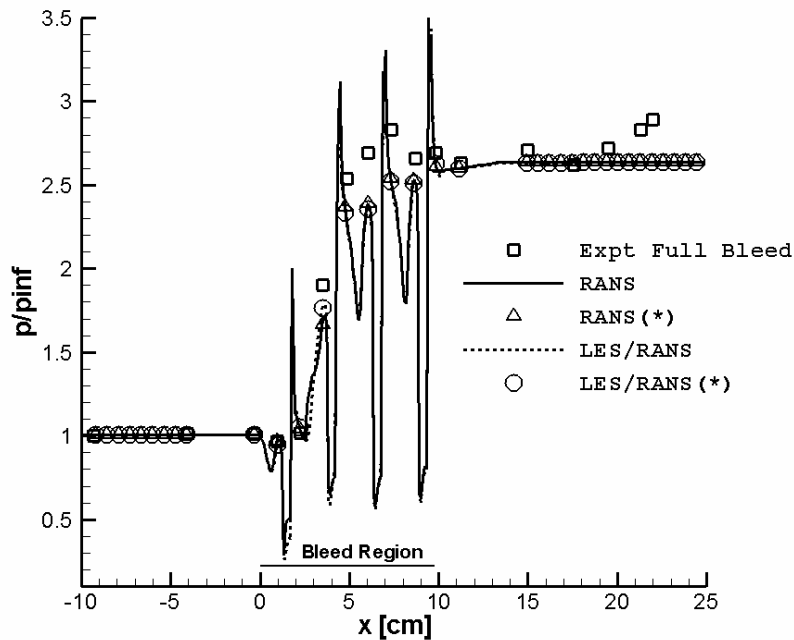


Figure 33: Snapshot of temperature contours with inset bleed plate: shock / boundary layer interaction with bleed

Temperature contours shown in Figure 33 reveal that the bleed array produces localized wave patterns associated with the formation of expansion waves as the near-wall fluid moves into each bleed port and with the formation of a re-compression shock located at the downstream edge of the bleed port. This response occurs for all the bleed ports in the full bleed case but only in the most downstream (last two) ports for the half bleed case. A general thinning of the



a) half bleed



b) full bleed

Figure 34: Wall pressure distributions: shock / boundary layer interaction with bleed; (*) - averaged at pressure tap locations

boundary layer within and downstream of the bleed region is evident, as is a re-compression shock located just downstream of the end of the bleed region. Overall the effects are more pronounced for the full bleed case. Higher temperatures are noted near the vicinity of the shock impingement position for the half bleed case. These are associated with a recirculation region formed due to the shock impingement and enlarged somewhat by air blowing out from the plenum. The free-jet expansion of the bleed-hole fluid as it enters the plenum is less pronounced for in the half-bleed case, due to the higher plenum pressure.

Centerline surface pressure distributions in Figure 34 provide more evidence of the localized expansion / compression events induced by the suction effect. The pressure levels at the surface plane over each bleed port are included in the computational distributions to provide an indication of the local flow patterns. For the full bleed simulation, the LES/RANS and RANS predictions are very similar, and when averaged to the experimental data locations, are in reasonable agreement with the measurements. Surface pressure predictions for the half bleed case also compare reasonably well with the data. It is interesting to note that the localized compression/expansion effects are relatively absent in the upper part of the interaction region for the half bleed case compared to the maximum bleed scenario. This is due to the absence of active suction through the bleed ports in this region for the lower bleed rate. In Ref. [26], some discussion is made of the fact that the measured wall pressure for the maximum bleed simulation is higher in some places than the value obtained through oblique shock theory. The authors argue that situations might arise where, due to the suction effect, flow is directed into the static tap, causing it to read a higher value. Another explanation, furthered by the computational

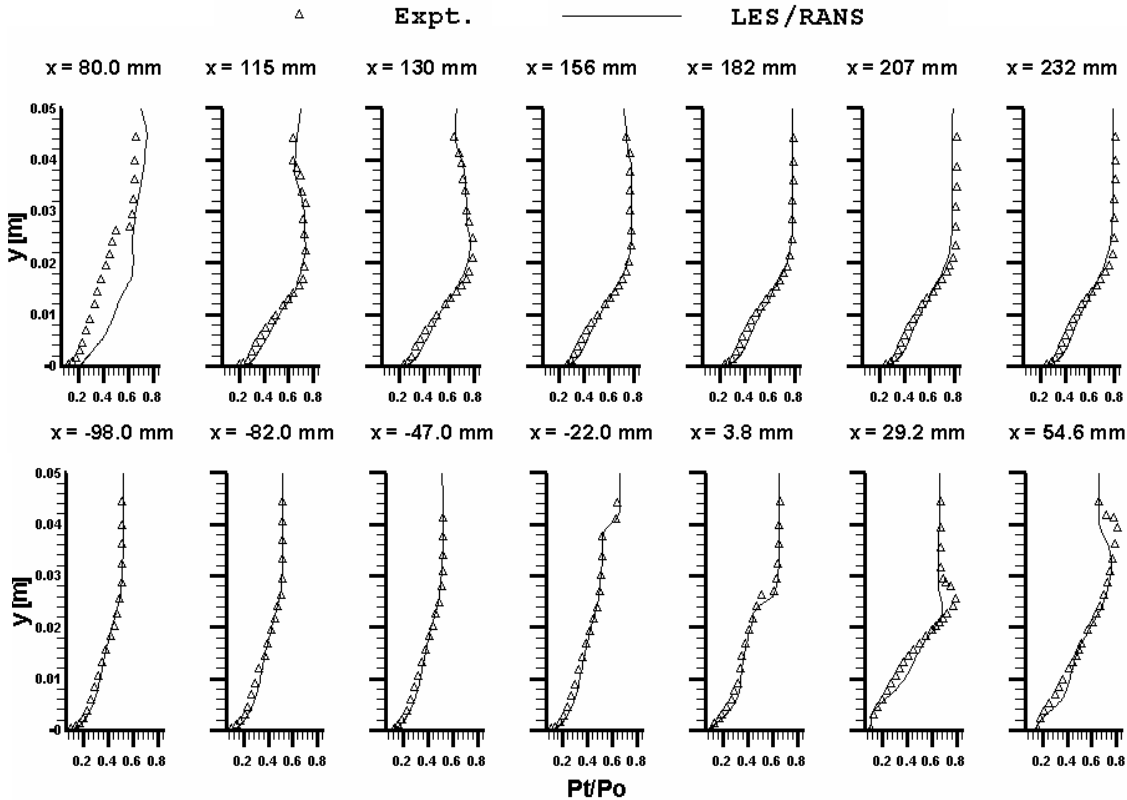


Figure 35: Pitot pressure distributions: shock / boundary layer interaction with half-bleed

results, might be that some of the static taps are very close to a bleed hole and as such, the static taps measure an average value associated with the rapid compression / expansion process occurring at the downstream edge of each bleed hole. It is clear that the bleed effects are highly localized, at least for this particular array.

Pitot-pressure distributions throughout the interaction region are shown in Figures 35 and 36 for the half-and full-bleed simulations. The model predictions are very similar and agree well with the experimental data. The LES/RANS model produces a slightly fuller Pitot-pressure profile near the wall downstream of the bleed region for both the bleed rates. This result is consistent with that evidenced for the case without bleed, in that the LES/RANS model generally provides a more rapid recovery of the boundary layer downstream of a shock-induced

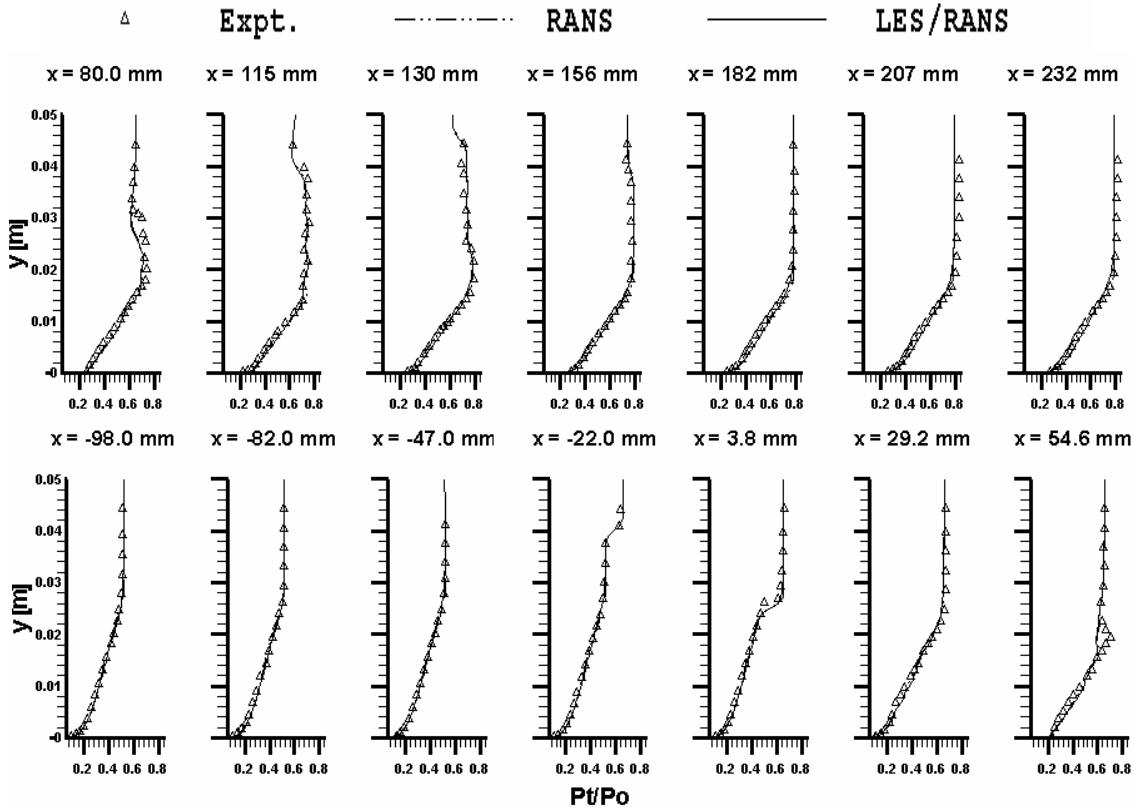


Figure 36: Pitot pressure distributions: shock / boundary layer interaction with full bleed

disturbance. Predictions within in the interaction region, specifically at the 80 mm station, are not quite as good, especially for the half bleed case. This is possibly due to the difference in the structure of the separation shock between experiment and that predicted by computation.

Pitot-pressure distributions extracted at the bleed-hole exit plane (Figure 37) for the full bleed case indicate that the computations under-predict the measured peak pressure level at all axial stations, with the LES/RANS model providing slightly better agreement. This trend is consistent with the under-prediction of the overall bleed mass flow rate mentioned above. It is possible that these results would improve with additional X-Z mesh refinement over the holes.

The bleed mass flux distributions over the entire array for the full- and half-bleed LES/RANS simulations are displayed in Figure 38. Of particular note is the increase in bleed mass flux in the region downstream of the shock-impingement location. This is the expected

trend, as the pressure level is higher in this region. For the full-bleed case, the suction effect is much less for bleed ports located upstream of the shock impingement location. The mass fluxes in this region are similar to those found in the flat-plate boundary layer simulations discussed above. Some localized entrainment of bleed-hole fluid into the boundary layer is noted for the full-bleed case, but a much stronger blowing effect is present for the half-bleed case. This is due to a pressure differential within the plenum caused by the preferential injection of mass downstream of the shock impingement location. Mach number contours and streamlines in Figure 39 indicate that the initial entrainment of fluid into the bleed port occurs through a supersonic expansion that is terminated by a ‘barrier shock’ [13] oriented normal to the flow direction. The lowermost portion of this shock wave interacts with the fluid near the upstream edge of the bleed port, creating a region of

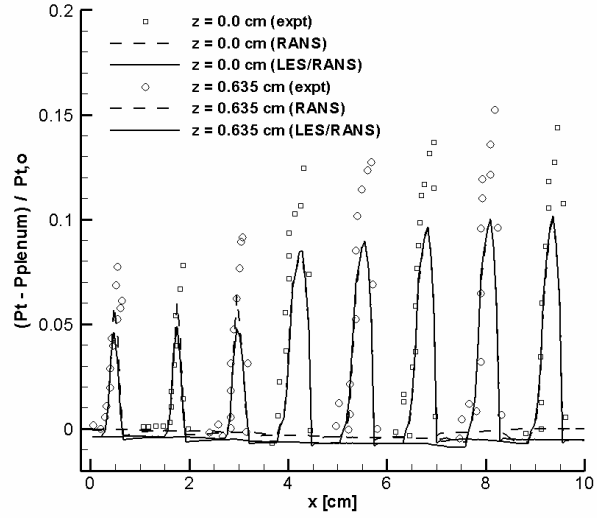


Figure 37: Pitot pressure profiles at exit of bleed holes with full bleed

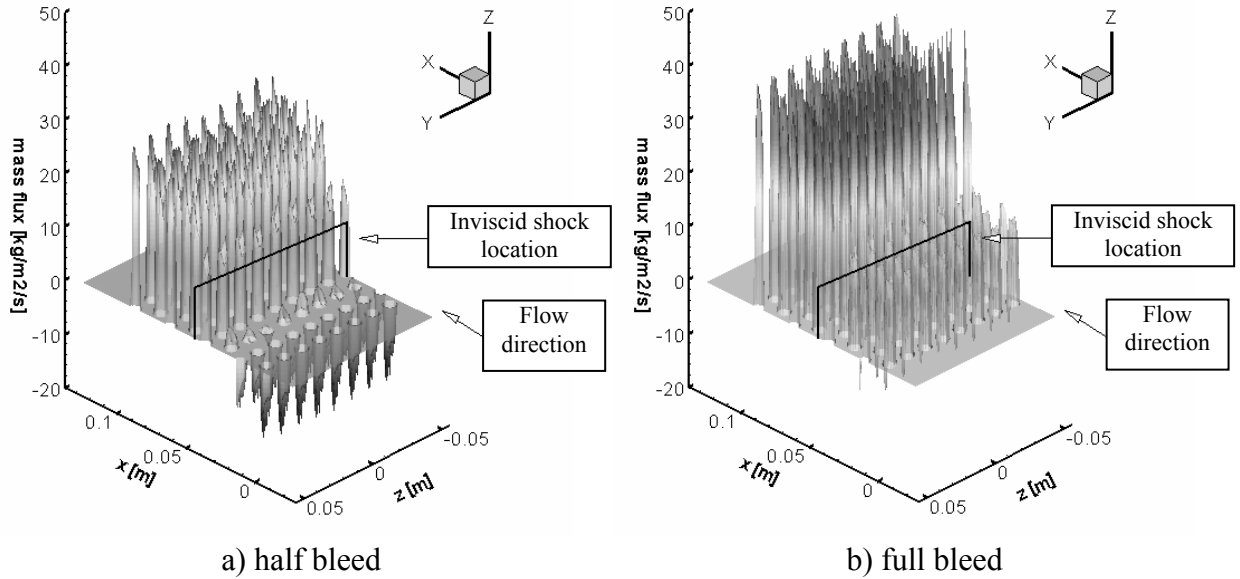


Figure 38: Bleed mass flux distributions

separation that acts to reduce the cross-section area occupied by the core fluid. The growth of this region creates an area minimum, which allows the subsonic flow behind the barrier shock to accelerate to supersonic speeds at the bleed-hole exit. This under-expanded jet then relaxes to the plenum pressure level through a series of expansion and compression waves. The uppermost portion of the barrier shock propagates out of the bleed port. The fluid that passes through this part of the barrier shock is compressed to levels in excess of the average wall pressure and is

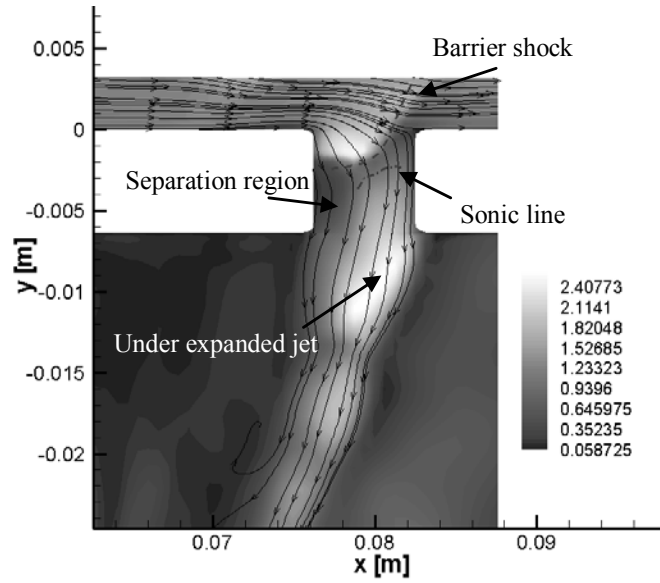


Figure 39: Mach number contours in bleed hole

then expanded as it turns toward the flat-plate surface. This provides the mechanism for the large spikes in the wall pressure distributions shown in Figure 34.

6.3.6. Reynolds-stress evolution and turbulence structure

Turbulence amplification is a well-known characteristic of shock / boundary layer interactions. Bulk compression, streamline curvature, shock oscillation, and the dynamics of separation / re-attachment all contribute to the amplification effect. [36] Large bleed rates as used in the Willis, et al. experiments can essentially remove turbulent separation but also induce other disturbances that could potentially amplify turbulence. Figure 40 plots span-averaged contours of resolved turbulence kinetic energy and resolved Reynolds shear stress ($\overline{\rho u'v'}$) for the LES/RANS cases with and without bleed. For the case without bleed, large Reynolds-stress values are found near the time-averaged position of the separation shock and downstream of the re-attachment location. Further downstream, the stresses begin to relax to levels similar to, but larger than those in the incoming boundary layer. With full bleed, the separation / re-attachment response is eliminated, and very little Reynolds-stress amplification is observed. The half-bleed results indicate that some initial amplification takes place near and upstream of the shock-impingement position, as there is no significant suction effect in this region. Further downstream, the suction effect suppresses the shock system dynamics, and the Reynolds stresses again begin to relax to values similar to those in the upstream boundary layer. The wave patterns generated by flow into the bleed holes generate local disturbances in the Reynolds stresses, but these propagate out of the boundary layer. This result indicates that the dominant source of Reynolds-stress amplification in impinging shock / boundary-layer interactions may be the dynamics of the separation region, which triggers the motion of the separation and re-attachment shocks.

Figure 41 shows iso-surfaces of the swirl strength (10000 s^{-1}) for the interactions with and without full bleed. Visually, the interactions are similar, displaying a general increase in structural content and the presence of more smaller-scale structures within and downstream of the interaction region. A more quantitative measure, shown in Figure 42, is obtained by

calculating the probability density function of the logarithm of the swirl strength at different streamwise locations. The most probable value is indicated as the peak in the distribution, and a

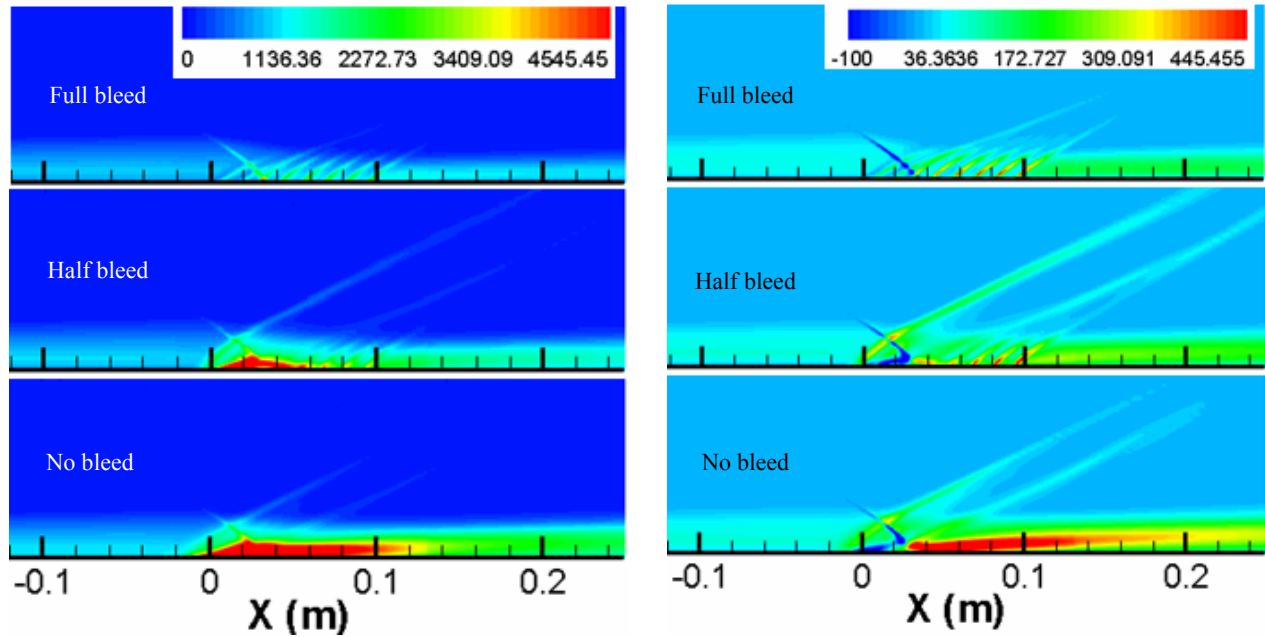


Figure 40: Evolution of resolved turbulent kinetic energy (left) and resolved Reynolds shear stress (right) through the interaction region

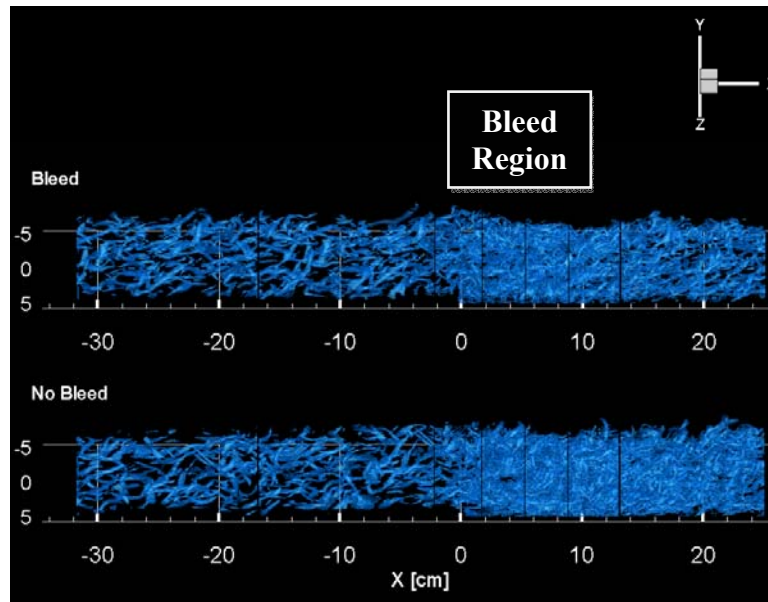


Figure 41: Iso-surfaces of swirl strength (10000 s-1) for interactions with full bleed and no bleed

shift in the distribution to the right implies an increase in the population of more tightly-wrapped (finer-scale) vortical structures. This can also imply a general decrease in turbulence length scales. For the interaction without bleed, the most probable swirl strength value increases by

about an order of magnitude as the flow separates, then re-attaches. In the recovery region, the most probable swirl-strength value decreases, and the distribution approaches that of the upstream boundary layer. With bleed, the distributions do not deviate as much in the interaction region, though the trend of an increasing population of finer-scale structures still holds. The swirl-strength distributions in the recovery region are close to those in the incoming boundary layer, again showing that the bleed effect accelerates the recovery of the boundary layer to a new equilibrium state following the shock reflection.

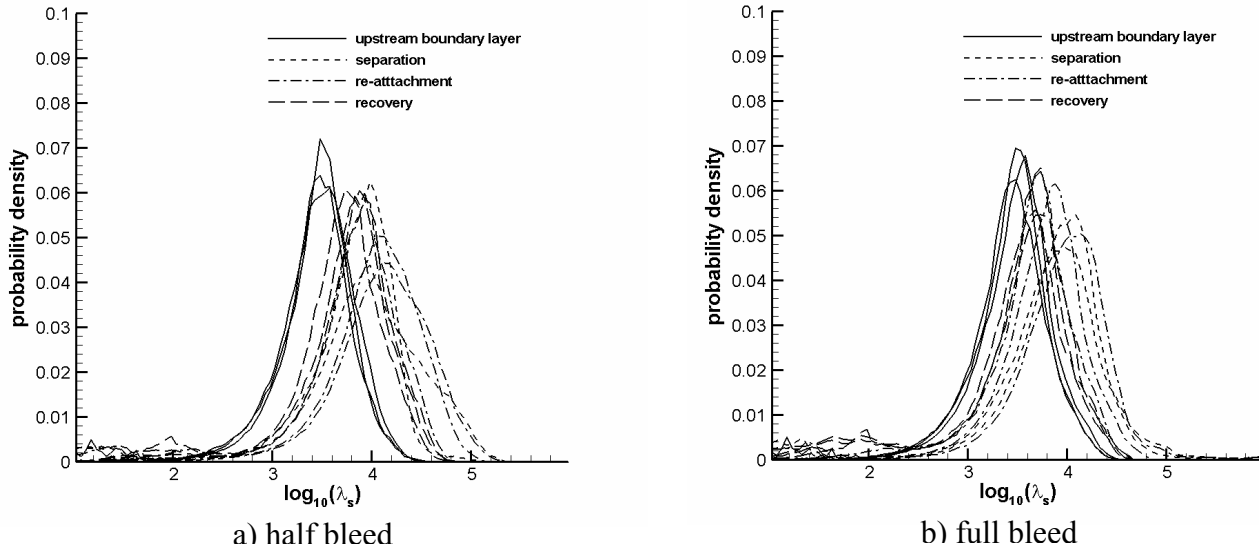


Figure 42: Evolution of swirl-strength probability density distributions

6.4. Mesoflap Control of Shock / Boundary Layer Interactions

The third set of calculations presented in this work applies the LES/RANS/IB methodology to examine shock / boundary layer interaction control using arrays of mesoflaps, which are rendered as immersed bodies and can deform dynamically in response to time-varying pressure loads. We consider quasi-steady simulations using a 2-D RANS solver, similar to Wood, et al. [32] as well as fully dynamic simulations using the LES/RANS model.

6.4.1. Experiment details

Experiments involving mesoflap arrays having different thicknesses, layouts and arrangement to control SBLIs, have been performed at the University of Illinois [6-8]. The experiments were performed at a nominal Mach number of 2.45, a stagnation temperature of 300 K, and a Reynolds number / meter of 57×10^6 . The test section in the wind tunnel is 50.8 mm high and 50.8 mm wide. Data collected in these experiments includes centerline axial velocity data obtained at various streamwise stations using one-component laser Doppler velocimetry (LDV) and wall static pressure distributions. The velocity data has been used for generating profiles of streamwise normal stress intensity and boundary layer integral properties. This work focuses on two of the UIUC experiments:

- An oblique shock / turbulent boundary layer interaction at Mach 2.45 induced by a 8-degree wedge placed on the upper wall of the wind tunnel (LDV velocity data, surface pressure measurements)
- The same oblique shock / turbulent boundary layer interaction with the addition of an array of six third-generation [7] mesoflaps of thickness = $76.2 \mu\text{m}$ in the shock interaction region (LDV velocity data, surface pressure measurements).

The mesoflap system consisted of a steel frame with supporting spars with the mesoflap array made of nickel-titanium (nitinol) epoxied to it. The mesoflaps were 4.63 mm long, spanned about $\frac{3}{4}$ of the wind tunnel and had a thickness of $76.2 \mu\text{m}$. The mesoflap system enclosed a cavity which was 44.5 mm wide and 19.1 mm deep. The leading edge of the first mesoflap (counted from upstream to downstream) was located at ~ 22.25 mm from the center of the cavity (which was also the shock impingement location). This location has been denoted as x_0 in the experiment and also in this work. For convenience, the computational domain used in this work (detailed in the next section) sets $x_0 = 0$. The leading edge of the shock generator was placed at $19.4\delta_0$ upstream of x_0 , which was also the location where the inflow boundary layer properties

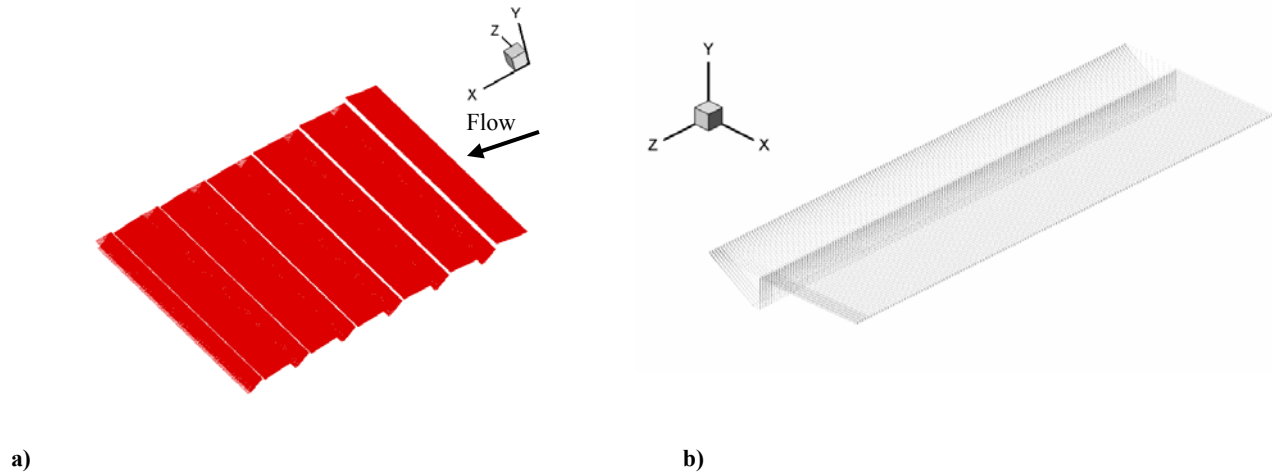


Figure 43: 3-D views of mesoflap; a) deflected mesoflap array with flow direction indicated, b) a single mesoflap (entire width in z direction not shown for compactness)

were calculated in the experiment. In the computational domain, the shock generator position was adjusted such that the inviscid oblique shock impingement location was approximately at x_0 . The boundary layer thickness at the inflow plane, δ_0 was determined as 4.0 mm by fitting the velocity data to the experimental curve fit due to Sun and Childs [37]. The compressible displacement thickness and momentum thickness were also calculated from the curve fit as $0.27\delta_0$ and $0.075\delta_0$ respectively. Velocity profiles were collected at streamwise stations of $x = -19.4\delta_0$ mm, $x = -0.12 \delta_0$, $x = 2.26 \delta_0$, $x = 8.73\delta_0$, $x = 15.0\delta_0$ for the SBLI without any control. For the case with the mesoflap array in place, velocity data was collected at locations downstream of the mesoflap array at $x = 8.73\delta_0$, $x = 13.4\delta_0$ [7].

6.4.2. Computational domain and calculation details

The primary domain (that containing the shock generator and incoming boundary layer) extends from $X = -99.05$ mm to $X = 60.65$ mm in the streamwise direction and from $Y = 0$ to $Y = 58.0$ mm in the wall normal direction at the start of the domain, reducing to ~ 39.8 mm at the trailing edge of the shock generator. For the 2-D quasi-steady FSI simulations, the spanwise width of the domain is one mesh cell. For the LES/RANS simulations, the computational domain extends from $Z = -19.4$ mm to $Z = 19.4$ mm in the spanwise direction. The streamwise and spanwise mesh spacing is $\sim \delta_0/15$, and the minimum mesh spacing in the wall-normal direction is 0.005 mm. For the cases with the mesoflap array in place, another domain for the plenum was added. The plenum, which is covered on its top by the mesoflap array, extends from $X = -22.25$ mm to $X = 22.25$ mm in the streamwise direction and from $Y = 0$ mm to $Y = -19.1$ mm in the wall normal direction. The spanwise extent of the cavity is same as for the corresponding primary domain. The number of cells used for the upper domain in the LES/RANS computations is ~ 18.66 M with the plenum containing an additional ~ 1.55 M cells. The array of mesoflaps (including the spars) is rendered as a collection of IB surfaces. Figure 43 shows a single flap structure with the fixed spar. The number of points required in rendering the array structure is 791453.

No-slip, adiabatic-wall boundary conditions are imposed on all solid surfaces (excepting the upper wall including the shock-generator and plenum walls where a slip wall condition is imposed) for both cases. The value of power law chosen in different parts of the mesoflap is as follows – $k = 1$ for the flap upper and lower surface and $k = 1/9$ for all other surfaces. A linear power-law is used to define the near-surface velocity interpolation for surfaces in which the mesh spacing (normal) near the surface is sufficient to resolve the viscous sub layer. Periodic conditions are used in the spanwise directions. For the shock / boundary-layer interactions, slip-wall conditions are applied along the upper boundary, and properties are extrapolated from the interior at the downstream boundary. Boundary conditions for the flat plate boundary layer study were same (on the lower wall, upper wall and downstream boundary) as for the SBLI studies.

To determine the inflow conditions for all the SBLI studies, a flat-plate simulation at the test-section conditions was first performed to determine the place at which the predicted boundary layer properties most closely matched the experimental data at $X = -19.4 \delta_0$. Flow properties at the inflow plane of the computational domain were then extracted from the flat plate solution at a location consistent with the position of the inflow plane relative to the measurement location. Convergence of the RANS calculations was ascertained using three measures: relative decrease in residual norm, constancy of surface quantities, and constancy of the global mass flow rate. For the quasi-steady FSI simulation, the convergence of the mesoflap position was monitored using changes in the computed displacements of the flaps. The LES/RANS calculations were initiated by super-imposing scaled boundary-layer fluctuations from an earlier calculation onto part of a converged RANS solution. After several flow-through times to eliminate initial transients, time-averaged statistics for the LES/RANS calculations were collected over a minimum of seven flow-through times, based on the domain length and free-stream velocity. The LES/RANS calculation involving the mesoflap array was run for a longer duration ~ 12 flow through times. This was done to discern a pattern in the mesoflap displacements and to determine the dominant response frequencies.

6.4.3. Oblique shock / boundary layer interaction without mesoflap array

A 3-D view showing snapshots of pressure contours on a streamwise X-Y plane and axial velocity on a near surface plane (X-Z) is shown in Figure 44 for the LES/RANS model. The iso-surface of zero axial velocity, indicating the separation bubble, is colored in blue. The figure

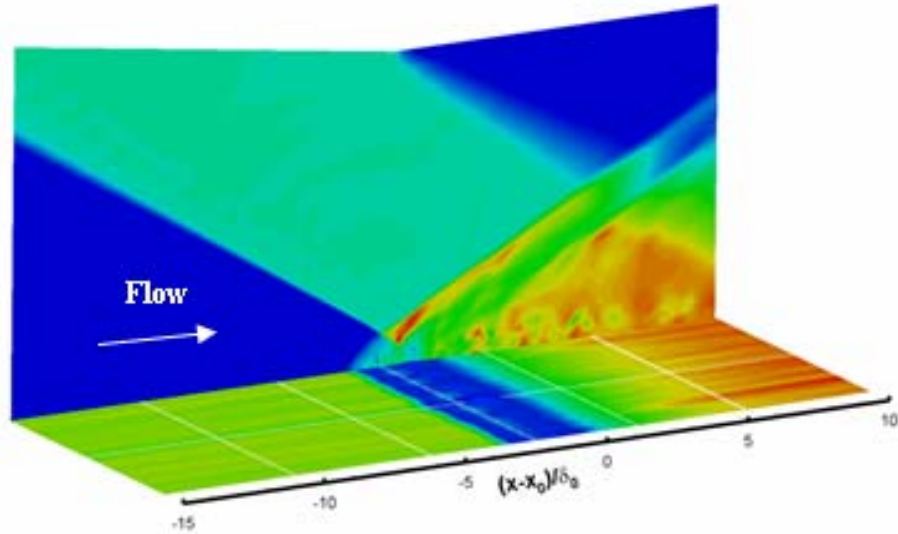


Figure 44: Snapshot of contour plots of pressure on an X-Z plane (close to surface) and axial velocity an X-Y plane; iso-surface of zero axial velocity shown in blue on the near surface plane

shows the impinging and reflected shock structure showing that the zero axial velocity iso-surface originates approximately at the location of separation shock. The separation bubble has ‘bumps’ and ‘troughs’ which can be discerned when seen closely. These are due to streaks of high and low-momentum fluid in the incoming boundary layer close to the surface. Figure 45

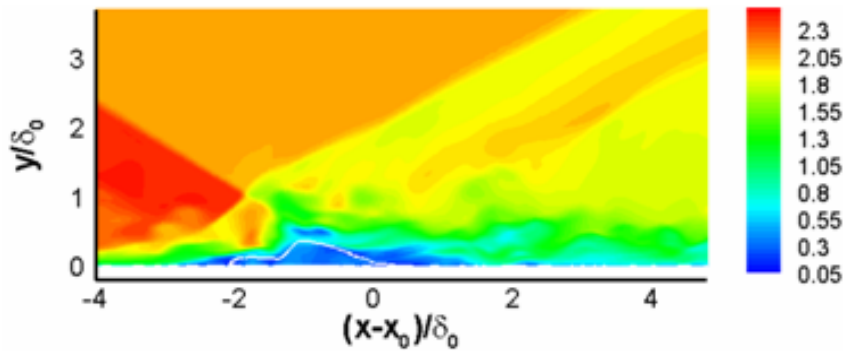


Figure 45: Snapshot of Mach number contours showing in white the zero axial velocity boundary

shows a 2-D close up view of the separation region with a white line indicating the location of zero axial velocity.

Figure 46 shows the centerline wall pressure distribution compared with experimental data for the oblique shock interaction with no control. The Menter SST RANS model appears to over-estimate the level of upstream influence of the interaction (indicated by the separation-shock pressure rise). The LES/RANS model provides slightly better predictions. In the experiment, a gradual rise in pressure is observed upstream of the interaction region from about $((X - X_0)/\delta_0 = -10$, which has been attributed to effects of reduced free stream Mach number due to boundary layer growth in the test section. This is not reflected in the numerical data and might be due to the fact the boundary layer on the upper wall (treated as a symmetry boundary in computations) is not resolved. The computations over-predict the pressure level downstream of the impingement position. It is not clear why this might be happening. Beyond this region the expansion fan generated at the trailing edge of the shock generator hits the lower wall, which is reflected by the drop in the surface pressure. The predictions in this region are accurate for both computations.

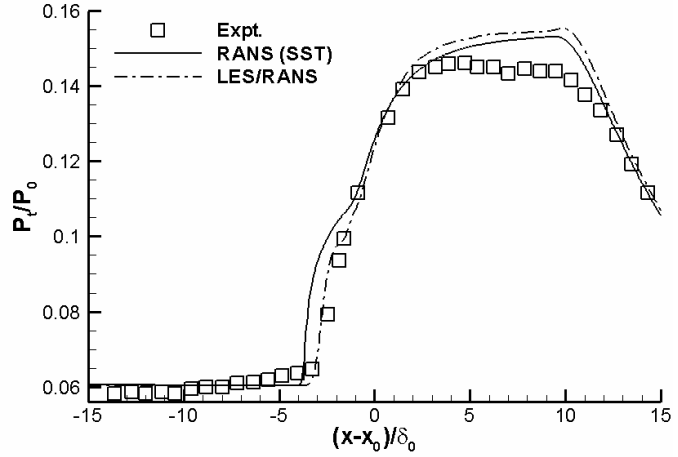


Figure 46: Centerline wall pressure for SBLI without control

Figure 47 shows experimental and computed centerline axial velocity profiles at different streamwise locations. The numerical predictions of axial velocity at the inflow $((X - X_0)/\delta_0 = -19.4)$ are in good agreement with experimental data, with both RANS and

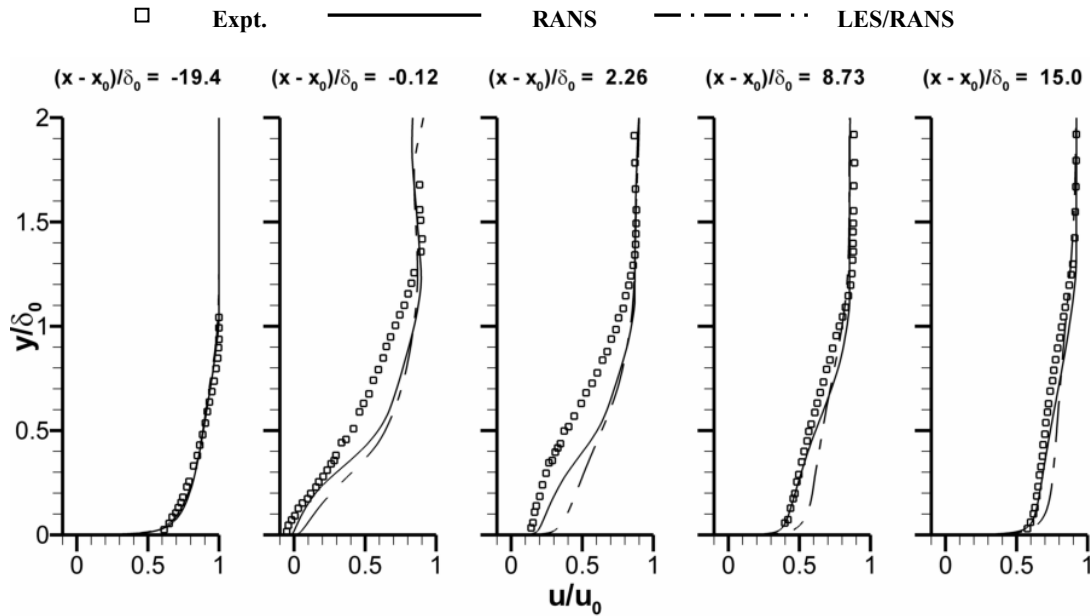


Figure 47: Centerline axial velocities for shock/boundary layer interaction without control

LES/RANS profiles being somewhat more full in the near-wall region ($y/\delta_0 < 0.4$). In the interaction region ($(X - X_0)/\delta_0 = -0.12, 2.26$) the numerical predictions show significant deviations from experimental data. The wake-like profile present in the experiment is less evident in the computed profiles, more so for the LES/RANS predictions. This is most evident at the $(X - X_0)/\delta_0 = 2.26$ station. This is suggestive of differences in the shape and/or location of the separation bubble between the experiment and the computations. The experimental profile is suggestive of a thicker separation bubble. A possible reason for this might be the fuller near-wall velocity profile predicted at the inflow, which would be more resistant to separation. The last two stations are downstream of the interaction, and the computational predictions are closer to the LDV data. Here, the LES/RANS method tends to over-predict the recovery rate of the inner part boundary layer, compared to the RANS model. This trend has been observed in some previous applications of the LES/RANS method in compression-ramp interactions [15] and may be indicative of higher turbulence intensity near the wall.

Figure 48 compares predicted streamwise turbulence intensity profiles (resolved stresses for the LES/RANS model) at different streamwise locations with experiment. Three sub-plots are

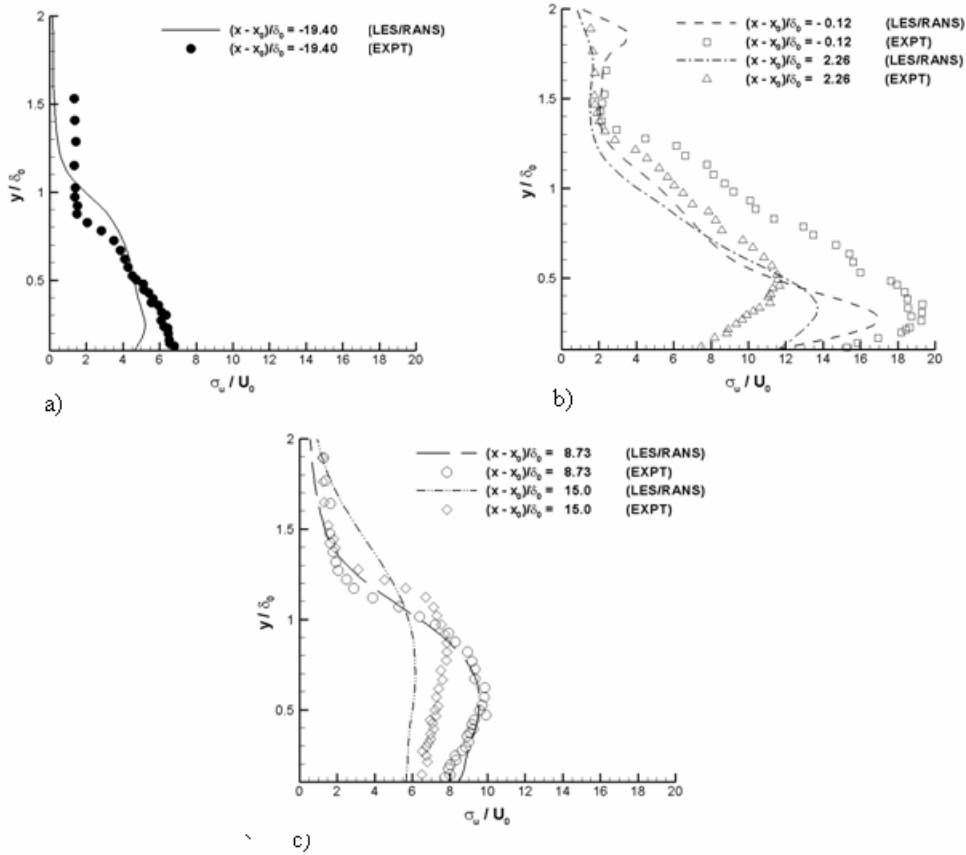


Figure 48: Streamwise turbulence intensity profiles at various streamwise locations; a) inflow, b) interaction region, and c) downstream

developed by categorizing the streamwise stations into inflow (a), interaction (b) and downstream (post-interaction; c) zones. The turbulence intensity levels are on the average under-predicted. At the inflow station, the free-stream turbulence level is rather high $\sim 2\%$ compared to

the calculation. In the interaction region, the location of maximum turbulence intensity shifts away from the wall. Within the separation region ($(X - X_0)/\delta_0 = -0.12$), the location of the peak is under-predicted but is in better agreement with experiment at stations further downstream. The turbulence intensity level is under-predicted at the station just downstream of the re-attachment position ($(X - X_0)/\delta_0 = 2.26$). The turbulence intensity profiles downstream of the interaction show better agreement with experimental data, with excellent agreement observed at the $(X - X_0)/\delta_0 = 8.73$ station. Overall the LES/RANS predictions fare reasonably well compared with experiment, with better results obtained upstream and downstream of the interaction. This is again suggestive of differences in separation-bubble geometry and possibly interaction dynamics in that region.

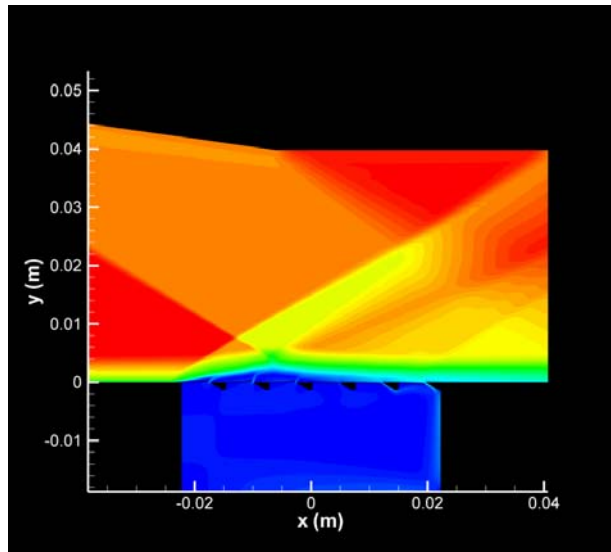


Figure 49: Mach number contours for the converged configuration of the mesoflap array

6.4.4. Flow structure of oblique shock / boundary layer interaction with mesoflap array – 2-D quasi-steady FSI modeling (RANS)

Two different approaches have been used to account for the effects of meso-flap control: a 2-D simulation which uses a quasi-steady modeling for the structure and uses a RANS turbulence (Menter SST) closure, and a 3-D simulation which employs a dynamic modeling for the structure and uses the hybrid LES/RANS turbulence closure.

Figure 49 shows the Mach number contours for the converged configuration of the mesoflaps as modeled using the quasi-steady, 2-D approach. Fluid is entrained into the cavity through the slots furthest downstream of the shock impingement point and is injected from the cavity into the boundary layer through the slots furthest upstream of the shock impingement point. The mesoflaps are numbered from the upstream end, so mesoflap 1 is the farthest upstream and mesoflap 6 is farthest downstream. As can be observed, mesoflaps 1 and 2 and 5 and 6 are primarily responsible for the flow into and out of the cavity. Mesoflaps 3 and 4 deflect very little, allowing only minimal fluid exchange between the upper domain and the plenum.

This trend is very consistent with that observed in the experiments [6,7]. Figure 50 shows the maximum deflection (which is also the edge deflection) of each mesoflap at each structural iteration. To improve the code's response in the initial transient periods, a first order spatial discretization was used for fluid solver to begin with, and when the deflection pattern showed a

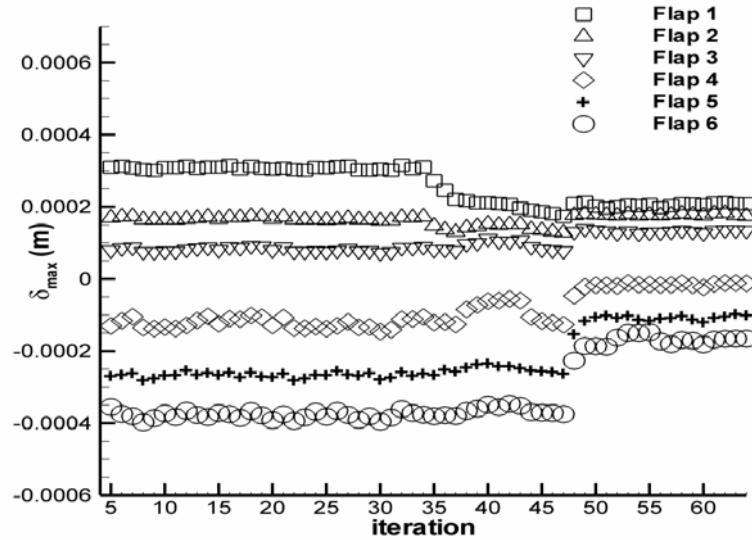


Figure 50: History of maximum deflection of each mesoflap with iteration

reasonable convergence, the higher-order PPM discretization was turned on. There is a sharp change in the deflection pattern of the upstream flaps at around the 34th structural iteration which roughly corresponds to this change in the order of accuracy. It is interesting to note that the upstream mesoflaps (1-2) tend to converge faster than the downstream (5-6) ones.

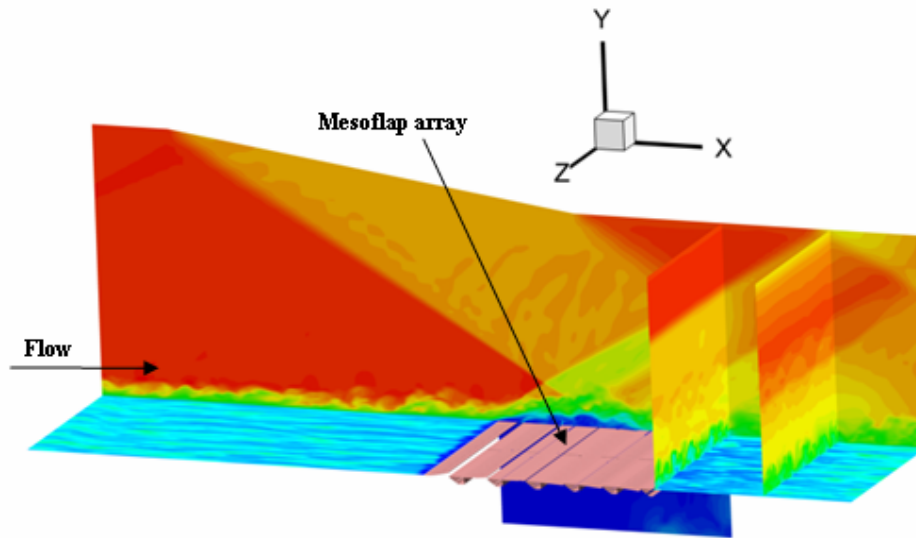


Figure 51: Mach number contours for shock/boundary layer interaction with control by mesoflap array

6.4.5. Flow structure of oblique shock / boundary layer interaction with mesoflap array – 3-D dynamic FSI modeling (LES/RANS)

Figure 51 shows a 3-D view of the deflected mesoflap array with a snapshot of Mach number contours shown. The trace of the leading edge shock can be seen on the X-Y plane, with a low Mach number region being present over a large portion of the mesoflap array. A sequence

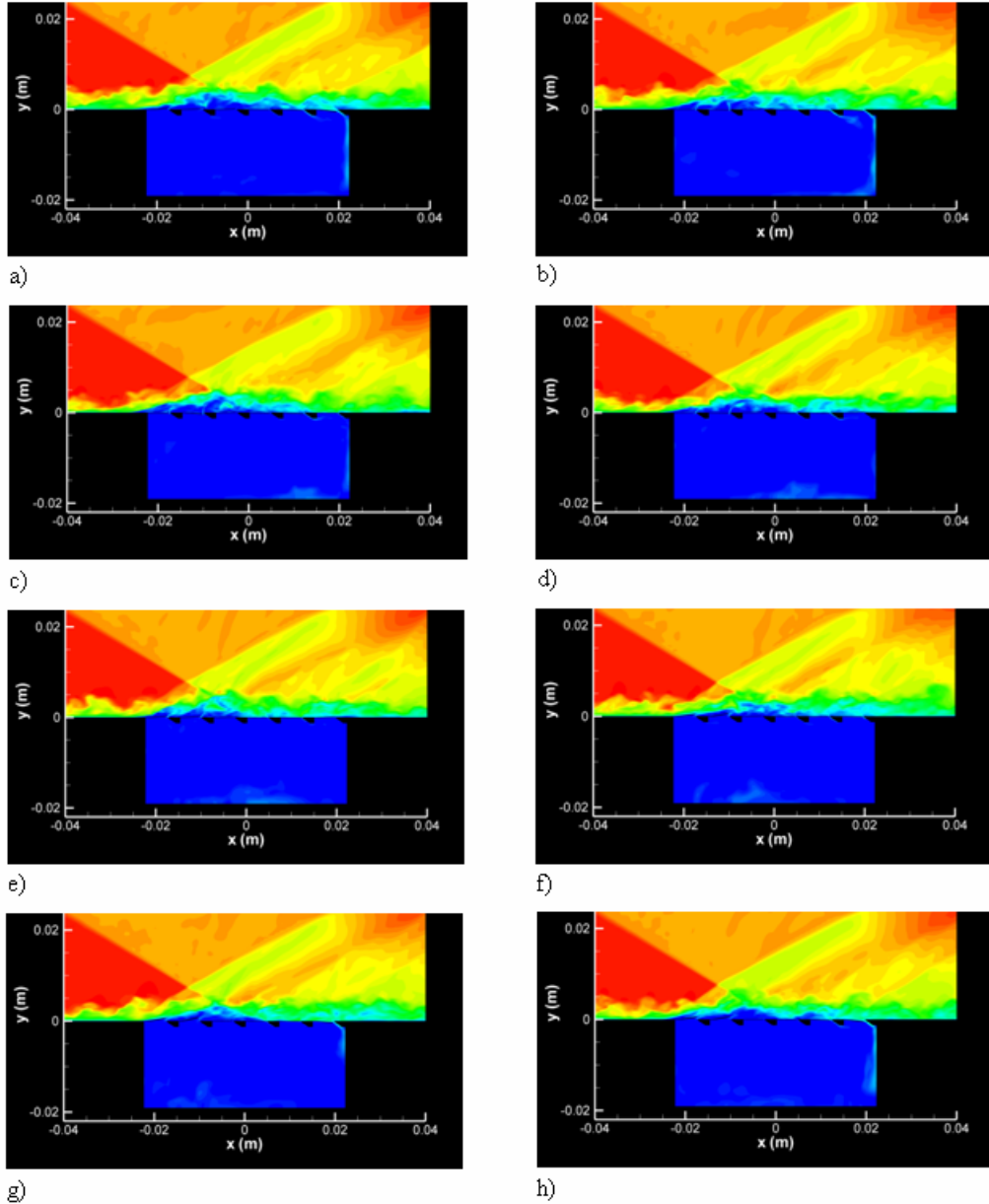


Figure 52: Snapshots of Mach numbers contours; frames are spaced at intervals of 600 iterations ~ 0.09 ms

of Mach number snapshots is shown in Figure 52 to illustrate the dynamics of the flow with the mesoflap array in place. The sequence spans ~4200 iterations which covers about 0.63 ms in physical time. It can be seen that injection and bleed happen simultaneously at the upstream

and downstream mesoflaps, respectively. The angle at which the fluid is injected from the cavity into the core flow or bleeds into the cavity from the core flow is dependant on flap configuration. As observed in the quasi-steady simulation, it is evident that the intermediate flaps (3, 4) do not play a major role in the transpiration process. Angled injection at the most upstream flap seems to energize the flow (leading to a reduction in the low Mach number region) whereas at the second flap, injection tends to swell up the separation bubble forming just downstream of it. The maximum amount of bleed occurs at the most downstream mesoflap.

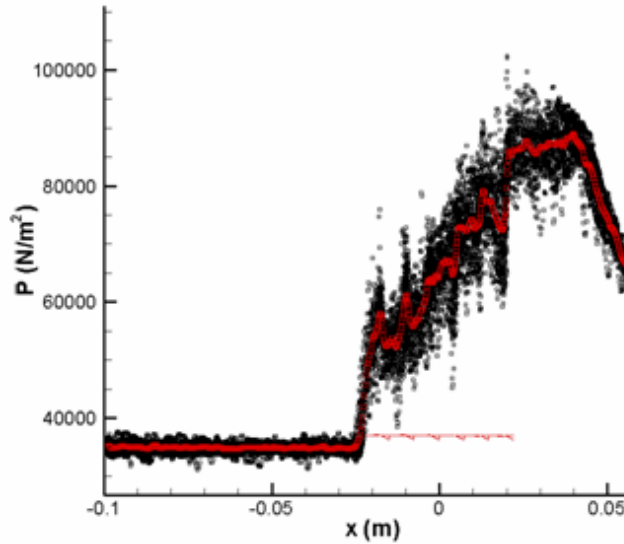


Figure 53: Wall static pressure history with the time averaged value shown in red

Figure 53 shows the history of wall pressure spanning 4200 iterations which is about 0.63 ms, with data spaced at 200 iterations. The figure also shows the location of the mesoflap array in the lower part of the frame to help identify patterns in the time-averaged data. The time-averaged data (red line) shows a compression followed by a sharp drop in pressure at a couple of mesoflap locations upstream of the $X = 0$ position and one prominent expansion followed by a sharp compression near the end of the flap array. For the pattern noted upstream of $X = 0$, the rise in pressure corresponds to compression of the fluid as it bends into itself at the upstream flaps, which in a time average sense deflect upward, followed by an expansion at the trailing edge of the flap to approach the average pressure value. An expansion occurs at the farthest downstream flap as the fluid bends away due to the downward deflection of the flap (in the time-average sense), and then recompresses to average values at the trailing edge. The pressure data does not reveal a clear pattern for the remaining flaps, which possibly indicates that these flaps respond less dynamically to the pressure loads.

The deflection history (20 K iterations ≈ 3 ms) of the flaps is shown in Figure 54 with the time-average position shown in red. The flaps are represented as straight lines which can be thought of as a projection of their upper surfaces on a plane normal to its edge. It is clear from the figure that the maximum deflections (again, in a time-average sense) occur at the two most upstream flaps and the farthest flap downstream. This corroborates the observations made above for the wall pressure data. Figure 55 shows a comparison of the time-averaged deflections of each mesoflap as calculated from the quasi-steady and the dynamic FSI models. Also shown is

the interpolated pressure loads (time- and span-averaged for the 3-D calculations) acting on the flap surfaces. The figure shows that, in general, the mesoflaps deflect to a greater extent in the

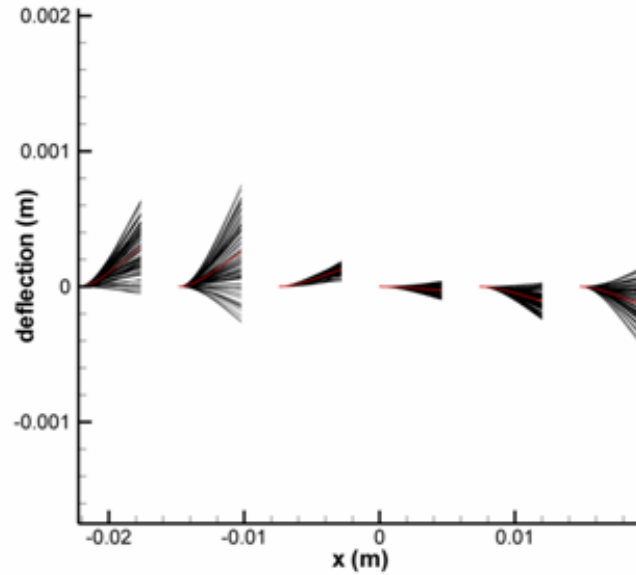


Figure 54: Deflection history of the six flaps (represented by 1-D beams) with the time-averaged position shown in red

dynamic modeling. The net pressure load which is based on summation (with proper sign) of span-averaged pressures on the upper (negative) and lower (positive) surface of the flaps shows a similar trend. This is consistent, as higher loads would result in greater amount of deflection.

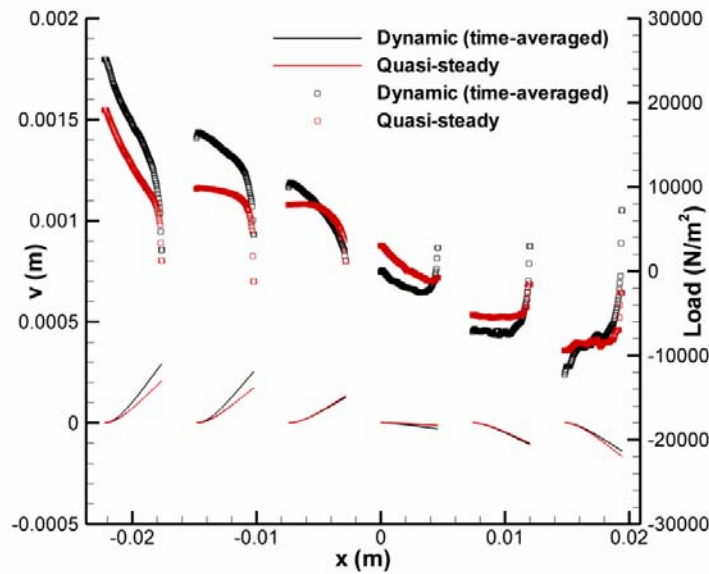


Figure 55: Deflection and interpolated net pressure load (on flap surfaces) comparisons for the quasi-steady and dynamic modeling of the mesoflaps; loads - symbol, displacement - solid lines.

Also to be noted is that the loads acting on the upstream flaps are primarily positive (in the upward direction) while that for the downstream flaps are primarily negative (in the downward direction). It is also clear that magnitude of the net loads tend to increase as one moves away from the center which also corroborates the deflection patterns observed.

Figure 56 shows the frequency response of the mesoflap array due to the time-varying loads acting on it. This is not a response spectrum in the sense used in structural mechanics but more of an investigation of what frequencies might be playing a role in determining the dynamic response of the flaps. Since no damping has been added to the system and there is no algorithmic damping provided by the time integration method chosen, any initial transient or numerical noise would not be damped out. The reason for not using damping was to look into the maximum possible response of the system which would have been altered by the presence of damping. Also since we were not really focusing on obtaining a steady oscillation pattern for the mesoflaps, this

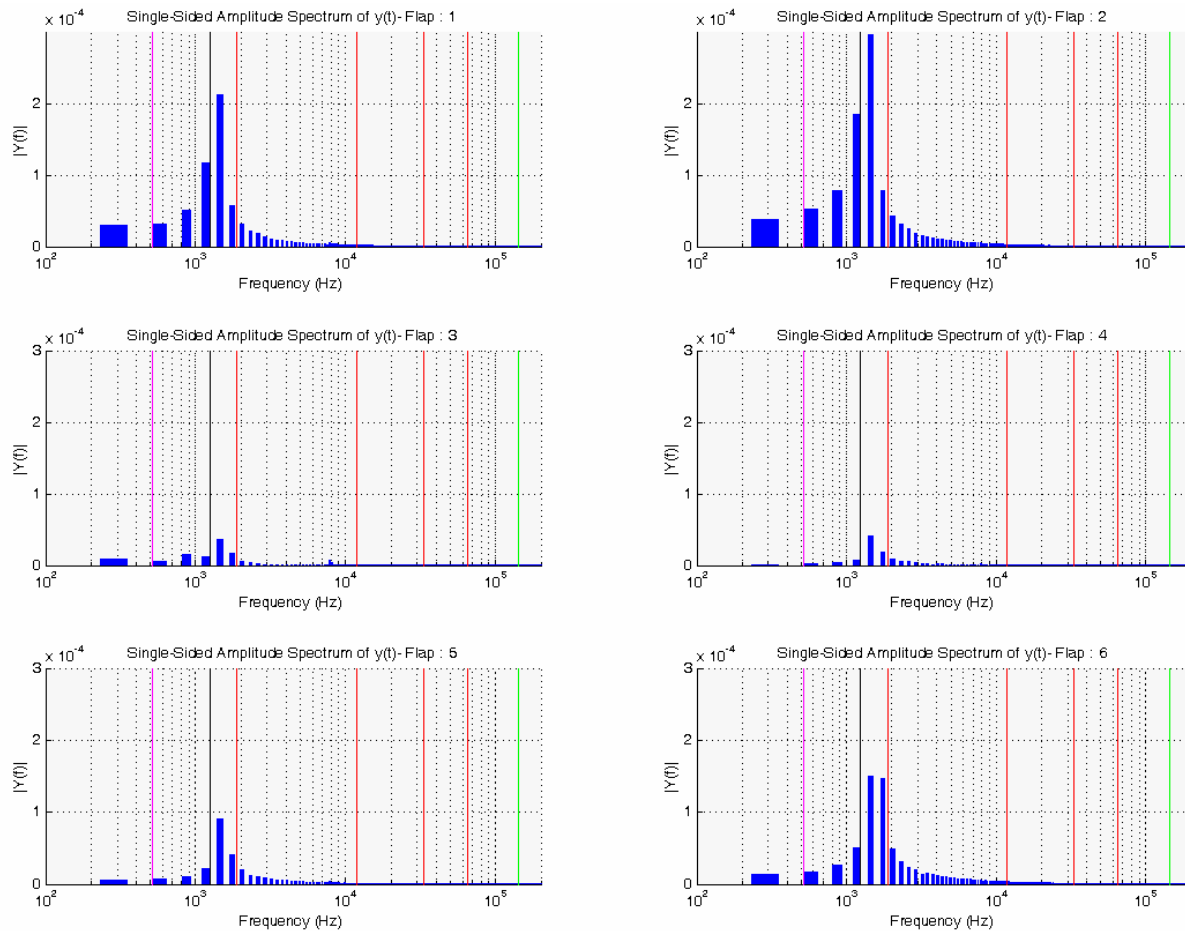


Figure 56: Frequency analysis of flap–response (blue) based on the displacement of the edge of the flap; red: natural frequencies (four shown), black: low frequency shock motion, green: boundary layer turbulence frequency, pink: frequency based on recirculation time in cavity

was justified. As such the peaks in the plot are considered to represent the driving frequencies responsible for the large scale flap response. There are two predominant peaks in the plot for each of the flaps and both of these are less than the fundamental frequency of the mesoflap (first natural frequency of the modeled cantilevered beam). Some relevant frequencies (and also the

first four natural frequencies) are also shown in the figure to evaluate whether any of these have an impact on the flap dynamics. The line in black correspond to the low frequency motion characteristic of similar shock / boundary layer interactions, $\sim 115 \frac{U_\infty}{\delta_0}$ [38], the green line represents a characteristic frequency associated with the largest eddies in the incoming boundary layer, $\frac{U_\infty}{\delta_0}$ and the pink line is a frequency based on a quantity termed here as the recirculation time τ_{rec} , i.e. the time required for the fluid injected from the cavity into the core flow to re-enter the cavity and go out again, and has been derived as a gross approximation in this work. To derive this quantity, average near wall (parallel to wall) velocities are calculated for all the three walls and top (near flap array) of the cavity using time and span-averaged velocity data.. A further approximation is made about the velocity at the top wall (basically flap region) of the cavity which is evaluated as the average of the free-stream velocity U_∞ and velocity calculated as described above. τ_{rec} is then calculated as the time it will take for any scalar to traverse the entire perimeter of the cavity based on the average velocities computed. The frequency is then given by $1/\tau_{rec}$. As evident from the figure, it seems that the frequency which seems to have the strongest influence on the flap response is the low frequency shock motion. The computational time used for the present calculations (after initial transients) is ~ 3.6 ms which roughly corresponds to about 4.45 time periods of the low frequency oscillation. The magnitude of the dynamic response matches well, qualitatively, to the flap responses as evident in Figure 54. For illustration, the maximum amplitude of the response in Figure 56 is for flap 2 which can be seen clearly by the range of the tip motions in Figure 54.

6.4.6. Oblique shock / boundary layer interaction with mesoflap array – data comparisons

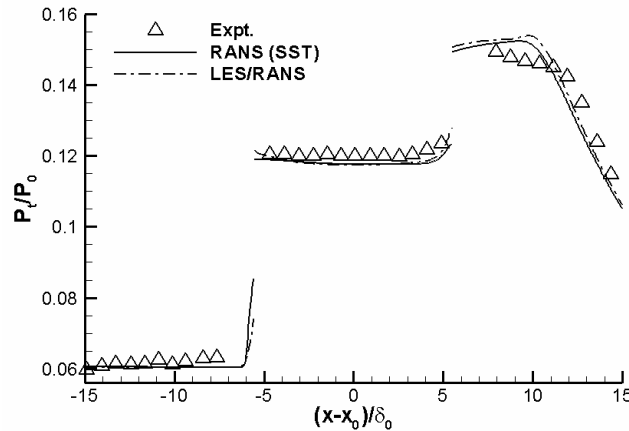


Figure 57: Centerline wall pressure for SBLI with control; pressure at the lower wall of cavity is shown for the region of the mesoflap array (-5.6 to 5.6 on the X axis)

Figure 57 shows the centerline wall pressure data for the experiment and computations. The numerical predictions are in reasonable accord with the wall pressure at the upstream and downstream regions of the cavity on the whole. The pressure rise starts further upstream in the domain than in the no-control case, which is due to a stronger leading edge oblique shock. Data is not available in the region just upstream and downstream of the cavity due to the stringer plate (to which the flap array is epoxied). The higher pressure observed downstream of the interaction

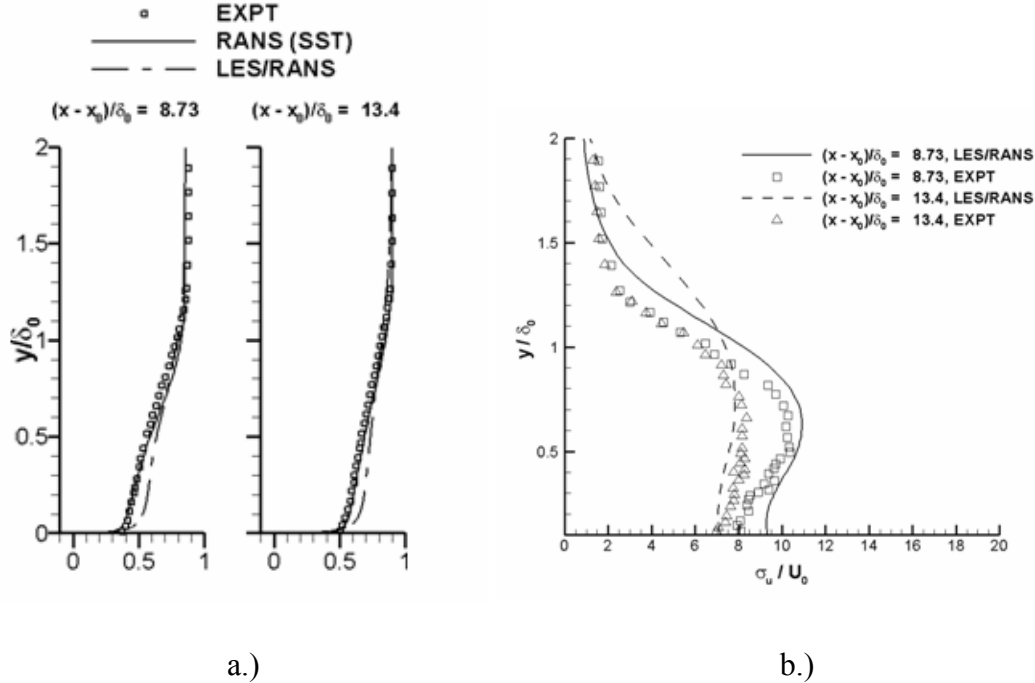


Figure 58: Streamwise turbulence intensity profiles at various streamwise locations; a) inflow, b) interaction region, and c) downstream

is still present in these calculations as it was for the no-control case. The pressures along the lower wall of the cavity agree well with the experimental data.

Centerline axial velocity profiles are shown for two downstream stations in Figure 58a. RANS predictions are in excellent agreement with the data, while the LES/RANS computations predict a fuller profile near the wall. Figure 58b shows streamwise turbulence intensity profiles at two streamwise locations downstream of the interaction. The computed turbulence intensity agrees well with experimental data at the $(X - X_0)/\delta_0 = 8.73$ station. At the station furthest downstream, the turbulence intensity is over-predicted in the outer region of the boundary layer. The peak turbulence intensity at the downstream locations increases when control is added, as can be seen by comparing Figure 58b with Figure 48. The combination of unsteady blowing and suction as induced by the mesoflap dynamic response appears to amplify turbulence to levels higher than encountered in the case without control. This effect is opposite to that provided by strong, nominally-steady bleed rates, as discussed in Section 6.3.

6.5. Hyper-X Boundary Layer Trip Arrays

A version of the IB flow solver was used by Meelan Choudhari of NASA Langley Research Center to compute laminar-flow base states induced by some of the boundary-layer trip geometries used in NASA's Hyper-X program. Trip geometries similar in shape to the micro vortex generators were first considered [P-3, P-4], followed by square-peg trips.[P-7]. Each trip was rendered as an immersed boundary. The resulting converged base states were then analyzed using linear stability theory to determine the most amplified modes. Figure 59 shows the

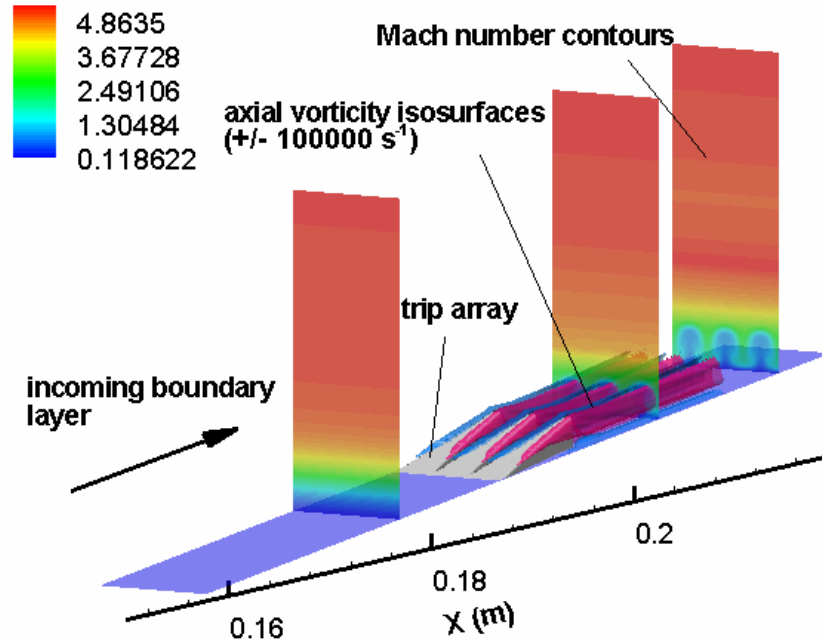


Figure 59: Vortical flows induced by Hyper-X boundary layer trips

formation of longitudinal vortical structures in the Hyper-X forebody boundary layer due to the trip arrays. The reader is referred to Refs P-3, P-4, and P-7 for further details of these calculations.

6.6. University of Michigan 3D Shock / Boundary Layer Interaction

The immersed-boundary method was also used in a recent calculation focused on 3D shock / boundary layer experiments conducted at the University of Michigan. These experiments were used in a blind challenge test to ascertain the ability of current methods (mainly RANS and LES/RANS) to predict the detailed features of such interactions. The Michigan team used stereo PIV techniques to develop a reasonably complete map of the velocity field and second-moment quantities within the interaction region. The shock generator was mounted in the middle of their wind tunnel to avoid tunnel-starting issues. A consequence of the mounting strategy was that the shock generated was not two-dimensional, but rather, conical. The entire interaction was also influenced by sidewall shock / boundary layer interactions. The NCSU team participated in the

blind challenge study and was able to complete one calculation of this flow using the newest version of the LES/RANS method [27]. The immersed-boundary technique developed in this work was used to model the effects of the shock generator. The non mass-conservative variant, which reconstructs the pressure field within the band cells, was employed, as the use of the conservative form led to band-cell oscillations in pressure which then propagated along Mach lines toward the surface. To account for unresolved boundary layer growth on the shock

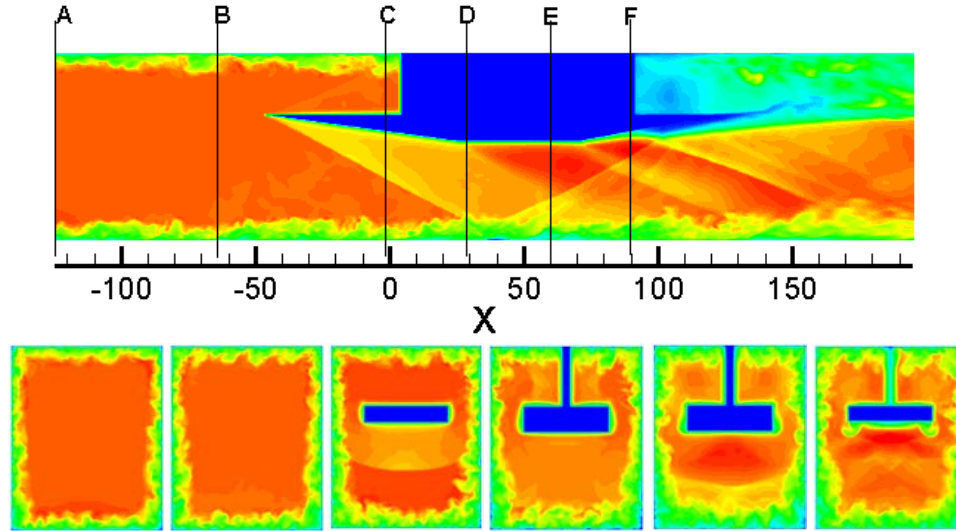


Figure 60: Instantaneous Mach number contours: University of Michigan SBLI experiment

generator, the normal vectors defined at the lower surface were transitioned between values corresponding to a wedge angle of 8.5 degrees to the correct wedge angle of 7.75 degrees over a distance equal to 1/10 of the length of the shock generator. This modification was necessary to obtain the correct shock impingement point. Figure 60 shows instantaneous Mach number contours for this calculation. The blue contours correspond to the blanked-out portions within the shock-generator immersed body.

7. Conclusions

This work has developed an extension of an existing immersed-boundary (IB) method to compressible, turbulent flows and has investigated its use in simulating the effects of different types of flow control devices: micro vortex generators, bleed-hole arrays, aero-elastically-deforming ‘mesoflaps’, and boundary layer trips. The IB method has been used with RANS (Menter SST) and LES/RANS turbulence closures. The method has been applied to oblique shock / turbulent boundary layer interactions with and without micro VG flow control (Cambridge University experiments), bleed flow control (NASA Glenn experiments), and mesoflap flow control (University of Illinois experiments). The following general conclusions may be stated (case-specific conclusions may be found in References P-1 through P-9).

1. The LES/RANS model originally developed in [15] provides good predictions of the mean flow structure of these interactions with and without control. Second-moment predictions are also in good accord with available experimental results. In general,

though, the mean-flow results are no more accurate than those provided by the Menter SST RANS model, which performs excellently for this class of relatively weak shock / boundary layer interactions. Specific deficiencies noted in the LES/RANS model include a slight tendency to under-predict the axial extent of separation and a related tendency to over-predict the recovery rate the boundary layer downstream of re-attachment. The latter effect may be overcome by a new variant of the LES/RANS model [27] which is better able to respond to changes in the equilibrium structure of a boundary layer.

2. The compressible, turbulent version of the IB model performs very well in mimicking the effects of the control devices considered without the need for excessive mesh refinement in the vicinity of the devices. Two versions have been developed: one of which is rigorously mass-conserving. The non- mass-conserving version provides smoother flow solutions near the IB. The mass-conserving version can result in oscillations in thermodynamic properties near the IB, but its use is necessary for problems in which precise mass conservation is essential. Examples of this include flow through small slots and holes.
3. The IB framework has been extended to include aero-elastic effects as modeled through beam-bending theory. Predictions of meso-flap deflection for the University of Illinois experiment and the associated effects on the fluid dynamics of the interaction appear to be qualitatively correct.
4. The Cambridge University SBLI experiments with micro VGs are significantly influenced by three-dimensional effects associated with sidewall boundary layer separation. These contribute to the enlargement of the primary zone of axial separation near the centerline of the wind tunnel. A quantitative assessment of the effects of the micro VGs is made more difficult because of these effects, but the general trend is that the vortices induced by the micro VGs deform the region of separation but do not eliminate it entirely. Computations of idealized SBLIs with micro VG control show that the strengths of the generated vortices are maintained for a reasonable distance downstream of the interaction, and the LES/RANS model in particular predicts a broadening of the vortices that energizes the entire recovering boundary layer. These trends suggest that the micro VG concept has the potential of controlling weaker shock / boundary layer interactions (generated as part of a shock train) even if the primary separation region is not wholly eliminated.
5. The disturbances induced by bleed-hole arrays of the type used in the NASA Glenn experiments are highly localized to each bleed port and are not representative of a continuous suction effect. The fact indicates that existing bleed models may have to consider variable porosity effects for better predictions. Reynolds-stress predictions obtained from the LES/RANS model indicate that the use of high levels of boundary-layer bleed suppresses the amplification of turbulence often noted in shock / boundary layer interactions. This result indicates that the dominant source of turbulence amplification in un-controlled interactions may be the dynamics of the separation / re-attachment event.
6. The UIUC mesoflap concept as applied to oblique SBLIs is not a particularly effective means of control if the intent is to remove regions of axial separation. Strong blowing into the boundary layer occurring at the first few mesoflap stations forces the boundary layer away from the surface, increasing the probability that the impinging shock will

separate the boundary layer. The suction is applied near the place where the separated boundary layer would re-attach naturally and thus has little effect. Turbulence levels in the recovering boundary layer are enhanced with meso-flap control, relative to the case without such control. This may make the boundary layer more resistant to subsequent shock impingements. An analysis of the frequency response of the mesoflap system indicates that the dominant forcing frequency is comparable to the low-frequency modes naturally observed in uncontrolled SBLIs with flow separation. This provides additional evidence that the mesoflap concept does not remove separation to any significant extent and may, in fact, increase separation.

8. Directions for Future Work

Some challenges and directions for future work are summarized as follows.

1. The IB method needs to be improved so that the best features of the non-mass-conservative and conservative variants are combined. The fact that the surface normal vectors can be altered so that they may not exactly conform to the true surface normal (as used in Section 6.6) may provide directions for future development, as the normal vector could be considered a variable that may be adjusted to enable better mass conservation.
2. The coupling between the structural solver and the IB movement algorithm needs to be improved. The fact that mass is ‘swept’ from one class of cell to another as the IB moves is not directly accounted for in the current implementation. Techniques used to maintain particulate mass conservation in the presence of IB body movement [39] were implemented but were not successful.
3. Observed weaknesses of the LES/RANS method include its tendency to under-predict the extent of axial separation, its tendency to over-predict the rate of recovery of the re-attaching boundary layer and the lack of generality of the calibration procedure. A new model [27] that is designed to overcome some of these deficiencies is under development.
4. The effects of three-dimensionality on the flow structure of shock / boundary layer interactions and the efficacy of various control devices in these situations are not understood at present. A future focus will be to apply the LES/RANS/IB models to such flows considering the full effects of wind-tunnel boundary layers, sidewall SBLIs, and corner vortical structures. The case presented in Section 6.6 is a starting point, but much more work, performed in close collaboration with experimental efforts, is needed.

9. Publications Resulting from this Study

[P-1] Ghosh, S., Choi, J-I., and Edwards, J.R. “RANS and hybrid LES/RANS Simulation of the Effects of Micro Vortex Generators using Immersed Boundary Methods” AIAA Paper 2008-3728, Presented at the 38th AIAA Fluid Dynamics Conference, Seattle, WA, June, 2008.

[P-2] Ghosh, S., Choi, J-I., and Edwards, J.R. “Simulations of Shock / Boundary Layer Interactions with Bleed using Immersed Boundary Methods,” AIAA Paper 2009-1330, Jan. 2009. Presented at the 47th Aerospace Sciences Meeting and Exhibit, Orlando, FL, Jan. 2009.

[P-3] Choudhari, M., Li, F., and Edwards, J.R. “Stability Analysis of Roughness Array Wake in High-Speed Boundary Layer” AIAA Paper 2009-170, Presented at the 47th Aerospace Sciences Meeting and Exhibit, Orlando, FL, Jan. 2009

[P-4] Choudhari, M., Li, F., Chang, C.L., and Edwards, J.R., "On the Effects of Surface Roughness on Boundary Layer Transition," Proceedings of the International Conference on Aerospace Engineering and Exhibition, 2009, Bangalore, India, May 18-22, 2009.

[P-5] Ghosh, S., Choi, J.-I., and Edwards, J.R. “Numerical Simulations of the Effects of Micro-Vortex Generators using Immersed Boundary Methods” *AIAA Journal*, Vol. 48 No. 1, 2010, pp. 92-103

[P-6] Ghosh, S., Choi, J.-I., and Edwards, J.R. “Simulation of Shock Boundary Layer Interactions with Bleed using Immersed Boundary Methods” *Journal of Propulsion and Power*, Vol. 26, No. 2, 2010 (to appear)

[P-7] Choudhari, M., Li, F., Chang, C., King, R., Edwards, J.R., and Kegerise, M., “Laminar-Turbulent Transition Behind an Isolated Roughness Element in a High-Speed Boundary Layer” AIAA Paper 2010-1575, Presented at the 48th Aerospace Sciences Meeting and Exhibit, Orlando, FL, Jan. 2010.

[P-8] Edwards, J.R. “Hybrid LES/ RANS Simulation of the Effects of Boundary Layer Control Devices Using Immersed Boundary Methods” Final Technical Report, AFOSR Grant FA9550-07-1-0191, Feb., 2010.

[P-9] Ghosh, S., Choi, J.-I., and Edwards, J.R. “Numerical Simulation of the Effects of Mesoflaps in Controlling Shock / Boundary Layer Interactions” AIAA Paper 2010-4465. To be presented at the 40th AIAA Fluid Dynamics Conference, Chicago, IL, June, 2010.

10. Personnel

Jack R. Edwards, Principal Investigator

Jung-Il Choi, Research Assistant Professor

Santanu Ghosh, Graduate Research Assistant (will defend his Ph.D Dissertation entitled “Simulations of Shock Boundary Layer Interactions Using Immersed Boundary Methods” in March, 2010)

11. Connections / Collaborations / Invited Talks

- Navier-Stokes code with immersed-boundary methodology provided to Meelan Choudhari of NASA Langley and used to predict flows over boundary-layer trip arrays
- Recycling / rescaling turbulence-generation module provided to Datta Gaitonde at AFRL/RB and implemented into AFRL’s FDL3DI solver during the PI’s visit to AFRL in July, 2009.

- Invited talk on AFOSR-sponsored work entitled “Hybrid LES/RANS/Immersed-Boundary Methods for Simulating Effects of Boundary-Layer Control Devices” presented at the 1st Shock Wave / Boundary Layer Interaction Workshop Spring Meeting, Ohio Aerospace Institute, April 15-16, 2008
- Invited talk on AFOSR-sponsored work entitled “Simulations of Shock / Boundary Layer Interactions with Bleed using Immersed Boundary Methods” presented at the 2nd Shock Wave / Boundary Layer Interaction Workshop Spring Meeting, Ohio Aerospace Institute, March 31-April 1, 2009
- Participation in blind challenge study: AFRL Shock / Boundary Layer Interaction Workshop, Jan 8, 2010

12. Bibliography

- [1] Fukuda, M.K, Hingst, W.G., and Reshotko, E., “Control of Shock Wave – Boundary Layer Interactions by Bleed in Supersonic Mixed Compression Inlets,” NASA CR-2595, August, 1975.
- [2] Syberg, J., and Konsek, J.L, “Bleed System Design Technology for Supersonic Inlets,” *Journal of Aircraft*, Vol. 10, No. 7, 1983.
- [3] Delery, J.M. “Shock Wave / Turbulent Boundary Layer Interaction and Its Control,” *Progress in Aerospace Sciences*, Vol. 22, No. 4, 1985, pp. 209-280.
- [4] Hamed, A. and Shang, J.S. “Survey of Validation Data Base for Shockwave Boundary-Layer Interactions in Supersonic Inlets,” *Journal of Propulsion*, Vol. 7, No. 4, 1991, pp. 617-625.
- [5] Hingst, W.R. and Tanji, F.T. “Experimental Investigation of Two-Dimensional Shock – Boundary Layer Interaction with Bleed,” AIAA Paper 83-0135, 1983 (also NASA TM-83057, 1983)
- [6] Gefroh, D., Loth, E., Dutton, C., Hafenrichter, E., “Aeroelastically deflecting flaps for shock/boundary-layer interaction control”, *Journal of Fluids and Structures*, Vol. 17, 2003, pp. 1001-1016
- [7] Gefroh, D. L., “Experimental Study of Mesoflaps to Control Oblique- Shock/Boundary-Layer Interaction,” M.S.Thesis, Dept. of Aeronautical and Astronautical Engineering, Univ. of Illinois, Urbana, IL, June 2000
- [8] Gefroh, D., Loth, E., Dutton, J.C., and McIlwain, S., “Control of an Oblique Shock / Boundary Layer Interaction with Aeroelastic Mesoflaps” *AIAA Journal*, Vol. 40, No. 12, 2002, pp. 2465-2466.
- [9] Anderson, B.H., Tinapple, J., Surber, L., “Optimal Control of Shock Wave Turbulent Boundary Layer Interactions using Micro-Array Actuation,” AIAA Paper 2006-3197, June. 2006.
- [10] Babinsky, H., Li, YI, Ford, C.W.P. “Microramp Control of Supersonic Oblique Shock-Wave / Boundary Layer Interactions” *AIAA Journal*, Vol. 47, No. 3., 2009, pp. 668-675
- [11] Hamed, A., Shih, S., Yeuan, J.J. “Investigation of Shock / Turbulent Boundary Layer Bleed Interactions” *Journal of Propulsion and Power*, Vol. 10, No. 1, 1994, pp. 79-87.
- [12] Hamed, A., Yeuan, J.J., and Jun, Y.D. “Flow Characteristics in Boundary Layer Bleed Slots with Plenum,” *Journal of Propulsion and Power*, Vol. 12, No. 2, 1996, pp. 231-236.
- [13] Shih, T.I.P., Rimlinger, M.J., and Chyu, W.J. “3-Dimensional Shock-Wave Boundary Layer Interactions with Bleed” *AIAA Journal*, Vol. 31, No. 5, 1993, pp. 869-876.

- [14] Rimlinger, MJ, Shih, T.I.P., and Chyu, W.J. "Shock-wave Boundary Layer Interactions with Bleed through Rows of Holes" *Journal of Propulsion and Power*, Vol. 12, No. 2, 1996, pp. 217-224.
- [15] Edwards, J.R., Choi, J-I., and Boles, J.A. "Hybrid Large-Eddy / Reynolds-Averaged Navier-Stokes Simulation of a Mach-5 Compression Corner Interaction", *AIAA Journal*, Vol. 46, No. 4, 2008, pp. 977-991.
- [16] Choi, J.-I., Edwards, J.R., and Baurle, R.A. "Compressible Boundary Layer Predictions at High Reynolds Number using LES/RANS Models" *AIAA Journal*, Vol. 47, No. 9, 2009, pp. 2179-2193.
- [17] Choi, J.-I., Oberoi, R.C., Edwards, J.R. and Rosati, J.A. "An Immersed Boundary Method for Complex Incompressible Flows", *Journal of Computational Physics*, Vol. 224, 2007, pp. 757-784.
- [18] Fadlun, E.A., Verzicco, R., Orlandi, P., and Mohd-Yusof, J. "Combined Immersed-Boundary / Finite-Difference Methods for Three-Dimensional Complex Flow Simulations," *Journal of Computational Physics*, Vol. 161, 2000, p. 35.
- [19] Mittal, R., and Iaccarino, G. "Immersed Boundary Methods", *Annual Review of Fluid Mechanics*, Vol. 37, 2005, pp. 239-261.
- [20] Gilmanov, A., Sotiropoulos, F., and Balaras, E. "A General Reconstruction Algorithm for Simulating Flows with Complex 3-D Immersed Boundaries on Cartesian Grids" *Journal of Computational Physics*, Vol. 191, 2003, pp. 660-669.
- [21] Edwards, J.R. "A Low-Diffusion Flux-Splitting Scheme for Navier-Stokes Calculations," *Computers Fluids*, Vol. 26, No. 6, 1997, pp. 635-659.
- [22] Colella, P. and Woodward, P.R. "The Piecewise Parabolic Method (PPM) for Gas-Dynamical Simulations", *Journal of Computational Physics*, Vol. 54, pp. 174-201, 1984
- [23] Menter, F.R. "Two Equation Eddy Viscosity Turbulence Models for Engineering Applications," *AIAA Journal*, Vol. 32, No. 8, 1994, pp. 1598-1605.
- [24] Lenormand, E., Sagaut, P., Ta Phuoc, L., and Comte, P., "Subgrid-Scale Models for Large-Eddy Simulations of Compressible, Wall-Bounded Flows," *AIAA Journal*, Vol. 38, 2000, pp. 1340-1350.
- [25] Walz, A. Boundary Layers of Flow and Temperature (English translation), MIT Press, 1969.
- [26] Willis, B.P., Davis, D.O., and Hingst, W.R. "Flowfield Measurements in a Normal-Hole-Bled Oblique Shock-Wave and Turbulent Boundary Layer Interaction" AIAA Paper 95-2885.
- [27] Giesekeing, D., Choi, J-I., Edwards, J.R., and Hassan, H.A. "Simulation of Shock / Boundary Layer Interactions Using Improved LES/RANS Models" AIAA Paper 2010-111.
- [28] Wilcox, D. C., Turbulence Modeling for CFD, DCW Industries, 2nd ed., 1998.
- [29] Boles, J.A., Choi, J.-I., Edwards, J.R., and Baurle, R.A. "Simulations of High-Speed Internal Flows Using LES/RANS Models" AIAA Paper 2009-1324.
- [30] Arya, S., Mount, D.M., Netanyahu, N.S., Silverman, R., and Wu, A.Y. (1998) "An Optimal Algorithm for Approximate Nearest-Neighbor Searching", *Journal of the ACM*, Vol. 45, 1998, pp. 891-923.
- [31] Cook, R.D., Malkus, D.S., Plesha M.E., Witt, R.J., "Concepts and Applications of Finite Element Analysis", Fourth Edition
- [32] Wood, B., Loth, E., Geubelle, P., "Simulation Of Aeroelastic Mesoflaps For Shock/Boundary-Layer Interaction" *Journal of Fluids and Structures*, Vol. 16, No. 8, 2002, pp. 1127-1144

- [33] Balaras, E. and Yang, J., “An embedded-boundary formulation for large-eddy simulation of turbulent flows interacting with moving boundaries”, *Journal of Computational Physics*, Vol. 215, 2006, pp. 12-40
- [34] Willis, B.P., Davis, D.O., and Hingst, W.R. “Flow Coefficient Behavior for Boundary Layer Bleed Holes and Slots” NASA Technical Memorandum 106846, 1995.
- [35] Bond, R.B. and Edwards, J.R. “Computational Analysis of an Independent Ramjet Stream in a Combined Cycle Engine” *AIAA Journal*, Vol. 42, No. 11, 2004, pp. 2276-2284.
- [36] Smits, A.J. and Muck, K-C. “Experimental Study of Three Shock Wave / Turbulent Boundary Layer Interactions” *Journal of Fluid Mechanics*, Vol. 182, 1987, pp. 291-314.
- [37] Sun, C. C., and Childs, M. E., “Modified Wall Wake Velocity Profile for Turbulent Compressible Boundary Layers,” *Journal of Aircraft*, Vol. 10, No. 6, 1973, pp. 381–383.
- [38] Dupont, P., Haddad, C., Debiève, J.F., “Space and time organization in a shock-induced separated boundary layer”, *J. Fluid Mech.* Vol. 559, 2006, pp. 255–277
- [39] Choi, J-I. and Edwards, J.R. “Large Eddy Simulation and Zonal Modeling of Human-Induced Contaminant Transport” *Indoor Air*, Vol. 18, 2008, pp. 233-249.